TÉCNICO LISBOA

PALS – Setup optimisation and application to macromolecular materials characterisation

Luísa Alexandra Teixeira Nunes Baptista

Thesis to obtain the Master of Science Degree in

Engineering Physics

Supervisors: Dr. Luís Miguel Mota Ferreira
Dr. Rodrigo Clemente Velez Mateus

Examination Committee

Chairperson: Prof. Dr. Ilídio Pereira Lopes
Supervisor: Dr. Luís Miguel Mota Ferreira
Members of the Committee: Dr. Norberto José Sobral Catarino
Prof. Dr. Vasco António Dinis Leitão Guerra

December 2021

Acknowledgments

I would like to begin by thanking my supervisors Dr. Luís Ferreira and Dr. Rodrigo Mateus and also Dr. Luís Cerqueira, not a supervisor only in title, for all the guidance, assistance and tireless support that they provided me throughout all the work that culminated in this thesis.

I would like to extend my gratitude to Dr. António Gonçalves and Research Fellow Rodrigo Coelho, from the Solid State Group at C2TN, CTN, IST, for granting us access to the annealing facilities at the Laboratory of High Temperature Synthesis and Crystal Growth at C2TN, CTN, IST for the execution of the annealing of the nickel and copper samples used in this study and for their assistance during this process. Furthermore, I would like to acknowledge Dr. Norberto Catarino, from IPFN, IST, for permitting the use of his 3D printer for the printing of some components that were incorporated into our experimental setup.

Finally, I want to thank my close friends for the shared craic and suffering, as well as for all the help, support and friendship they so readily and constantly provided me, not only during this past year in which I was doing my thesis but also during all my academic path at IST and I also want to thank my family for all their unrelenting support, for giving me the strength and love I needed, for patiently listening to me complain about life for countless hours and for always being there unconditionally. All this journey would have been truly impossible without them all.

Resumo

Um dos aspectos fundamentais da matéria prende-se com os volumes vazios presentes no interior dos materiais, tais como defeitos atómicos, lacunas ou poros, que influenciam fortemente várias das suas propriedades macroscópicas físicas, químicas e mecânicas.

Espectroscopia de tempos de vida de aniquilação do positrão (PALS) é uma poderosa e versátil técnica de espectroscopia nuclear, não destrutiva, que permite um estudo completo dos volumes vazios no interior dos materiais, relativamente à sua existência, dimensão e concentração, através da medição do tempo decorrido entre a implantação de positrões no material e a emissão de radiação resultante de aniquilações positrão-electrão.

Dado o enorme potencial desta técnica, um espectrómetro PALS foi instalado pelo grupo de Radiação, Elementos e Isótopos (GREI), para ser utilizado na análise de materiais macromoleculares por ele desenvolvidos. Antes desta análise ser possível, foi necessário realizar este projecto, que consistiu na calibração e optimização do espectrómetro e no desenvolvimento e aprendizagem de ferramentas essenciais para a aquisição e análise dos dados. Adicionalmente, o desempenho do espectrómetro foi avaliado através de medições de tempos de vida com amostras padrão de níquel, cobre, silício de grau electrónico, Teflon® e policarbonato. Os resultados obtidos são bastante semelhantes aos valores apresentados na literatura, legitimando assim a operação do sistema e o procedimento de análise de dados.

Dadas estas medições bem-sucedidas, o espectrómetro foi aplicado ao estudo de um conjunto de amostras poliméricas, fabricadas pelo grupo, como uma primeira demonstração da utilidade da técnica no desenvolvimento e estudo de materiais moleculares a serem produzidos pelo GREI.

Palavras-chave: Espectroscopia de vida do positrão, Aniquilação de positrões, Optimização de um espectrómetro, Resolução temporal, Análise de espectros de tempos de vida, Aniquilação de positrões em polímeros

Abstract

One of the fundamental structural aspects in matter is the free volumes that exist inside materials, such as atomic defects, vacancies, voids or pores, which by enabling molecular reorganisation, strongly influence various material's macroscopic physical, chemical and mechanical properties.

Positron Annihilation Lifetime Spectroscopy (PALS) is a powerful and versatile non-destructive nuclear spectroscopy technique that enables a complete study of the free volume structure inside materials, regarding the free volumes' existence, dimension and concentration, by measuring the elapsed time between the implantation of positrons into a material and the emission of the radiation resultant from the positron-electron annihilations.

Given the tremendous potential of this technique, a PALS spectrometer was assembled at the Radiation, Elements and Isotopes Group (GREI) facilities to be implemented in the study of macromolecular materials developed by the research group. Before this analysis was possible, our work, consisting of a careful calibration and optimisation of the spectrometer and the development and training in essential data acquisition and analysis tools was required. Moreover, the performance of the spectrometer was evaluated through some positron lifetime measurements with appropriate standard samples of nickel, copper, electronic-grade silicon, Teflon® and polycarbonate. The obtained results were in excellent agreement with reported literature values, thus validating the system's operation and data analysis procedure.

Following these successful applications, the spectrometer was employed to the study of a batch of polymeric samples fabricated by the group as a first demonstration of the usefulness of PALS on the development and study of macromolecular materials produced by GREI.

Keywords: Positron lifetime spectroscopy, Positron annihilation, Lifetime spectrometer optimisation, Timing resolution, Lifetime spectra analysis, Positron annihilation in polymers

Contents

List of Tables

List of Figures

List of Abbreviations

ACAR	Angular Correction of Annihilation Radiation
ADC	Analogue-to-Digital Converter
AMOC	Age-momentum Correlation
CF	Constant Fraction
CF MON	Constant Fraction Monitor
CFD	Constant Fraction Discriminator
CFDD	Constant Fraction Differential Discriminator
CM	Classical Model
CRT	Cathode Ray Tube
DBS	Doppler Broadening Spectroscopy
DOF	Degree of freedom
EG-Si	Electronic-grade silicon
ESG	Exponential Sided Gaussian
FC Unit	Fast Coincidence Unit
FWHM	Full Width at Half Maximum
GREI	Radiation, Elements and Isotopes Group
HEMA	Hydroxyethyl methacrylate
HYB	Hybrid
MCA	Multi-Channel Analyser
MCM	Modified Classical Model
MG-Si	Metallurgical-grade silicon
NIM	Nuclear Instrumentation Module
o-Ps	Ortho-positronium
p-Ps	Para-Positronium
PALS	Positron Annihilation Lifetime Spectroscopy
PAS	Positron Annihilation Spectroscopy
PC	Polycarbonate
PE	Polyethylene
PE-g-HEMA	Polyethylene-grafted-Hydroxyethyl methacrylate
PMT	Photomultiplier tube
PP	Polypropylene
Ps	Positronium

Ps-TOF	Positronium time-of-fight
PTFE	Polytetrafluoroethylene
PVA	Polyvinyl alcohol
RTE	Rectangular Tao-Edlrup
SE	Semi-empirical
TAC	Time-to-Amplitude Converter
TE	Tao-Edlrup
W/V	Weight by Volume

Chapter 1

Introduction

One of the fundamental structural aspects in matter is the free volume structure contained within it, which may include vacancies, pores, holes, voids and other such formations, which appear due to irregular packing, density fluctuations or topological constraints. The free volume structure can have a great influence in a material's physical, chemical and mechanical properties, for instance in viscosity, physical aging, glass transition temperature and permeability. Probing and characterising it, in terms of existence, size, concentration and distribution of its local constituents, is therefore extremely important. One of the techniques that is currently well-recognised as a powerful and versatile tool for the measurement of these micro to sub-nanometer structures is Positron Annihilation Lifetime Spectroscopy, or PALS.

PALS was developed in the late 1960s as part of the wider field of Positron Annihilation Spectroscopy (PAS), which encompasses a series of nuclear spectroscopy techniques, with each exploiting a particular facet of the process of annihilation of positrons with electrons in matter. In the particular case of PALS, the elapsed time between the implantation of positrons into the material under study and the emission of the gamma radiation resultant from the positron-electron annihilations is measured. This positron lifetime depends on the state of the positron at the time of annihilation. In fact, it depends on whether the positrons annihilate from a free state in the bulk of the material or form a bound-state with a molecular electron, known as a positronium atom and commonly represented by the symbol Ps, or even if either positrons or Ps atoms annihilation takes place inside the material's free volumes, in which case it also depends on their geometry and size. By assessing this lifetime it is then possible to determine the free volumes' size and corresponding concentration and distribution in the material and relate this information with some of the material's important macroscopic features. However, in spite of its enormous potential, the PALS technique has not become largely widespread as yet, mainly due to the high price of its components and the high technical qualifications required for its installation and calibration.

1.1 Historical background

The positron (e^+), the anti-particle of the electron, was first theorised by Dirac in 1930 [1, 2] as a positive electron, in an attempt to provide an explanation for the negative energy solution obtained from the relativistic wave equation for the energy of the electron. It was eventually experimentally discovered by Anderson in 1932 [3], when he observed tracks in a cloud chamber resulting from the passage of

cosmic rays which, when subjected to a magnetic field, showed a curvature identical to that expected of a particle with the same mass-to-charge ratio as an electron but in the opposite direction. His observations were later confirmed by Blackett and Occhialini [4], who provided further experimental evidence of the positron's existence.

An important process in which positrons are involved is positron annihilation. This phenomenon was likewise theoretically predicted by Dirac [1], even though the positron had not been discovered at the time, so Dirac referred instead to "protons" and acknowledged the problem of the large difference in mass between electrons and protons. The experimental proof for such a process was achieved in 1933, simultaneously by Heiting [5], Joliot [6] and Thibaud [7], with the latter showing in the following year that the positron could annihilate with an electron by emission of two γ-rays, each with an energy of 511 keV [8]. At around the same time, Klemperer [9] demonstrated that these γ-rays were emitted in coincidence and in opposite directions, despite us now knowing that a three gamma rays emission is also possible, the probability of which was first calculated by Ore and Powell in 1949 [10].

Another pivotal advancement was the discovery of the positronium. The concept of a bound state of a positron and an electron was first conceived in 1934 by Mohorovicic [11], who named it "electrum", as a means to explain some components of unknown origin in spectra emitted by stars. This term was later replaced by "positronium" in 1945 by Ruark [12], who additionally established the symbol Ps to refer to this bound state, which was experimentally observed in gases in 1951 by Deutsch [13].

One final tremendous development that paved the way for the creation of positron annihilation spectroscopy techniques was the demonstration that the positron or Ps atom annihilation characteristics change when they are trapped at free volumes present in materials. It was thus realised the potential of assessing aspects such as lifetime, energy or emission angle of the γ-rays coming from the annihilation of positrons or Ps atoms to obtain information about the electronic structure of matter. With this understanding, the field of Positron Annihilation Spectroscopy was born, which nowadays encompasses several different spectroscopy techniques that are used to describe the free volumes inside a wide range of materials. In all of them, the γ-rays resultant from positron or Ps atom annihilations are detected, however they differ on the method of detection and the photons' characteristics of interest as well as the subsequent analysis. Among these are PALS, Doppler Broadening Spectroscopy (DBS), Angular Correction of Annihilation Radiation (ACAR), Ps time-of-flight (Ps-TOF), 3γ annihilation spectroscopy and Age-momentum Correlation (AMOC), with the former three being the most commonly and proficiently applied. Despite its rich history, this is still a developing and growing field, with various PAS techniques having been successfully employed in a number of technologically important fields of research and applications, providing an insightful characterisation of the free volume structure of materials. They have also been applied together with other probing techniques to produce a complete and detailed characterisation of the internal structure of materials, in order to assess their macroscopic attributes and hence evaluate their performance and suitableness for the intended applications.

1.2 Relevant Studies

We now redirect our attention to one of these techniques, the focus of this thesis: PALS. Since its

conception, PALS has been applied to the characterisation of the internal structure and consequently to the understanding of the macroscopic behaviour of solids, liquids and gases, with the former being the most extensively studied. Earliest PALS investigations of solids were devoted to the description of defects and the electronic structure of metals and alloys and this class of materials is still extensively probed today, with [14–17] as some recent examples. The application of PALS was later extended towards the study of semi-conductors, non-metals and crystals with [18–21] as some of the most recent studies illustrating the importance of PALS in a complete analysis of the materials' free volume structure.

Nowadays, the technique finds most usage in the field of insulator, polymeric, molecular and hybrid materials, having all started in 1952 with the first PALS experiment on polymers performed by DeBenedetti and Richings [22]. The pioneering work done in the 1960s, 1970s and early 1980s by Brandt [23, 24], Tao [25] and Eldrup [26, 27] deepened our knowledge on the relation between the annihilation characteristics of positrons and Ps atoms and the free volume structure inside polymers and, as so, paved the way for a systematic application of the technique to this class of materials. The study of polymers has endured until today with several studies published each year on the subject of polymers' free volume structure characterisation with PALS, as the assessment of the dimension, concentration and length of voids, of the spacing between polymeric chains and of the existence of cross-linking effects, all possible with PALS, plays a major influence on the evaluation of the performance and applicability of these materials. In fact, in one instance [28], PALS was applied to the characterisation of the free volume structure of polyvinylpyrrolidone, a polymer, whose free volume entities make it especially appropriate to be employed in the pharmaceutical industry for the production of a variety of drugs. Additionally, PALS was used together with other techniques to determine the optimal conditions for grafting molecularly imprinted atrazine polymers, widely used herbicides, onto polyethylene/polypropylene (PE/PP) non-woven fabrics [29]. In another study [30], properties such as glass transition temperature, relaxation characteristics and thermal expansion behaviour of three photopolymers, essential for a wide range of usages such as protective coatings, dental materials and 3D lithography, were evaluated with four different methods including PALS. Similarly, several microstructural parameters of a series of polystyrenes, particularly useful in, but not restricted to, applications and areas such as drug delivery systems, light emitting materials and nano technologies, were studied with several methods, among which was PALS [31]. Finally, gas diffusion and barrier performance properties of cellulose nanocrystals, which are increasingly being considered as green alternatives for packaging applications because of their biodegradability, low cost, high crystallinity and high aspect ratio, were correlated with the free volume properties probed with PALS [32].

Constant improvements of the technique have also allowed PALS to be used and recognised as a probing technique in the investigation and characterisation of many other types of technologically important materials, with many different applications. Ceramics [33–35], nanoparticles [36, 37] and nuclear materials [38–40] are among some of the most increasingly examined. However, despite being most commonly employed in studies in material science, it is with biological systems that PALS finds its most promising emerging application, in particular for medical purposes. It has been observed that diseased tissues and cells differ from normal healthy ones in their sub-nanostructure, molecular interactions and activity. These changes influence their molecular properties which can be detected as changes in PALS parameters.

Consequently, due to its potential to be used in *in vivo* studies for the identification of diseased tissues, the incorporation of PALS as an additional diagnostic method is being carefully studied [41–45].

Alongside these developing applications of PALS, new advances in the instrumental setup required for data acquisition have also been reported. The most outstanding innovation is the introduction of digital acquisition systems and related software [46–48], in order to replace the conventional analog Nuclear Instrumentation Module (NIM) electronics used thus far for the recording of the time spectra. This method, which is being increasingly adopted in the PALS community, allows, among other things, for better time resolutions to be achieved, provides access to additional information regarding the γ-rays detected, facilitates data reproducibility and eliminates the need for the time consuming adjustment processes of the analog electronics. In addition, this approach opens possibilities for the unification of various PAS systems in one single measuring system and the correlation of the data obtained in otherwise independent experiments, enabling the extraction of new information regarding the investigated samples.

1.3 Goals of the study

As it became apparent, PALS is still experiencing improvements and a growing interest from many industries and technological areas. This is easily understood by the fact that PALS presents four great advantages that make it a very suitable and useful method for the analysis of free volumes in materials and systems: it is a non-destructive technique, allowing subsequent use and studies of the examined samples; it provides a thorough study of the material's free volume characteristics, in a wide range of temperatures; it can probe both near-surface and in-depth regions and even layered structures; and the experimental setup can operate unattended and for long periods of time, which facilitates and accelerates the process of analysis.

Given the number of applications of the PALS technique and its tremendous potential in the characterisation of the free volume structure of different solids, the research group GREI - Radiation, Elements and Isotopes Group, in which this thesis is inserted, has assembled in its facilities, in C2TN, CTN, IST, a PALS instrumental setup for the analysis of a variety of polymer-based and hybrid materials that are synthesised through irradiation methods, to be used mainly for biomedical purposes and conservation of cultural heritage artefacts. The application of PALS to the examination of these materials is of extreme relevance given that their free volume structure can influence some critical aspects that are decisive for their performance and suitableness and it was in order to meet this need that this work has emerged. The work described in this thesis broadly involves three main goals. The first is the optimisation of the GREI's PALS spectrometer, by revising and improving its fast coincidence electronic system. This process will be backed up by the acquisition of experimental PALS spectra with the apparatus for reference materials with well known behaviour, namely pure nickel, copper, electronic-grade silicon, high-purity commercial Teflon® (PTFE) and Polycarbonate (PC) and the comparison of the results obtained with literature data. Secondly, the obtainment of a deep understanding of the analysis methods and procedures that go into an experiment using the PALS technique is intended. Furthermore, a set of tools required for the analysis of the PALS spectra acquired and the transformation of the subsequent results into information regarding the free volumes of the studied samples is to be developed. The final objective concerns the

application of a then optimised spectrometer to the acquisition and further analysis of spectra of a series of macromolecular materials developed by the research group, such as radiation processed polymer-based and hybrid materials, which constitute two fundamental lines of work of the group regarding research in advanced materials, in order to analyse important morphological and structural characteristics of these materials.

Some of the materials recently developed by the research group and candidates to be analysed in the future with the PALS spectrometer optimised during this work are reported below. One of these materials were Polyvinyl alcohol (PVA) supported catalytic membranes obtained by γ-irradiation, which have been probed in order to assess their viability to be used in pervaporation membrane reactors, for the production of biodisel [49]. Another example are hybrid materials resultant from the mixture of three different precursors, prepared by γ-irradiation, whose micro and nanostructures have been a particular focus of study [50, 51]. These structures are concerned with the material's porosity and consequently have an influence in the design of these materials for biomedical applications, for instance, in bone cement or when cellular anchoring processes are required to keep the cells together and the structural cohesion of tissues. Finally, another set of materials were chitosan-based matrices that were prepared by γ-irradiation to be used as scaffolds, supports that are used as a template at a body injury to guide cell growth and regeneration, thereby assisting the body in growing new and functional tissue [52]. In order to be used as a scaffold, a materials needs to a have a suitable porosity for cell in-growth, which signifies a three-dimensional interconnected porous architecture where cells could easily attach and proliferate. This study demonstrates how γ-irradiation processing of chitosan-based matrices can be a useful method of modelling a material to have, among others, this one fundamental property required to be used in tissue regeneration.

1.4 Thesis structure

This thesis is subdivided into five additional chapters. In chapter 2, the theoretical background for the understanding of the physical processes that are on the basis of the PALS technique is laid out, by encompassing a discussion on photon and positron interactions with matter and on the models used to relate the PALS parameters and the characteristics of the free volumes inside materials. Following this, in chapter 3, after a description of how a PALS measurement is carried out, the aspects required for a PALS acquisition and ensuing treatment of the data acquired are discussed in detail. These include the source of positrons, the experimental setup, the data fitting software and the samples to be studied. In chapter 4, a recount is given of both the experimental setup optimisation and calibration work carried out and the tools developed to simplify the analysis of the data acquired. Then, in chapter 5, the results of measurements performed with a now optimised spectrometer are presented, beginning with the ones obtained for all reference samples and ending with the ones attained for the polymeric samples analysed, including the values estimated for the size of the free volumes inside them. Finally, in chapter 6, an overview of the information outlined in this thesis is presented, by also detailing future work directions to further improve the experimental setup as well as the progress which may be able to be carried out based upon the results of this study.

Chapter 2

Theory

2.1 Photon interactions with matter

Although a large number of interaction mechanisms with matter are possible for γ-rays, only three play an important role in radiation measurements: photoelectric effect, Compton scattering and pair production. Grasping the basic aspects of these processes and the way in which they are represented in a γ-ray spectrum is essential to the understanding of the process of selection of the energies to be detected performed during the calibration of the PALS setup and explained in detail in *Section 4.1.2*. The three processes are relevant over a wide range of energies, with the photoelectric being the dominant for low energy photons, with energies up to hundreds of keV and pair production the one that dominates for high energy ones, with energies higher than about 5 MeV, while the Compton scattering is the predominant for photons with energies in between. Although, the predominance of each mechanism is also dependent on the atomic composition, in particular the atomic number, of the material striked by the photons.

2.1.1 Photoelectric effect

When a low energy photon is incident on matter, it may happen that it interacts with a constituent atom, being absorbed in the process and, in return, an atomic electron, called a photoelectron, is ejected from one of the atom shells, in an interaction known as photoelectric effect. However, this phenomenon is only possible when the energy of the incident photon is greater than the energy binding a particular electron to its bound shell. When this energy criterion is met, the photon's extra energy is transferred to the photoelectron in the form of kinetic energy, meaning that the photoelectron is ejected with a kinetic energy, E, dependent on the frequency of the incident photon, ν, by means of:

$$E = h\nu - E_b \tag{2.1}$$

where h is the Plank constant and E_b is the binding energy of the electron's original shell.

2.1.2 Compton scattering

For intermediate energy photons, a scattering process between the incident photon and an atomic electron is possible, in a process designated as Compton scattering. In this situation, the incident photon

transfers a portion of its energy to the electron, which recoils as a result, while the photon is deflected by a certain angle from its original direction. The final energy of the deflected photon is dependent upon the angle of scattering and can be computed through the following expression, which is be derived by simply writing the equations for the conservation of energy and momentum, assuming a loosely bound and at rest electron:

$$E_{final} = \frac{E_{initial}}{1+\frac{E_{initial}}{m_e c^2}(1-cos\theta)} \tag{2.2}$$

where $E_{initial}$ is the initial energy of the photon, θ is the scattering angle and m_e is the rest mass of the electron. For small scattering angles, very little energy, close to 0, is transferred from the photon to the electron and even in the extreme case of a backscattering, for $\theta = \pi$, where the most energy is transferred to the electron, some of the original energy is still retained by the incident photon.

2.1.3 Pair production

In the event that the energy of an incident photon is greater than 1.022 MeV, twice the rest mass of the electron, a phenomenon by the name of pair production is energetically possible and likely to occur. In this process, required to take place in the presence of the Coulomb field of a nucleus, the photon gives rise to an electron and positron pair, each with a rest mass of 511 keV, reason why the photon mass must be larger than 1.022 MeV (2×511 keV) for the production to occur. The excess energy above 1.022 MeV carried by the photon is converted into kinetic energy to be shared by the pair. Because the produced positron will eventually annihilate in the medium, two annihilation photons are normally generated as secondary products of the pair production.

There is no simple expression for the probability of pair production to occur, although, admitting its magnitude is proportional to the square of the atomic number of the absorbent material is a rather good approximation [53]. The momentum and separation angle between the two created specimens is determined by the laws of conservation of energy and momentum and it is in order to satisfy them that the process must take place near a nucleus, as an interaction involving a single photon and an electron–positron pair produced in free space could never satisfy the conservation of both energy and momentum.

2.2 Positron interactions with matter

Upon the incidence of a positron on a solid surface, it will either backscatter or will implant into the material. In the latter case, the positron will interact with matter by undergoing thermalisation, followed by diffusion and, in materials with a lower electronic density, possibly formation of positronium atoms. Furthermore, the positron can perhaps suffer trapping at specific sites within the material and finally annihilate with an electron as either a positron or as part of a Ps atom.

2.2.1 Thermalisation

When injected into a solid, an energetic positron will undergo thermalisation within the lattice, which means that it will gradually lose energy until it reaches thermal equilibrium with the medium, by processes that are dependent on its kinetic energy and the type of the material in which it was implanted. For

the highest energetic positrons, with E_{kin} up to a few MeV, the main mechanisms for energy loss are electronic excitation of molecules and ionisation of the medium's atoms, which, as a result, creates a trail of electron and ion pairs along the trajectory of the injected positron. The positrons will lose energy until atom ionisation is no longer feasible and when they finally slow down to energies in the eV range, the phonon scattering and the excitation of electrons up to the conduction band and subsequent creation of electron-hole pairs, take over. It is at this point that a thermal equilibrium is achieved, maintained by phonon absorption and emission. Despite being a relatively short process when compared to the lifetime of a positron, taking only a few picoseconds, reason why it is commonly neglected in lifetime calculations, it is, nevertheless, during thermalisation that the most penetration of a positron into a solid takes place.

2.2.2 Diffusion

Upon reaching thermal equilibrium with the medium, the behaviour of the positrons is dominated by electrostatic interactions with the host lattice. At this point the positrons begin the process of diffusion through the material, undergoing a three dimensional random walk through the lattice, in which they interact with their surroundings, through quasi-elastic and isotropic collisions with the host atoms, before forming a Ps atom, being trapped or annihilating with the electrons of the medium. This mechanism has a small contribution for the positrons' implantation in the material but together with trapping is one of the greatest contributors for their lifetime.

2.2.3 Positronium formation

After the processes of thermalisation and diffusion, the formation of positronium atoms, mentioned in the introduction of this thesis, can take place, but only in materials with a low electronic density, for instance polymers or insulators, where a fraction of the injected positrons, typically 10% to 50%, will form Ps atoms. A positronium atom is created when a positron captures a host electron and a neutral but unstable bound state of the positron-electron pair is created, as an analogue of the hydrogen atom, but with the proton replaced by a positron, whose instability will inevitably lead to its decay through a positron-electron pair annihilation. Unlike those materials, positronium formation is not possible in metals and semi conductors as in such a high electron density environment, positrons will surely annihilate with electrons in the surroundings before they have a chance of forming a Ps atom with one of them.

Ps can be formed by two distinct processes, described by the Ore model [54] or the blob model [55–58], which is an extension of the traditional spur model [59]. The Ore model or Ore gap model describes Ps formation by a positron which has not yet completely thermalised and, given its excess kinetic energy, is capable of capturing an electron from a surrounding molecule as it passes through the medium. This process is most probable when the positron's energy is greater than $E_i - E_{Ps}$, where E_i the ionisation energy of the medium and E_{Ps} is the binding energy of the Ps, which in vacuum is 6.8 eV, but may be smaller in the medium, an energy range where no other electronic energy transfer process is likely. This model is more suited to describe Ps formation in gases while the blob model better describes this process in condensed matter. The blob model states that at the end of the slowing-down process, when the positron's kinetic energy is only a few hundred eV, it creates a track of electron-ion pairs, resultant from

the last ionisation collisions, within a blob with a radius about a few dozens of Å. A positron thermalised within the blob can not escape and a Ps atom will be formed when, through electrostatic attraction, a positron captures an intrablob electron, competing against other processes, such as annihilation, electron-ion recombination, diffusion of electrons and escape of the positron out of the blob.

Regardless of the process, once created, the positronium in the ground state can exist in two different configurations depending on the alignment of the positron and the electron spins. On one hand, it can exist as a singlet state, also called para-positronium or p-Ps, which corresponds to 1/4 of the Ps atoms formed and where the spins of the electron and positron are in opposite directions, making the spin angular momentum equal to 0. The p-Ps state, which has a mean characteristic lifetime of 125 ps in vacuum can only self-annihilate into an even number of photons and it decays primarily through the emission of two back-to-back 511 keV γ-rays, being this the only decay mode with a significative branching ratio. On the other hand, Ps atoms can exist as a triplet state, known as ortho-positronium or o-Ps, which corresponds to the remaining Ps atoms formed and where the spins of the electron and positron are in the same direction, meaning that the spin angular momentum is equal to 1. The o-Ps state, with a longer mean characteristic lifetime of 142 ns in vacuum, can only decay into an odd number of photons, in order to conserve spin and angular momentum. As in the previous instance, only one decay mode is significant, the decay into three γ-rays, in which case the energy distribution of each of these photons is reasonably approximated by a linear increase from zero energy to a maximum cutoff at 511 keV.

2.2.4 Trapping

Before suffering annihilation, which will be discussed in detail in the next section, both positrons and Ps atoms may undergo the process of trapping, a process which is slightly different for materials with a high electron density and materials with a lower one.

In materials such as metals and semi-conductors, with a high density of free electrons in the conduction band, after reaching thermal equilibrium and while diffusing within the atomic lattice of the material, the positron, having a positive charge, undergoes Coulomb repulsions with the positive ions within matter. In materials with lattice imperfections, such as defects, dislocations, voids or any other type of free volume, both atoms and electrons may either be missing or their density may be locally reduced at these flaws. Then, the combined effect of the reduction of the Coulomb repulsion by the positively-charged ion cores and of the redistribution of electrons causes a deep negative electrostatic potential trap at these defects. Therefore, positrons see these locations as strongly attractive centres in the material, where their energy is lower than if in the free positron state and thus are very likely to succumb to these localised states. The transition from a free state to this localised one is called positron trapping. Detrapping from a shallow enough trap is possible with the assistance of phonon interactions, however, detrapping from deep traps is practically impossible, leaving the positron trapped until annihilation. Moreover, at these sites, the local electron density is lower when compared with the average electron density sampled by positrons in the bulk of the material, hence it is expected that positrons reside there for longer periods of time, given that they have increased difficulty in finding an electron to annihilate themselves with. Additionally, for

a given type of material, the larger the defect size, the longer positrons can reside in it and vice-versa.

On the other side of materials' structural organisation, we have materials with a low electron density, such as polymers and insulators. In these materials, there is usually an abundance of areas of lower nuclear and electron charge density, such as pores, vacancies, cracks and free volumes of all kinds. The reduced dielectric response of the medium in such locations leads to a higher binding energy for both positrons and Ps atoms, which, as we have seen, can be formed in these types of material, and thus near these defects they are pushed into them. Once there, both specimens will move through the volume, lose energy by deflecting off the walls, interact with the surrounding molecularly bound electrons and eventually trap at the potential well of the free volume. If the material's free volumes are closed, then positrons and Ps atoms will be trapped there and will bounce around in the walls until their annihilation. As with the case of metals and semi conductors, the annihilation probability is strongly dependent on the pore size, resulting in that the lifetime of the specimens in this trapped state increases systematically with increasing size of the free volume. However, in the case of the voids in the material being interconnected, due to their light mass and high mobility, positrons and Ps atoms will diffuse within the porous network over great distances, that can even surpass the material thickness, while in some cases they may even diffuse out of the material and into the surroundings where they finally annihilate.

2.2.5 Annihilation processes

Finally, after undergoing all processes described before or just a combination of them, with thermalisation and diffusion happening mandatorily, all positrons injected into a material will eventually annihilate. However, many annihilation processes are possible, depending on whether positrons annihilate from a free or a trapped state and, in materials where that is possible, if they form positronium atoms and in turn whether those get trapped or not.

In their free state and at thermal energies, positrons have a much higher probability to annihilate with either a valence electron of an atom or a free electron. In the annihilation process, the particles collide and convert their mass entirely into electromagnetic energy, in the form of gamma photons. In the centre-of-mass frame, the photons' total energy is equal to $E = 2m_e c^2 = 1022$ keV, where m_e is the rest mass of the electron (or positron). This annihilation almost always yields two γ-rays of an equal energy of $E = m_e c^2 = 511$ keV, travelling in opposite directions, in accordance with the conservation of energy and momentum. Zero-, one- and three-γ annihilations are also possible, but rather rare, given that the zero- and one-γ annihilations are only possible in the presence of a third body such as a nearby nucleus to absorb the remaining energy and that the three-γ annihilation has a spin-averaged cross section of only 0.27% of that for the two-γ one. All positrons injected into the material which annihilate from this free state, tend to do so with approximately the same lifetime, which is characteristic of the material as it is proportional to the effective electron density sampled by the positrons.

Similarly, positrons trapped either in defects in high electron density materials or voids in low electron density ones will also annihilate according to this annihilation scheme. However, this time they will not annihilate with a free or valence electron on their path through matter during the diffusion process, but instead with an electron they may encounter on one of their many collisions with the defect's or void's

walls when trapped inside their potential.

Unlike positrons, free Ps atoms, whether they are p-Ps or o-Ps, while diffusing through the medium can suffer self-annihilation, as discussed in *Section 2.2.3*, even though o-Ps self-annihilations are extremely rare and when they do happen, unlike all other annihilation processes here discussed, they do not result in the emission of photons with an energy 511 keV. This annihilation mechanism has a very well defined associated lifetime for p-Ps and o-Ps atoms as they annihilate with their intrinsic self-annihilation lifetime, not the one for vacuum, as presented before, but instead with a characteristic one specific for the material in which they were formed.

Finally, when Ps atoms are trapped inside the potential well of voids within materials with a low electron density they will move through the void, colliding with its walls, until they find, in one of these collisions, a bound molecular electron with opposite spin to that of the positron, at which point a so-called "pick-off" annihilation occurs. This is an interaction by which the positron in the Ps atom does not annihilate with its bound electron, but instead with the found electron in a 2 γ-ray emission process, instead of a 3 γ-ray one for the case of the o-Ps atom. Despite the fact that this process is possible for both p-Ps and o-Ps atoms, it is not as relevant for the p-Ps because it tends to self-annihilate before it has a chance to find an electron of opposite spin in the walls of the free volume or indeed be trapped inside it. For the o-Ps, however, it is estimated that it can undergo 10^6 wall collisions before "pick-off" annihilation occurs. With each bounce, there is a certain probability to annihilate with a molecular electron, a probability which is strongly dependent on the void size, given that in smaller voids more Ps-wall collisions will take place, leading to a faster "pick-off" annihilation.

The possible annihilation processes and their characteristic time scales are summarised in *Figure 2.1*.

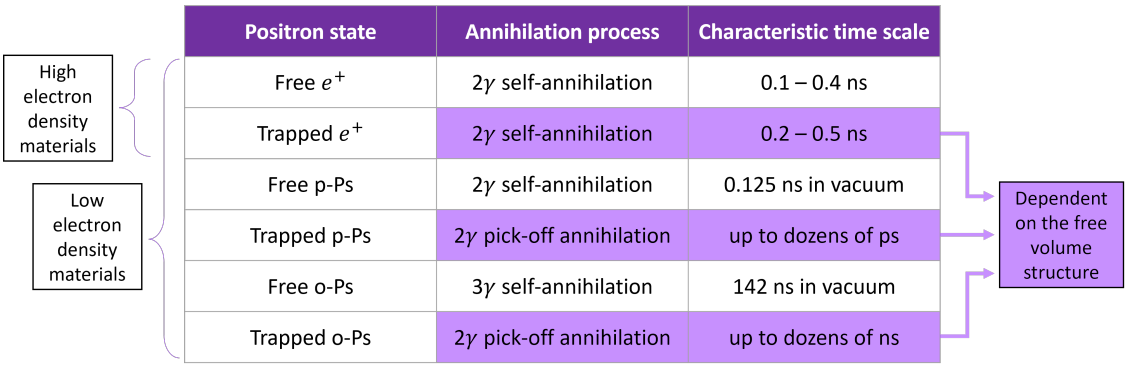

Figure 2.1: Characteristic time scales of the different positron annihilation processes in matter. Table containing data from [60].

The trapped positron two γ-ray annihilation and the p-Ps and o-Ps two γ-ray pick-off annihilation have a characteristic time scale that is dependent on the morphology and structure of the free volumes where the annihilations take place. Hence, the existence of these trapped states and their consequent lifetime determination through the PALS technique provides valuable information about the material with regards to its internal free volumes as the positron or Ps lifetime reflects their size and electronic structure, respectively, for when metals and semiconductors are under analysis or for when polymers and insulators are being studied. Furthermore, from a distribution of defect or void sizes, a positron or Ps atoms lifetime distribution will emerge. To be noted, however, that for the case of polymeric and

insulator materials, the trapped o-Ps state is the one that is more likely to take place and therefore is the one that plays the key role in providing the relevant information concerning the material's free volume structure as it is its lifetime that is used to relate the results of a PALS measurement with the size of the free volumes in a material under study.

2.3 Theoretical models for the estimation of free volumes' size

As we have seen in the previous chapter the potential and usefulness of the PALS technique stems from its capability to characterise the free volume structure inside materials, in terms of the existence, size and distribution of its constituents. However, a PALS measurement provides only the lifetime of positrons or Ps atoms that annihilate inside the analysed samples. Therefore, in order to attain the desired information regarding the free volumes in both polymers and insulators, theoretical models have been designed to correlate their size with the observed lifetime of the o-Ps atoms, all under the assumption that the o-Ps pick-off annihilation rate is independent of the material comprising the free volume's walls. A number of them have been developed over the years, in order to further tune and improve the agreement with experimental data of the ones established before. Below, is then given a detailed description of each of the models developed throughout the years, which will be used in this work to determine the characteristics of the internal structure of the studied materials developed by the research group.

The Tao-Eldrup Model

The original model for free volume size estimation with PALS parameters is the Tao-Eldrup (TE) Model, named after Tao who first proposed it [25] and Eldrup who calibrated it to improve the agreement with experimental data [27], although Nakanishi *et al.* later calibrated it even further [61]. The Tao-Eldrup Model takes into account the process of pick-off annihilation undergone by Ps atoms and estimates the probability for this phenomenon to occur, although we only apply it to o-Ps atoms. By doing so and given that this probability is strongly dependent on the size of the free volume where the o-Ps atom is trapped, the model constitutes a great method for determining the size of free volume cavities present in materials, but only for very small free volumes, with radius smaller than 1 nm.

For simplicity, the model regards the o-Ps atom as a single quantum particle with a mass twice as large as that of the electron. In addition, the model approximates the free volumes as infinitely deep spherically potential wells, that totally confine the o-Ps to the ground state. Nonetheless, totally confined o-Ps will never collide with the walls of the cavity and consequently will not decay by pick-off annihilation. In order to overcome this unrealistic situation, the free volumes are described by the quantity $R + \Delta R$, where R is the radius of the electron-free infinite potential barrier region, where the potential is zero and the o-Ps lifetime is assumed to be that of vacuum and ΔR is the depth of the potential barrier, that is the thickness of the virtual electron layer presumed to be the cavity walls where the electron density is constant and with which the o-Ps wave function overlaps, as represented in *Figure 2.2*. It is due to this superimposition of the o-Ps wave function and the walls of the cavity that the pick-off annihilation is possible. Consequently, the o-Ps pick-off annihilation rate equals the multiplication of two factors: (i) the o-Ps annihilation rate inside the electron layer in the cavity, and (ii) the superimposition probability of the o-Ps wave function with said layer.

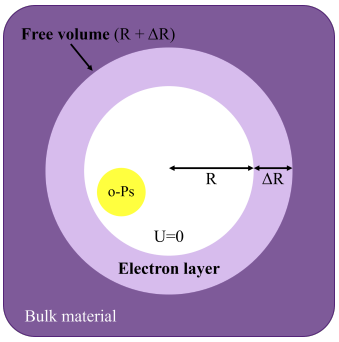

Figure 2.2: Illustration of a free volume as modelled by the Tao-Eldrup Model.

For the first factor, it is presupposed that, in the electron layer, the o-Ps atoms annihilate with the highest possible rate, which corresponds to the Ps spin-average annihilation rate in vacuum, λ_A, which is then given by:

$$\lambda_A = \frac{1}{4}\lambda_{p-Ps} + \frac{3}{4}\lambda_{o-Ps} \tag{2.3}$$

where λ_{p-Ps} and λ_{o-Ps} are, respectively, the intrinsic p-Ps and o-Ps annihilation rates in vacuum, equal to $1/0.125\ ns^{-1}$ and $1/142\ ns^{-1}$, resulting in that λ_A is approximately $2\ ns^{-1}$. For the second factor, we consider the superimposition probability of the o-Ps wave function and the electron layer inside the cavity to be:

$$P = \int_{R}^{R+\Delta R} \Psi(r) r^2 dr \tag{2.4}$$

where $\Psi(r)$ is the o-Ps normalised wave function that, by the quantum mechanics description of a particle in a spherical well, is given by:

$$\Psi(r) = \left(\frac{1}{2\pi(R+\Delta R)}\right)^{0.5} sin\left(\frac{\pi r}{R+\Delta R}\right)/r \tag{2.5}$$

By integrating the second factor, using the wave function expressed above and multiplying it by the first factor, we arrive at the pick-off annihilation rate. As we have seen, the Ps atoms can annihilate either by self-annihilation or by pick-off annihilation and the total annihilation rate is the sum of the annihilation rates of both these processes. In this scenario, the o-Ps would annihilate with its intrinsic self-annihilation rate in the central portion of the vacancy and with the here described pick-off annihilation rate in the electron layer that is assumed to be at the vacancies walls. Nevertheless, the Tao-Eldrup Model ignores the o-Ps vacuum self-annihilation rate and the overall annihilation rate of the o-Ps atom, λ_{TE}, is solely the pick-off annihilation rate due to the interactions with electrons in the walls of the free volume:

$$\lambda_{TE} = \lambda_A \left(1 - \frac{R}{R+\Delta R} + \frac{1}{2\pi} sin\left(\frac{2\pi R}{R+\Delta R}\right)\right) \tag{2.6}$$

By inverting this relation, a straightforward correlation between the lifetime, τ, of o-Ps atoms obtained from the fitting procedure, given in ns, and the radius of the free volumes is achieved:

$$\tau_{TE} = \frac{1}{\lambda_A}\left(1 - \frac{R}{R+\Delta R} + \frac{1}{2\pi} sin\left(\frac{2\pi R}{R+\Delta R}\right)\right)^{-1} \tag{2.7}$$

A reasonable value for ΔR, determined empirically by fitting the above equation to data related to liquid and molecular solids of known free volume mean radius, ranges from 0.1656 to 0.19 nm, for most materials, with the most commonly used value for polymers being 0.1656 nm.

The Tokyo Model

Despite giving quite accurate results for the radius of free volumes, the Tao-Eldrup Model is not suitable for vacancies greater than 1 nm as it neglects the 142 ns o-Ps lifetime in the central portion of the vacancy, an assumption reasonable solely for small o-Ps lifetimes and correspondingly for very small free trapping volumes. An extension of the Tao-Eldrup Model to the analysis of materials with larger free volumes, the Tokyo Model, was suggested [62], named after the University of Tokyo where it was developed. While maintaining the presumed spherical geometry of the free volumes, this new semi phenomenological model intended to estimate the size of vacancies in any range. Nevertheless, the model agrees with the experimental data only for vacancies with radius smaller than 30 nm [63].

The proposed approach was to presuppose that, inside a vacancy, the o-Ps atom has a natural annihilation rate equal to its vacuum annihilation rate, λ_{o-Ps}, plus an additional term whose value is dependent on the radius of the vacancy. For vacancies with a radius below a critical radius R_a, the additional term is simply the annihilation rate as given by the TE Model in *Equation 2.6*. On the other hand, for volumes with radius larger than R_a, the additional term is assumed to be equal to the annihilation rate given by the TE Model for a pore of radius R_a, weighted by the probability of finding the o-Ps atom inside a sphere of that radius. This results in the following total annihilation rate:

$$\lambda_{Tokyo}(R) = \begin{cases} \lambda_{TE}(R) + \lambda_{o-Ps} & R < R_a \\ \lambda_{TE}(R_a)\left(1 - \left(\frac{R-R_a}{R+\Delta R}\right)^b\right) + \lambda_T & R \geq R_a \end{cases} \tag{2.8}$$

where the probability of finding the o-Ps atom outside a sphere of radius R_a is approximated by the term $\frac{R-R_a}{R+\Delta R}$, *i.e.* the fraction of pore radius greater than R_a raised to the power of b. The values of the two free parameters were adjusted by fitting experimental data to the model and have been determined as $R_a = 0.8$ nm and $b = 0.55$ [62].

The Rectangular Tao-Eldrup Model

Another modification to the Tao-Eldrup Model in order to not only account for larger vacancies in materials but also to include a temperature dependence of the annihilation rate resulted in the Rectangular Tao-Eldrup (RTE) Model [64]. Since its conception, the model has been commonly used in the PALS community mostly due to its applicability for vacancies of any size at any temperature. However, the latest tests by Thraenert *et al.* [63] and Zaleski *et al.* [65] have demonstrated that the RTE Model agrees with the experimental data exclusively in the range between 2 and 100 nm at a temperature of 300 K.

Regardless, the model suggests that as the free volume size increases, the separation between energy levels becomes narrower, which results in that, for larger vacancies, the o-Ps atom can randomly occupy not only the ground state but also thermally excited energy levels, with different superimposition probabilities governed by the Maxwell-Boltzmann distribution. Furthermore, the vacancies are now seen as rectangular wells with sides $a + 2\delta$, $b + 2\delta$ and $c + 2\delta$, with δ a free parameter analogous to ΔR in the TE Model, which means that in fact the vacancies have sides of length a, b and c. The annihilation rate, which is calculated for a given temperature T, is then expressed as:

$$\lambda_{RTE} = \lambda_A - \frac{\lambda_{p-Ps} - \lambda_{o-Ps}}{4} F(a, \delta, T) F(b, \delta, T) F(c, \delta, T) \tag{2.9}$$

with $\delta = 0.18$ nm and $\beta = 0.188\ eV.nm^2$, both determined by existing experimental data [64] and:

$$F(x,\delta,T) = 1 - \frac{2\delta}{x+2\delta} + \frac{\sum_{i=1}^{\infty} \frac{1}{i\pi} sin\left(\frac{2i\pi\delta}{x+2\delta}\right) exp\left(-\frac{\beta i^2}{(x+2\delta)^2 k_B T}\right)}{\sum_{i=1}^{\infty} exp\left(-\frac{\beta i^2}{(x+2\delta)^2 k_B T}\right)} \tag{2.10}$$

If, for simplicity, one considers the potential well not as parallelepipedic but as cubic one, all its sides are equal with the value D and in that case, the annihilation rate, for a given temperature, is given by:

$$\lambda_{RTE}(D,T) = \lambda_A - \frac{\lambda_{p-Ps} - \lambda_{o-Ps}}{4} \left(1 - \frac{2\delta}{D} + \frac{\sum_{i=1}^{\infty} \frac{1}{i\pi} sin\left(\frac{2i\pi\delta}{D}\right) exp\left(-\frac{\beta i^2}{D^2 k_B T}\right)}{\sum_{i=1}^{\infty} exp\left(-\frac{\beta i^2}{D^2 k_B T}\right)}\right)^3 \tag{2.11}$$

The Hybrid Model

In order to overcome the difficulties of the Tokyo Model and the Rectangular Tao-Eldrup Model in terms of agreement with experimental data, a Semi-empirical (SE) Model has emerged [66] that offers a better agreement with the experimental data, at least for vacancy sizes ranging from 0.2 nm to 400 nm.

The cornerstone of this model is the assumption that, for larger vacancies, the o-Ps energy falls into the range of k_BT (*i.e.* a measure of the energy at room temperature that equals the product of the Boltzmann constant k_B and the ambient temperature T). Therefore, instead of using a spherically symmetric infinite potential well for the material's free volumes as was the case for the Tao-Eldrup Model, this model considers a spherically symmetric potential well but with a finite depth of value U_0. With this supposition, the o-Ps wave function must be described by the Gaussian wave packet that depicts the back and forth scattering of the o-Ps atom between the energy barriers on the vacancy walls before annihilating with electrons in them, thus making the o-Ps annihilation rate vary between the vacuum intrinsic and pick-off annihilation rates, in the pore central region and at the vacancy walls, respectively. According to this model, the pick-off annihilation rate thence is given by:

$$\lambda_{SE} = \lambda_A \frac{3D}{1+D} \frac{\Delta R}{R_0+\Delta R} \left(\frac{R_0}{R_0+\Delta R}\right)^2 \tag{2.12}$$

where R and ΔR are similar to the quantities introduced in the TE Model and D is the diffusion probability, that is the probability for the o-Ps to diffuse into the virtual electron layer ΔR. The value of D should be obtained via the fitting of experimental data to the model, however, its value can be estimated by $D \approx exp(-2\kappa\Delta R)$, where $\kappa = \sqrt{\frac{4m_e(U_0-E)}{\hbar^2}}$, E is the o-Ps energy in the well and m_e is the rest mass of the electron. The value of $2\kappa\Delta R$ has been found to be equal to 2, which makes $D \approx$ exp(-2) ≈ 0.135.

Given that the Semi-empirical Model accounts for the determination of the size of free volumes only for vacancies with a radius larger than 1 nm, in order to have a continuous estimation for vacancies of all sizes, a new semi-empirical model, the Hybrid (HYB) Model [67] has arisen, combining the Tao-Eldrup Model and the Semi-empirical Model. According to this approach, the combination of these two models results in the following total annihilation rate for the o-Ps atom:

$$\lambda_{HYB} = \left((\sqrt{\lambda_{TE}\lambda_{SE} + \lambda_{o-Ps}}) + (\sqrt{(\lambda_{TE} \times \lambda_{o-Ps})(\lambda_{SE} + \lambda_{o-Ps})})\right)^{\frac{1}{2}} \tag{2.13}$$

A value for D for spherical vacancies has been found to be 0.0985 from the fitting of experimental data from studies carried out over a period of four decades. Furthermore, the dependence of the annihilation rate on temperature should be treated via the diffusion probability, an aspect not considered in the present model but already being accounted for in new calculations that will be later reported [67].

The Classical Model

When the o-Ps mean free path between collisions with the cavity walls is much larger than the thermal o-Ps de Broglie wavelength ($\lambda_{dB} = h/\sqrt{(2mk_BT)} = 3.05$ nm at room temperature), which happens only for vacancies larger than several tens nm, a model based on classical mechanics, the Classical Model (CM), proposed by Gidley et al. [68] can also be considered. In this model, the o-Ps total annihilation can be calculated through:

$$\lambda_{CM} = \frac{v_{th}}{L_{o-Ps}} P_A + \lambda_{o-Ps} \tag{2.14}$$

where v_{th} is the o-Ps thermal velocity, L_{o-Ps} is the mean free path between collisions with the cavity walls, making $\frac{v_{th}}{L_{o-Ps}}$ the collision frequency and P_A is the pick-off annihilation probability per collision. The value of $v_{th}P_A$ at room temperature has been deduced to be 0.021 $\pm$ 0.002 nm/ns [69].

The Combined Model

Even though, as seen above, the Classical Model can only be applied to the estimation of the size of large vacancies, the model can be extended to smaller free volumes, by taking into consideration the finite size of the o-Ps atom, resulting in the Modified Classical Model (MCM) [70].

The average length travelled by the o-Ps atom inside a cavity between two collisions, $L_{o-Ps_{modified}}$, is equal to the mean free length of the vacancy, $\overline{L}$, *i.e.* the distance travelled by an infinitely small particle between collisions, minus $2\overline{\Delta}$, which accounts for the distance that the o-Ps is not going to travel after the previous collision and before the present one due to its finite size. This consideration results in an average length $L_{o-Ps_{modified}} = \overline{L} - 2\overline{\Delta}$. Substituting this quantity in *Equation 2.14* for the total annihilation rate in the Classical Model, we get:

$$\lambda_{MCM} = \frac{v_{th}}{\overline{L}-2\overline{\Delta}} P_A + \lambda_{o-Ps} \tag{2.15}$$

The adjustable parameter $\overline{\Delta}$ can be defined in such a way that the o-Ps annihilation rate as given by the Modified Classical Model merges smoothly with the one given by the Tokyo Model for vacancies of radius smaller than the critical radius R_a in *Equation 2.8*. Since, in the latter, the cavity is considered to be spherical and consequently its size is expressed in terms of its radius R, this quantity needs to be transformed into the mean free length of the vacancy, $\overline{L}$. This is achieved by the following relation: $\overline{L} = \frac{4V}{A}$, with V and A being the cavity's volume and surface area, respectively, which for a sphere becomes: $\overline{L} = \frac{4R}{3}$. The two models converge for $\overline{L} = 1.28$ nm, when $2\overline{\Delta} = 0.76$ nm, forming thus the Combined Model [70] applicable to free volumes of any size, where the first expression of the Tokyo Model is valid for free volume sizes smaller than 1.28 nm, or equivalently Ps lifetimes less than 21.1 ns, and the MCM Model is valid otherwise, resulting in the following expression for the annihilation rate:

$$\lambda_{Combined} = \begin{cases} \lambda_{TE}(R = 3\overline{L}/4) + \lambda_{o-Ps} & \overline{L} < 1.28 \text{ nm or } 1/\lambda_{Combined} < 21.1 \text{ ns} \\ \lambda_{MCM}(\overline{L}) & \overline{L} \geq 1.28 \text{ nm or } 1/\lambda_{Combined} \geq 21.1 \text{ ns} \end{cases} \tag{2.16}$$

Figure 2.3 displays all the models discussed above for an easier comparison of the free volumes' sizes estimated by each one. It shows the lifetime of the o-Ps, in ns, as determined by the fitting of the experimental data vs the mean free length of the free volume where the o-Ps has been trapped, in nm, as estimated by the models. Although in some models the vacancies are assumed to be spherical and the annihilation rates are presented in terms of their radius, in the following figure, all models were converted, by means of the relation $\overline{L} = \frac{4V}{A}$, to be represented in terms of the vacancies' mean free length.

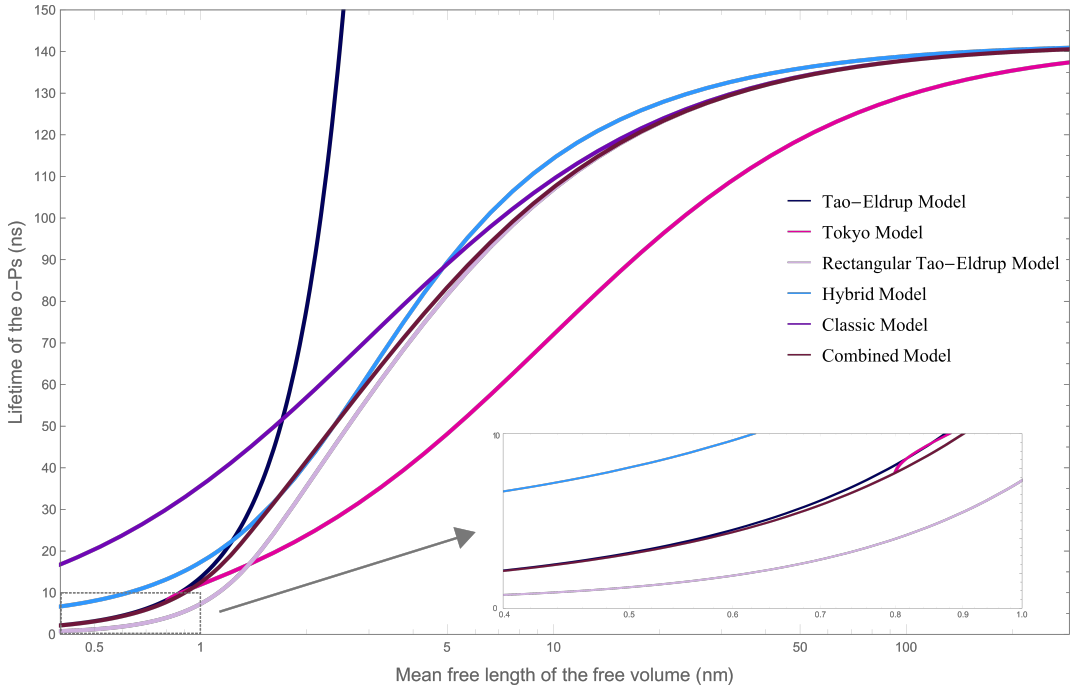

Figure 2.3: Models for free volume size estimation with parameters from the PALS analysis.

Finally, as it has become clear, each theoretical model only agrees with the experimental data in a particular range of vacancy size, hence, caution must be taken when choosing the appropriate models for determining the size of the free volumes present in a sample under study. In order to summarise this important information, the ranges of validity of each of the models discussed, both in terms of size of the free volumes and the lifetime of o-Ps atoms trapped inside them is presented in *Table 2.1*.

Model	Size range of validity	o-Ps lifetime range of validity
Tao-Eldrup Model	Radius $<$ 1 nm	$\tau_{o-Ps} <$ 28 ns
Tokyo Model	Radius $<$ 30 nm	$\tau_{o-Ps} <$ 123 ns
Rectangular Tao-Eldrup Model	2 nm $<$ Side $<$ 100 nm at a temperature of 300 K	16 ns $< \tau_{o-Ps} <$ 135 ns
Hybrid Model	0.2 nm $<$ Radius $<$ 400 nm	3.4 ns $< \tau_{o-Ps} <$ 140 ns
Classical Model	Size larger than 20 nm	$\tau_{o-Ps} >$ 123 ns
Combined Model	All sizes	$\tau_{o-Ps} <$ 142 ns

Table 2.1: Validity range of the models for free volume size estimation from PALS analysis results both in terms of size of the free volumes and the lifetime of o-Ps trapped inside them.

2.3.1 Estimation of free volumes' size distribution

In the particular case when a material presents several different but very close free volumes' sizes and in the absence of interconnected volumes, a more accurate way to describe the material's free volume structure is through the determination of its size distribution. This is achieved during the analysis process of an experimental lifetime spectrum not by fitting the spectrum to a series of discrete lifetime components but instead to a lifetime distribution, *i.e.* a continuum of lifetimes whose average value is typically in good agreement with the lifetime determined from discrete fitting. Now the goal is to transform the computed lifetime distribution into a distribution of vacancy sizes and more precisely into a relative distribution of specific vacancy volume, that is a distribution of the vacancy volume per unit sample volume. In order to do this, we start by considering an arbitrary free volume geometry, in which case the size distribution of free volumes where the o-Ps atoms annihilated is given by:

$$\frac{dN_{o-Ps}}{d\overline{L}} = \frac{dN_{o-Ps}}{d\tau}\frac{d\tau}{d\overline{L}} \tag{2.17}$$

where N_{o-Ps} is the total number of o-Ps annihilations recorded in the lifetime spectrum, τ is the o-Ps lifetime and $\overline{L}$ is the mean free path of the o-Ps inside the free volumes. This distribution must be corrected for any free volume size dependence of the o-Ps trapping probability. Thus:

$$\frac{dN_{o-Ps}}{d\overline{L}} = \frac{dN_{vacancy}}{d\overline{L}}P_T \tag{2.18}$$

where $\frac{dN_{vacancy}}{d\overline{L}}$ is the vacancy number density distribution as a function of $\overline{L}$ and P_T is the $\overline{L}$-dependent trapping probability. Now, for the specific vacancy volume distribution for any given free volume geometry, we have:

$$\frac{dV}{d\overline{L}} = \frac{dN_{vacancy}}{dl}V_{vacancy} = \frac{dN_{o-Ps}}{d\overline{L}}\frac{V_{vacancy}}{P_T} \tag{2.19}$$

Given that the o-Ps atoms are formed in the bulk of the material and subsequently diffuse into its free volumes, it is assumed that the o-Ps trapping process favors vacancies with larger surface area, which means that $P_T \propto A_{vacancy}$ and hence $V_{vacancy}/P_T \propto \overline{L}$. Thus, by knowing the fitted o-Ps lifetime distribution, $dN_{o-Ps}/d\tau$, characterised by its mean value and standard deviation and the first derivative of the equation used for the determination of the free volume size, $\mathrm{d}\tau/d\overline{L}$, it is then possible to determine the intended specific vacancy volume distribution, through the following relation, given for a particular void geometry:

$$\frac{dV}{d\overline{L}} \propto \frac{dN_{o-Ps}}{d\tau}\frac{d\tau}{d\overline{L}}\overline{L} \tag{2.20}$$

One interesting aspect about this relation is that, for the large vacancies, the distribution becomes independent of the vacancy shape and the theoretical model selected for the determination of the free volumes size. In fact, shape dependence is only introduced through $\tau(\overline{L})$, given the approximation that P_T depends on the free volume surface area but not explicitly on its geometry.

Chapter 3

PALS technique

3.1 Fundamentals

PALS is performed in the time domain since the time of each event, *i.e.* the lifetime of each individual positron is measured as the time interval between their implantation into the material being tested and the emission of a γ-ray resultant from their annihilation through one of the many possible processes described in *Section 2.2.5*. After a reasonable amount of these events, between 10^5 and 10^6, has been detected, a lifetime spectrum is obtained, representing the number of annihilation events of the implanted positrons versus their lifetime. This spectrum contains several lifetime components associated with different annihilation processes and some even depending on the existence and size of free volumes inside the material. This is due to the fact that each annihilation process has its own characteristic time signature and the fact that positrons or Ps atoms trapped inside free volumes will reside there for different time periods, depending on their size. It is with the decomposition of the acquired spectrum into these individual lifetime components and corresponding relative intensities that is then possible to extract information regarding the size, concentration and nature of free volumes in the probed material, that can have a radius as little as 1.3 Å [71].

Hence, in order to conduct an analysis of the free volume structure of solids based on the PALS technique three aspects are essential: (i) a source of positrons, (ii) an experimental setup, where the time of each event is detected and recorded, (iii) and an analysis method and software that enable the decomposition of the acquired spectrum into the individual time components and the correlation of these results with the intended information regarding the free volume structure of the material under study.

3.2 Positron source

There are two methods of implanting positrons onto a sample under analysis. One of these and by far the most popular choice consists of using a positron emitting radioactive source that suffers β^+ decay and emits positrons with a continuous spectrum of energies that ranges from zero to an end-point energy of about 0.1-1 MeV. The other implantation mechanism is done by using a linear accelerator that produces

positron beams of variable and very well defined energy, by either inducing pair production or by guiding the positrons emitted by a positron emitting source into the beam-line. The choice of which method to employ on a particular analysis relies on the type of study that is desired. For example, the use of a positron emitting source is unsuitable for probing near surface regions or a particular depth of interest within a studied sample, given the high energies and broad energy range of the incident positrons. Linear accelerators, on the other hand, are more indicated for these types of analysis, by delivering a focused mono-energetic positron beam of variable implantation energy onto the sample.

Regardless, the use of positron emitting radioactive sources is a more straightforward technique, enabling still plenty of analysis within a PALS experiment. Indeed, this was the method applied in this work for the implantation of positrons onto the sampled materials, with the ^{22}Na radioactive isotope chosen for the positron source. This particular radioisotope is the most frequently employed in PALS analysis and was selected due its many advantages, namely: the source is of simple production, handling and substitution; the isotope has a long half-life of 2.6 years suitable for the intended studies, given that it is ensured that not only does the source's activity remains nearly constant for the duration of a data acquisition run but also that the same source can be used for multiple runs; and the isotope's positron emission is accompanied by a almost simultaneous emission of a detectable gamma photon, which can be verified in its decay scheme that is represented in *Figure 3.1*.

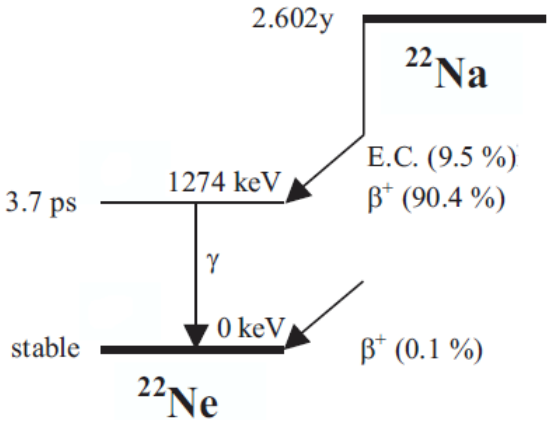

Figure 3.1: Decay scheme of ^{22}Na. Adapted from [60].

As shown, the radioisotope decays to either the 1274 keV excited state of ^{22}Ne or its ground state, which occurs through β^+ decay and has only a 0.1% branching ratio, making the relevant decay the one to the excited state of ^{22}Ne. This, in turn, can happen either by electron capture, with a branching ratio of 9.5% or by β^+ decay, with a branching ratio of 90.4%, where positrons are emitted with a continuous energy spectrum with an end-point energy of 545 keV. This high positron yield of 90.4% is another essential attribute of this radioisotope that makes it particularly fitting for the production of positrons for a PALS experiment. Furthermore, the half-life of the excited state of ^{22}Ne is only about 3.7 picoseconds, succeeded by the prompt emission of a 1274 keV γ-ray as the isotope transitions to its ground state. Given the extremely short lifetime of this excited state, both positron and 1274 keV γ-ray emissions can be considered simultaneous and the detection of this gamma photon can be used to mark

the time of emission of the positron.

The ^{22}Na source used in this work, which is represented in *Figure 3.2*, was prepared from the evaporation of around 0.33 μL of an aqueous solution of $^{22}NaCl$, with an activity of 100 μCi/μL, onto a 7μm thick Kapton® HN foil. After evaporation was complete and only the $^{22}NaCl$ crystals remained, another Kapton® HN foil of equal thickness was put on top of the crystals and the two foils were glued with an epoxy resin in order to seal the 20 mm diameter ^{22}Na positron source. Kapton® HN foils are commonly used for this purpose because, being a polymer, Kapton® HN has a very low atomic number and density. In consequence, thicker foils can be utilised, making the overall source easier to handle and considerably more durable. Therefore, when produced, in May 2016, the source's activity was roughly 33 μCi, which means that by the time the final measurements of this work were carried out, in May 2021, the activity had dropped to about 8.6 μCi. The activity of the source should be high enough to guarantee that the PALS measurements take up a sensible amount of time as well as that the positron annihilations in the lifetime spectrum are easily identifiable above background. Also it must not be so high that multiple positrons could be in the sample at the same time, leading to an overlap of annihilations in the sample and consequently the detection of false signals. For a 8.6 μCi source, the average time between decays is 3.1 μs, a value three orders of magnitude higher than the typical lifetime of positrons in matter, meaning that our source has a more than acceptable activity.

Figure 3.2: ^{22}Na source used in this work.

3.3 Experimental setup

The experimental setup used in this work comprises: a detection system, consisting of two scintillation detectors and respective photomultiplier tubes, for the detection of the implantation of a positron into the material and its ensuing annihilation; and a subsequent set of analog electronic modules, where the signals provided by the scintillators are processed in order to determine and register the value of the positron lifetime. The complete spectrometer configuration used in this work is schematically represented in *Figure 3.3*.

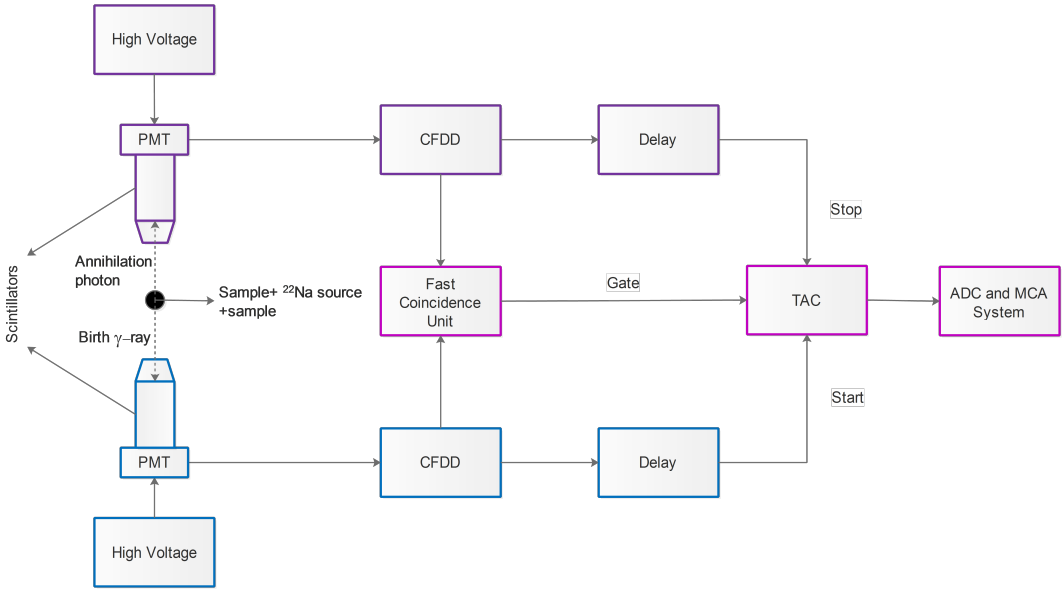

Figure 3.3: Block diagram of the PALS experimental setup used in this work.

3.3.1 Detection system

The detection system is thus intended to register the arrival times of two signals, one marking the implantation of the positron into the material and the other its annihilation. These signals are known, respectively, as start and stop signals and the time difference between the two establishes the positron lifetime. Given the almost simultaneous emission of the positron from the radioactive source and the 1274 keV γ-ray from the de-excitation of the ^{22}Ne radionuclide, the detection of this γ-ray is taken as the start signal. The stop signal, on the other hand, is considered as the detection of a 511 keV γ-ray resultant from a 2 γ-ray annihilation of the positrons ejected by our source into the material, meaning that a PALS measurement is thus based on the detection of γ-rays. An example of an energy spectrum resultant from the detection of γ-rays, otherwise known as a gamma spectrum, in this case, an energy spectrum obtained from the decay of our ^{22}Na source, is represented in *Figure 3.4*.

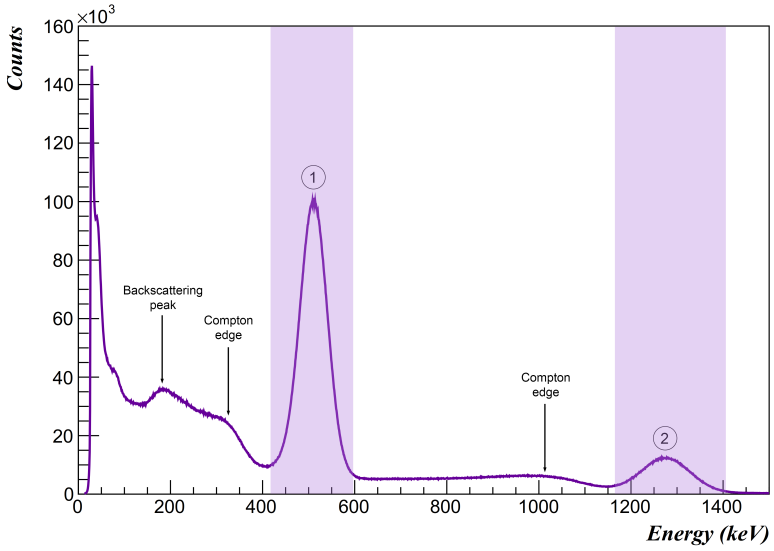

Figure 3.4: Acquired ^{22}Na radioactive source's energy spectrum.

To facilitate its interpretation and the identification of its features, a detailed explanation of the origin of each of the multiple features found in a typical gamma spectrum is provided in *Appendix A*, as understanding the composition of a gamma spectrum is of fundamental importance to later comprehend the energy selection process necessary for the calibration of the PALS setup, which is explained in detail in *Section 4.1.2*.

For the detection of these γ-rays to be possible, a sandwich composed of the ^{22}Na radioactive source and two pieces of the sample under analysis placed in close contact on either side of it, is positioned at an equal distance between the two scintillators, which in turn are facing each other, as schematically represented in *Figure 3.5*. Given that the positrons leave the radioactive source in all directions, with possible annihilations in any material they cross, it is extremely important to assure that the sample pieces are bigger than the ^{22}Na source in order to completely encapsulate it and thus minimise any unwanted contributions to the lifetime spectrum from positron annihilations in adjacent materials or in the air gap between the source and the sample pieces. Moreover, the sample pieces must also be thick enough to guarantee that the positrons emitted by the source completely stop and annihilate within the material, while at the same time, not so thick as to prevent the 511 keV γ-rays created as a result of the annihilations from being completely attenuated before they reach the detector. Hence, a thickness nigh on 2 times the range of the 545 keV (end-point energy of the continuous energy spectrum of the positrons emitted by the ^{22}Na source) positrons in the material fulfils both requirements.

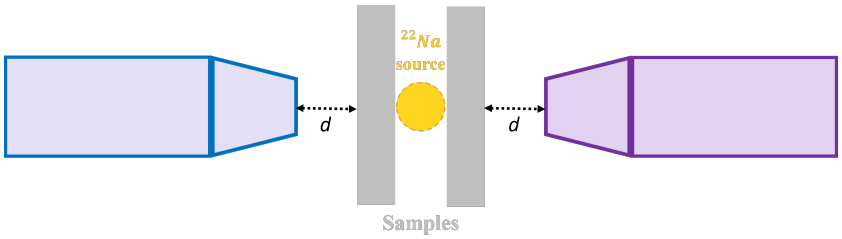

Figure 3.5: Representation of the source+sample sandwich, positioned at the centre of the two detectors.

Scintillation detectors

In a typical PALS experimental setup, the detection of the 1274 keV and 511 keV γ-rays is achieved by using two scintillation detectors, one for each γ-ray, coupled with their own photomultiplier tube (PMT).

A scintillator is a material that when bombarded by charged particles or radiation, absorbs the kinetic energy of the incoming particles or radiation, re-emitting it in the form of visible light pulses. This re-emission is a result of either fluorescence, which is the prompt emission of the visible radiation; phosphorescence, the emission of greater wavelength light than for fluorescence but after a much longer time following excitation; or delayed fluorescence, which corresponds to a delayed emission but of the same wavelength spectrum as prompt fluorescence. Disregarding cost and availability, an ideal scintillation material is desired to: exhibit a high scintillation efficiency for converting the detected kinetic energy into light; display a linear conversion, *i.e.* a light yield proportional to the deposited energy, over a wide range of energies; be transparent to its own emission wavelength (the wavelength of most intense emission), for good light collection; and convert most of the incident energy as fluorescence, while keeping

at a minimum the contributions from phosphorescence and delayed fluorescence, in order to generate fast signal pulses for a good time definition of events and a short dead time, essential for high counting rates.

Since there is no material that simultaneously meets all these essential criteria, there are several types of scintillator materials available that somewhat fulfil, to different degrees, the mentioned requirements. For this reason, even though scintillation detectors are used in every PALS experiment it does not necessarily mean that every setup comprises the same scintillator, as each experiment may require a different compromise among the many desired performance factors. Despite the great number of different scintillators they can be divided into two major categories, namely organic and inorganic scintillators. Organic scintillators encompass pure organic crystals, liquid solutions and plastics and are characterised by their hydrocarbon composition and consequent low-Z value, granting them a faster response time but a lower light yield. On the other hand, inorganic scintillators, than include inorganic crystalline materials, noble gases and glasses, tend to possess both a linear response and a great light output, however, with a few exceptions, they have a relatively slow response time. With the notable exception of plastic scintillators, organic scintillators are used extensively in beta spectroscopy and fast neutron detection, while gas and glass scintillators are commonly employed as heavy ions and neutrons detectors. On the other hand, plastic scintillators, with their notoriously fast response time and inorganic crystals, with their high Z-value and density that favours the interaction of incident photons with the scintillation medium by means of the photoelectric effect are preferred for gamma-ray spectroscopy and applications involving precise timing measurements.

In our work, the detectors chosen were barium fluoride (BaF_2) crystalline scintillators, that represent a rather satisfactory compromise between efficiency and time response, manufactured by Scionix [72] and presenting two main emission bands. The fast scintillation component, associated with the phenomenon of fluorescence, corresponds to around 15% of the total light output and is emitted in the wavelength bands centred around 195 and 220 nm, with a decay time (the time required for the intensity of the light pulse to drop below 1/e of its maximum value) falling in the range between 600 and 800 ps. The remaining 85% of the light yield consists of a relatively slow light component emitted by the crystal with a wavelength of 310 nm and with a decay time of roughly 630 ns.

The detection principle of inorganic crystals is based on the process of excitation of energy states within the material's crystalline lattice structure by an incident particle or radiation. From solid state physics, it is known that when a charged particle or radiation passes through the detection medium, a large number of electron-hole pairs are created as a result of the excitation and subsequent transition of electrons from the valence band up to the conduction band, leaving behind holes in the former. After some time, the electrons lose some energy and return to the valence band, followed by the emission of photons that carry the surplus energy from the de-excitation. In pure crystals, besides being extremely inefficient, this process will most likely result in the emission of overly energetic photons, whose energy lies beyond the visible spectrum. In order to overcome this, crystals are frequently doped with small amounts of carefully selected impurities, typically referred to as activators, to allow for additional sites to be created in the lattice containing different band structures with energy states in an intermediate energy band, known as the forbidden band, located between the valence and conduction bands. These

additional states present themselves as midway levels from where the electrons can de-excite back to the valence band, allowing therefore the emission of lower energy photons, now in the visible spectrum, thus making the detection of radiation possible in the crystal. In this scenario, when incoming particles or radiation create electron-hole pairs in the detector's medium, there are three possible mechanisms that are at the origin of the multiple light components usually exhibited by crystals:

- The electron and hole from the pair are created free and therefore separately drift through the crystal. Eventually, the electron encounters and incorporates into one ionised activator atom, that was previously ionised by one of the free holes, creating a neutral configuration. If this configuration is formed in an excited state with an allowed transition to the ground state, its de-excitation occurs very quickly and a photon is emitted in order to liberate the excess energy between the energy levels of the system. This mechanism thus gives rise to one of the crystal's fast light component, as an example of the fluorescence process.
- The electron-hole pair is created as a loosely bound state, known as an exciton, that freely wanders as one through the crystal structure until reaching the site of an impurity atom. In a similar manner as before, an excited configuration can be created and again the existence of an allowed de-excitation to the ground state induces a fast scintillation component, this time perhaps with a different wavelength, as yet another instance of fluorescence.
- The free electron from an unbound electron-hole pair discovers an excited atom from the incorporated impurity, however, upon creation of an excited configuration at the activator site, the transition to the ground state is forbidden. In this case, an additional increment of energy, which can be delivered through thermal excitations, is required to take the system to a higher energy state from which a de-excitation to the ground state is now possible. Consequently, a light emission characterised by a larger wavelength and also a much longer emission time takes place, which constitutes, therefore, the process of phosphorescence.

Photomultiplier tubes

Owing to the fact that scintillators produce extremely weak light pulses when bombarded with incoming charged particles or radiation, they must be coupled to a photomultiplier tube whose function is to convert these scintillations into usable analog, electronic pulses, which can then be transmitted to and processed by the associated electronic modules in order to register the positrons lifetime. Although other devices are equally available to perform the same task, PMTs are still the most commonly chosen for this purpose given their fast timing response, high current amplification or gain, good time resolution and broad range of radiant energies to which they are sensitive to.

A PMT is divided into two main components, namely the photocathode and the electron multiplier structure. The photons generated in the crystal then penetrate into the photomultipler tube through the photocathode input window, which serves not only to separate the PMT's internal components, which are under vacuum, from the exterior environment but, by only being sensitive to a restrictive wavelength range, also acts as a filter of the incident radiation to the PMT's interior. Provided the

photons' wavelength lies on the specified range, they then hit upon the photocathode where, by means of the photoelectric effect, an incident photon is absorbed and, as a consequence, a single low energy electron is ejected. Given that only a few photons are produced in the crystal and hence entering the PMT and also that not all photons striking the photocathode result in the emission of a photoelectron, the number of photoelectrons at the end of the photocathode is insufficient to create a convenient electrical signal. That is the reason why there is a second division of the photomultiplier designed for the multiplication of these electrons, that is comprised of various stages of dynodes, between which the electrons are accelerated by an applied potential. In each stage, when an electron hits the dynode, many other electrons are created by secondary electron emission. This process is repeated throughout the dynode chain, resulting in a cascade of 10^7 to 10^{10} electrons, enough to act as the charge signal of the original scintillation event, which are finally collected at the base of the PMT, generating an output signal at the anode whose amplitude is proportional to the energy deposited in the scintillator by the original gamma-ray.

For this work, the photomultiplier tubes selected are Hamamatsu R2059 [73], connected to two NHQ 103M high voltage modules, manufactured by FAST ComTec GmbH [74], for the supply of the required high voltage. The PMTs' spectral acceptance ranges from 160 to 650 nm, which permits the detection of the photons originating from the fast light component of the BaF_2 crystal of the scintillation detector, whose wavelengths are centred at 195 and 220 nm. Furthermore, these particular PMTs offer the possibly to obtain an output signal not only from the anode but also from the first dynode stage and exhibit an excellent time resolution as they possess a rise time of solely 1.3 ns and a transit time spread of 0.55 ns.

The detection ensemble of the two scintillation detectors and respective coupled photomultiplier tubes employed throughout this work is represented in *Figure 3.6*. As can be seen, the detectors, shown with a sample under analysis placed between them, were mounted on a rail system that allows them to move closer together or further apart up to the distance required for a specific analysis.

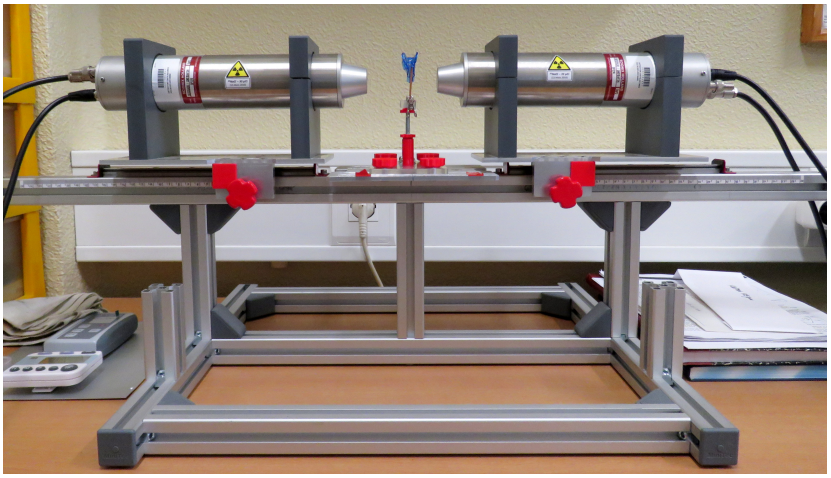

Figure 3.6: Detection system utilised in this work.

3.3.2 Electronic modules

Following the processing of the light pulses coming from the scintillation crystal, the output pulses from each PMT are sent to two dedicated Constant Fraction Differential Discriminators (CFDD), which are

used to mark the pulses' exact arrival time, through the simultaneous generation of both a fast negative signal, containing the relevant timing information and a slow positive logic output. Additionally, the CFDDs have upper and lower voltage level discriminators, ensuring that the outputs are only generated if the input pulses from the photomultiplier tube fall within the preset accepted amplitude range, *i.e.* if they simultaneously exceed the lower-level threshold and do not exceed the upper-level one. In that sense, one of the CFDDs is used to generate the start signal, thereafter referred to as the start CFDD, by being set to accept only the 1274 keV γ-rays and the other, from here on referred to as the stop CFDD, is prepared to be receptive only to 511 keV photons and therefore output the stop signal. Constant Fraction Discriminators (CFD) can also be used for the same purpose with the only difference being that instead of defining a voltage window that the signals' voltage must be within, they simply set a voltage limit above which the signals' voltage must be in order to be accepted.

The fast timing signals generated by the CFDDs are fed to the start and stop inputs of a Time-to-Amplitude Converter (TAC), but only after being passed through a dedicated delay unit. Subsequently, the TAC produces an analog pulse, whose amplitude is proportional to the time difference between the arrival of the two signals. However, in such a configuration, the TAC might be flooded with a large number of signals at its start input with no corresponding stop signals, causing a considerable dead time in the TAC. In order to prevent this, the slow positive output signals coming from the CFDDs are led to a Fast Coincidence Unit (FC Unit), likewise connected to the TAC. This unit serves the purpose of producing a gate signal in case it detects a coincidence event of photons of proper energies within the selected time frame, in other words, if a start and stop signal reach the unit within a specified time interval of each other. Only in the presence of this gate signal at the gate input of the TAC does the latter generate its output pulse, reason why a time delay is imposed to both the start and stop signals generated by the CFDDs, so as to compensate for the time required by the FC unit to process incoming signals and transmit a gate one.

Finally, the TAC pulses are digitised by an Analogue-to-Digital Converter (ADC) and conducted to a Multi-Channel Analyser (MCA), where each event is stored in a histogram as one count in the channel that corresponds to that particular signal amplitude. During a run of data acquisition, multiple events are then recorded in this histogram that constitutes the positron annihilation lifetime spectrum and represents the number of annihilation events of the implanted positrons versus their lifetime, in other words, the number of positrons that lived for a particular time period.

Constant Fraction Differential Discriminator

The CFFDs applied in this work are a Model 583B, manufactured by Ametek Ortec [75]. They can operate as both Constant Fraction Differential Discriminators or as Constant Fraction Discriminators, although the former configuration was used throughout the work as it allowed for a more fine energy selection of the input signals and consequently a greater time resolution of the system.

As it became clear, the CFDDs serve two main purposes on the signal processing chain: voltage/energy discrimination of the signals arriving from the photomultiplier tubes; and high precision record of the exact arrival time, for those which make the cut. Although the energy selection process is fairly straightforward,

the latter process, based on the constant fraction (CF) technique, entails a few more interesting aspects. In reality, when the arrival time of input signals is being recorded in the CFDDs, walk errors may arise. Walk errors are related to a high degree of timing uncertainty that derives from the fact that input pulses of variable amplitude do not necessarily, at least considering a wide amplitude range, cross the triggering threshold for timing register at the same identical time, which is precisely what is meant to be prevented with the constant fraction technique. Upon arriving to the CFDD, an input signal is manipulated in order to create a bipolar signal by: firstly, duplicating the input signal; then, delaying one of the duplicated signals, by forcing its passage through an external delay cable; and finally subtracting a fraction of the undelayed pulse from the delayed one. It is the zero crossing of this final bipolar pulse that is then detected and viewed as the arrival time of the input pulse and therefore used to trigger the generation of the CFDD output logic pulse. Hence, given that all pulses are timed for the same phase point, meaning they cross the zero level at the same fraction of their original pulse height, the timing register becomes independent of pulse amplitude and thus input signals of different amplitudes are recorded at the same exact time, greatly reducing the timing uncertainty. The influence of the CFDD's CF method on the timing uncertainty of the system as well as its dependency on certain details and components associated with the application of the method will be further explored in *Section 4.1.2*.

Delay unit

Despite being fixed throughout a run of data acquisition, in an experimental setup, it may or may not be desired that the time delays imposed on the output signals coming from the CFDDs are variable. In case this is desirable, then the delay is achieved by passing the signals through a delay module, composed of a number of cables of different lengths, in order to provide the choice of halting the signals for different amounts of time. This module usually comprises RG58 cables, characterised by a propagation velocity of about 0.66 the speed of light, resulting in a time delay of approximately 5 ns/m. On the other hand, for some lifetime spectrometer configurations or experiments, such our own, it may be preferable that the CFDDs' output signals are delayed for a fixed time period, in which case two RG58 cables of a certain and possibly different length, determined according to the time delay intended, are used to couple each of the CFDDs outputs to the TAC entrances.

Fast Coincidence Unit

The Fast Coincidence Unit employed in this work is a Model 2144A, manufactured by Canberra Industries [76] and its operation is based on the simple execution of either the logical AND function or the logical OR function to the two signals applied to its inputs, depending on whether one desires to consider coincidences or anti-coincidences, respectively. For implementation in a PALS experimental setup, only the application of the AND function is required. In that case, when two signals arrive at the unit within a specified time interval, they are perceived as coincident and an output pulse is generated, which may either represent the duration of the signals' time overlap or merely signal the existence of the coincidence.

Time-to-Amplitude Converter

In order to accurately register, to picosecond precision, the time interval between the arrival of the start and stop signals from the CFDD, time-to-amplitude converters rely on the linear charging of a capacitor. In fact, upon the arrival of the start signal, a transistor switch is opened and the constant rate charging process commences. This process is only ended when a stop signal is received at the TAC's input, within a selected time range, at which point another switch is opened, interrupting the connection between the constant-current source and the capacitor. If the stop signal fails to arrive within the selected time range, that particular time conversion event is ignored. In a capacitor, a relation between voltage, V, and constant charging current I, is established in the form of: $V = \frac{It}{C}$, where C is the capacitance and t is the charging time period, which in this case is the time interval between the arrival of the start and stop signals. The generated voltage is momentarily stored in a buffer amplifier until a linear gate is opened either automatically after a short period of time or by an external strobe upon which a positive unipolar voltage pulse, with an amplitude proportional to the capacitor's charge and consequently to the time interval between the arrival of the start and stop signals is outputted. After the transmission of this output pulse, all switches return to the closed position and the capacitor is completely discharged, in preparation for the next pair of signals. In this work, the choice for the TAC module fell on the Ametek Ortec's 567 Model. This particular model is capable of operating in either coincidence or anti-coincidence mode, meaning that the external strobe that causes the prompt emission of the TAC output can be provided either by the gate signal generated in the FC unit, the method used in our work for the start input, or by the lack thereof, the method chosen for the stop input.

Analog-to-Digital Converter and Multi-Channel Analyser

The Analog-to-Digital Converter and Multi-Channel Analyser make up part of the Multi-Channel Analyser Data Acquisition System, which, in our case, comprises the Ametek Ortec's EASY-MCA 8k Channel Multichannel Analyzer, that includes the ADC and the MCA, and the 7.0 version of MAESTRO Multichannel Analyzer Emulation Software, also produced by Ametek Ortec. Although many variations exist, the ADC provided is a 13-bit successive-approximation type ADC. These ADCs rely on a binary search to progressively narrow the range of binary "words" that possibly represent the input voltage until finally converging upon a digital output corresponding to the input pulse height. The MCA contained in the data acquisition package is a 8k channel one, meaning that the number of bins in the lifetime spectrum stored in it can be changed from 256 up to 8192. This module, together with the ADC, constitute the hardware portion of the acquisition system, which can be connected to a computer, where the MAESTRO software can be installed. The purpose of this software is to confer an overall control of the data acquisition process as it not only controls some of the hardware functions and properties, such as the ADC conversion gain or the channel range of the MCA but also provides a live display of the lifetime spectrum acquired, together with some powerful live analysis tools.

To get a better understanding of how a PALS spectrometer, up until now only schematically represented, is assembled and how the connections between its components are put into place, our PALS

experimental setup, incorporating both the detection and the electronic systems, is shown in *Figure 3.7*.

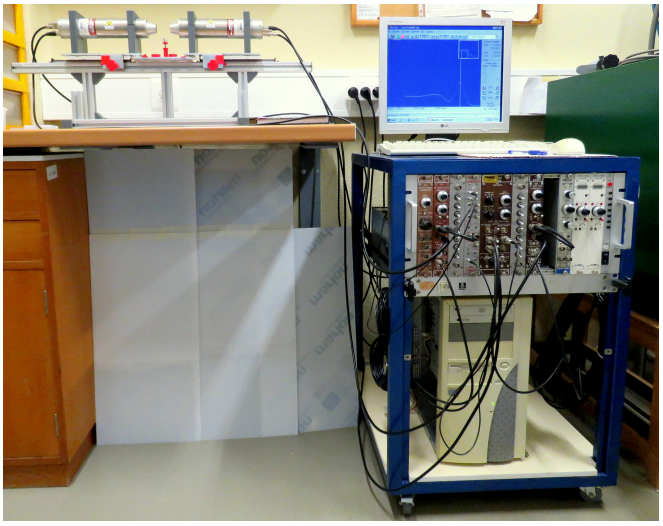

Figure 3.7: Complete experimental setup employed in this work.

3.4 Positron lifetime spectra analysis

A PALS analysis is later concluded using a software to deconvolute the acquired positron lifetime spectrum into recognisable components, characterised by useful parameters such as positron lifetimes and relative intensities of the annihilation channels in order to correlate them with important aspects of the free volume structure of the material analysed, such as free volumes' size, size distribution and concentration. In order to better visualise the function of the analysis software and the deconvolution process performed by it, a typical PALS lifetime spectrum analysed by the software and deconvoluted into its composing components is represented in *Figure 3.8*.

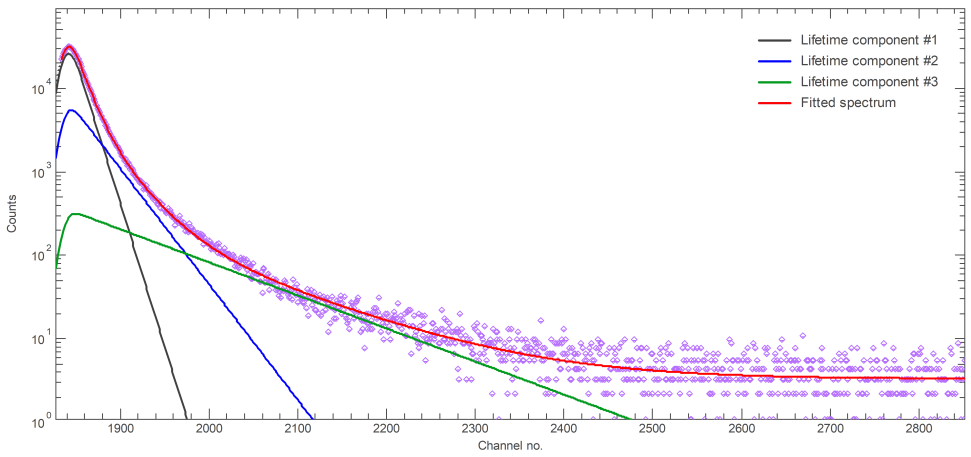

Figure 3.8: Deconvolution of a typical PALS lifetime spectrum into its respective lifetime components associated with the different positron annihilation channels, as produced by the analysis software.

3.4.1 Multiexponential Model

As a means to fully understand the role and functionalities of the deconvolution software, it is perhaps better to start by discussing the description of the positron lifetime spectrum according to the Multiex-

ponential Model. As pointed out in *Section 3.3.2*, a positron lifetime spectrum consists of a record of the lifetime of each positron that has annihilated in the sample under study. As we have seen, positrons can annihilate from multiple states when passing through a material, depending on whether the positrons or positronium atoms are free or trapped on one of the sample's free volumes and depending on the structure of these volumes. Furthermore, each of these states has its own characteristic positron lifetime as well as its own occurrence frequency, that determines the prevalence of a particular annihilation channel relative to the others and that is governed by the characteristics of the material in question. As a result, to each state is associated a positron lifetime function or lifetime component that represents the respective annihilation process and is characterised by both a lifetime and a relative intensity. According to the multiexponential model, each of these positron lifetime functions can be described as a decreasing exponential decay function. Therefore, an ideal positron lifetime spectrum is the result of the sum of n exponential decay components, each with its own lifetime and relative intensity, with n being the number of different states from which positrons have annihilated from when passing through the sample under study. Hence, an ideal positron lifetime spectrum is described by:

$$N(t) = \sum_{i=1}^{n} \frac{I_i}{\tau_i} \exp\left(- \frac{t}{\tau_i} \right) \tag{3.1}$$

with $\sum_{i=1}^{n} I_i = 1$, $N(t)$ being the time density of counts in the spectrum (although many authors refer to it simply as the number of counts in the spectrum) and τ_i and I_i are, respectively, the lifetime and the relative intensity of the i^{th} component.

In a typical analysis, the different positron functions to be obtained are treated as discrete parameters, however, there is also the possibility to regard each component as a continuous distribution of lifetimes, characterised by a mean value and a standard deviation. This approach takes into account the fact that free volumes in a sample may present a size and shape distribution and hence a positron lifetime one may arise. This alternative is also viable for when there are too many components in the spectrum close to one another, making it impossible to resolve them individually. Moreover, a combination of discrete lifetimes and continuous distributions of lifetimes in the same fitting procedure is also possible. In such a case, the ideal lifetime spectrum is given by:

$$N(t) = \sum_{i=1}^{m} I_i \lambda_i \exp(-\lambda_i t) + \sum_{j=1}^{n-m} I_j \int_0^{\infty} \alpha_i(\lambda) \exp(-\lambda t) d\lambda \tag{3.2}$$

$$\text{with} \quad \sum_{i=1} I_i = 1 \tag{3.3}$$

$$\text{and} \quad \int_0^{\infty} \alpha_i(\lambda) d\lambda = 1 \tag{3.4}$$

and where n is the total number of lifetime components in the spectrum and m is the number of discrete lifetime components, while, consequently, $n - m$ is the number of components in the spectrum described by a continuous distribution. Moreover, λ is the annihilation rate and $\alpha_i(\lambda)$ is the i^{th} distribution (probability density function) of annihilation rates of the decay channel, assumed to be a log-normal distribution, that is, a Gaussian distribution in a logarithmic scale. The software does not present the mean value and standard deviation of each $\alpha(\lambda)$ distribution, instead it provides the mean lifetime and standard deviation of the corresponding and much more useful lifetime distribution, taking into account

the relation $\lambda = 1/\tau$. These distributions, which are then functions of τ, are expressed as:

$$F(\tau) = \frac{1}{\tau\sigma'\sqrt{2\pi}} exp\left(-\frac{(ln\tau - ln\tau_0)^2}{2\sigma'^2}\right) \tag{3.5}$$

where τ_0 is the median value of the distribution and σ' is dimensionless and is sometimes called the scale or the shape parameter of the distribution. These two quantities can then be recalculated into the mean lifetime and lifetime dispersion and are these values that are presented by the program at the end of the fitting process.

However, the shape of a real positron lifetime spectrum is modified by a flat random background that accumulates under the spectrum and also by the finite time resolution of the detectors and associated electronics. The influence of the flat background is accounted for by simply adding its value, B, to the ideal spectrum equation as in:

$$N'(t) = \sum_{i=1}^{m} I_i\lambda_i \exp(-\lambda_i t) + \sum_{j=1}^{n-m} I_j \int_0^{\infty} \alpha_i(\lambda) \exp(-\lambda t) d\lambda + B \tag{3.6}$$

The influence of the time resolution, on the other hand, is a bit more complex to account for. The time resolution function, R(t), describes the response of the set of detectors and electronic modules to prompt coincidences. If it was an ideal set, when the detected lifetime is zero, a delta function would appear in the lifetime spectrum. In reality, the time spectrometer generates a prompt peak in the lifetime spectrum, *i.e.* the time resolution function, that is approximated by a sum of several gaussian functions, each characterised by its own relative intensity I_i, expected value, t_{0_i}, standard deviation σ and Full Width at Half Maximum (FWHM), with $(FWHM)_i = 2\sqrt{2ln2}\sigma_i$, resulting in:

$$R(t) = \sum_{i=1}^{n} \frac{I_i}{\sqrt{2\pi}\sigma_i} \exp\left(-\frac{(t-t_{0_i})^2}{2\sigma_i^2}\right) \tag{3.7}$$

Alternatively, $R(t)$ can be described as a gaussian function with exponential tails on both sides, a function known as Exponential Sided Gaussian (ESG) [77], which is frequently applied to model peaks with long tails. Besides *Equation 3.7*, the description of the time resolution function as an ESG function, which is defined by the equation below, is also accepted by the software.

$$\begin{aligned} f(x;\bar{x};\sigma;k_L;k_R) &= \exp\left(\frac{k_L^2}{2} + k_L\left(\frac{x-\bar{x}}{\sigma}\right)\right), \quad for \quad \frac{x-\bar{x}}{\sigma} \leq -k_L \\ &= \exp\left(-\frac{1}{2}\left(\frac{x-\bar{x}}{\sigma}\right)^2\right), \quad for -k_L < \frac{x-\bar{x}}{\sigma} \leq k_R \\ &= \exp\left(\frac{k_R^2}{2} - k_R\left(\frac{x-\bar{x}}{\sigma}\right)\right), \quad for \ k_R < \frac{x-\bar{x}}{\sigma} \end{aligned} \tag{3.8}$$

where $\bar{x}$ and σ represent, respectively, the mean value and standard deviation of the Gaussian core and k_L and k_R are the decay constants of the exponentials on the left and right side tails, respectively.

In practice, the time resolution is measured with the aid of a ^{60}Co radioactive source, whose decay scheme is represented in *Figure 3.9*. From this, it is clear that the radioisotope can decay by β^- emission to either a first excited state of the ^{60}Ni or a second higher state of the same specimen, with energies of 1332.492 keV and 2505.72 keV, respectively, with the former option having only a 0.12% branching

ratio, making the relevant decay the one to the higher excited state. Additionally, the deexcitation of both excited states of ^{60}Ni as the isotope transitions to its ground state results in the emission of a 1173 keV γ-ray, followed by a second 1332 keV γ-ray separated only by 0.713 ps. As these two gamma photons are emitted virtually in prompt coincidence, their detection by the PALS system, with the first emitted one taken as the start signal and the second as the stop signal, due to the system's limited resolving capability, should produce a peak resembling a gaussian function, whose description as either a sum of gaussian functions or an ESG function conveys the overall time resolution function of the system.

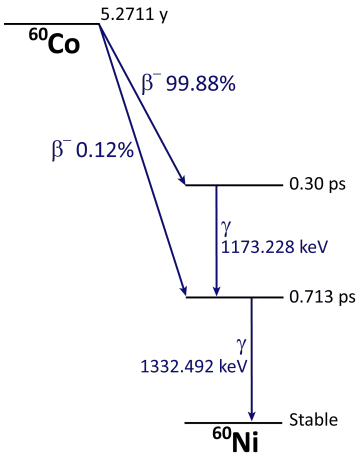

Figure 3.9: Decay scheme of ^{60}Co.

Whichever is the description chosen for the time resolution function, the real non-ideal positron lifetime spectrum, C(t), is thus the result of the convolution of such function with the sum of the theoretical description of the ideal spectrum and the background, viz:

$$C(t) = R(t) \otimes N'(t) = \int_0^\infty R(t - t_0)N'(t_0)dt_0 \tag{3.9}$$

3.4.2 Analysis software

The role of the analysis software is then to extract the physically meaningful parameters of the positron lifetime functions, resolution and background that compose the acquired experimental spectrum by fitting it into the multiexponential model description. For that purpose, and in an attempt to search for the best fitting process, several programs have emerged throughout the years that differ from one another on the mathematical process behind the fitting procedure. In fact, this procedure can be based on a least square fitting approach as is the case of PALSfit [78] and its earlier version PATFIT [79] and also of LT10 [80] and its predecessor LT9 [81], on a maximum entropy formulation of the Bayesian Theorem, around which the MELT software [82, 83] was developed; and also on a numerical Laplace inversion application, the method applied in the CONTIN software [84, 85]. All of these programs have had their fair share of applications and popularity within the PALS community, nevertheless, in more recent years, PALSfit and LT10 seem to be the ones more often chosen by researchers to be utilised in their PALS experiments.

Indeed, in this work, LT10 was initially intended to be used in the analysis of the experimental spectra

acquired as it presented many advantages: it is free; its analysis procedure is fairly straightforward; and it allows the simultaneous analysis of a set of experimental spectra in one computational run, therefore reducing the time consumed and complexity of the analysis. However, after exploring the program's functionalities and employing it in some preliminary analysis for several months, two crucial obstacles have been found that have led to a reconsideration of its application. The first of these disadvantages concerns the lack of information available about certain features of the software. Undeniably, despite the extensive amount of literature where the use of LT10 has been reported, there are several aspects regarding the analysis procedure that are not fully discussed. In particular, there are certain options and constraints on a few parameters, whose function and initial value to be introduced are not as clear-cut as it initially might seem, which are not at all addressed in the literature on the topic of spectra fitting with LT10. Furthermore, clarifying some aspects about the software with its developing team is also not very simple as further development of the program has been essentially nonexistent for quite a few years. Hence, it became clear that it was going to practically impossible to obtain an answer to some of the difficulties encountered while exploring the program, difficulties which were viewed as preventing a reliable analysis of the acquired experimental spectra. On the other hand, it was found that the final results provided by LT10 concerning the parameters of the positron lifetime and time resolution function are heavily dependent on the initial values set for them in the beginning of an analysis run. These initial values are required by the program as they are essential for the convergence of the fitting process and consist of educated guesses made by the user on the expected results for the parameters. However, an accurate knowledge of the expected values for all the desired parameters is not always possible. This would not present an issue if the program consistently rendered the same results despite having been provided with different initial guesses on a somewhat broad range, nonetheless, this is not the case. Indeed, the program is not very stable and a slight deviation of the initial value for a certain parameter forces an entirely different convergence of the model, translating in rather distinct results for all of the desired parameters, which, of course, deems the analysis procedure by LT10 as unreliable.

With all of this in mind and after careful consideration, it was decided that the best option was to dismiss LT10 and instead employ the PALSfit software. Similarly to LT10, PALSfit is based on a least square fitting approach, meaning that the experience acquired with LT10 could also be applied to PALSfit, which also provides a very straightforward approach to their analysis process. Furthermore, in spite of not being free and not allowing the simultaneous evaluation of a number of experimental spectra in one computational run, PALSfit came to solve the problems found with the former software. In fact, likewise what happened with LT10, the literature is of little help in clarifying some technical questions and difficulties that have arisen when experimenting with the software. Fortunately, however, these have readily been answered by the software's developing team, who is still working on new upgrades and developments, and with whom establishing contact was extremely easy. In addition, unlike LT10, the program always produces the same estimates of the fitting parameters after convergence, irrespective of the initial guesses. Consequently, it was concluded, that PALSfit would produce a simple and reliable analysis of the acquired experimental spectra and therefore should be the program used and so the PALSfit3 program, the version 3 of the PALSfit software was employed in our work.

The PALSfit program was developed by the Risø Campus of Technical University of Denmark and is a mature program that has been thoroughly tested and upgraded over a number of years. The program is divided into two modules: ResolutionFit and PositronFit. In the ResolutionFit module, the appropriate description of the time resolution function of the PALS system is extracted by fitting an experimental spectrum to the multiexponential model (*Section 3.4.1*), acquired under the same experimental conditions as the spectra of the other materials under study. The description obtained for the time resolution function can subsequently be imported to PositronFit where the same model is fitted to the experimental spectra. But now, because the time resolution function is already determined and fixed, the lifetimes and respective relative intensities of the lifetime components can be estimated.

3.5 Samples

One of the main goals of this work is the optimisation of a PALS spectrometer, by successive revisions and improvements to both the detection and electronic systems. In order to do so, lifetime spectra of materials with well known behaviour have to be acquired with the experimental setup and the positron lifetimes found from their analysis have to be compared with the values reported in literature. While the results obtained are not similar to those expected, then further improvements, tests and alterations to the parameters and properties of the many components comprising the setup must be performed and only when the attained lifetime spectra of these reference materials accurately reproduces the ones published in a plethora of studies from the last six decades is the optimisation process concluded.

In a PALS setup optimisation process, the most commonly examined materials tend to be pure metals and semiconductors, which are selected for two major reasons. The first is that these types of material are the ones most studied throughout the years and therefore a much larger and more reliable database of positron lifetimes in them has been put together. On the other hand, metals and semiconductors tend to exhibit only one short lifetime component in their spectrum, associated with the annihilation of positrons in the bulk of the material, which greatly facilitates a comparison of the results experimentally acquired with the values found in literature. Even in cases where that is not true and more than one positron function is present, corresponding to positron annihilations in trapping defects, typically the concentration of these defects is below the sensitivity limit of the PALS technique, which is approximately 0.1 ppm [86], resulting in that one lifetime component is much more intense than the other ones, whose contributions are negligible.

The existence of a single lifetime component in a spectrum is an enormous advantage for the analysis procedure. When a lifetime spectrum is acquired, apart from the background radiations, the undesired annihilations happening in the surrounding environment and the effect of the spectrometer's time resolution, there is a fourth external contribution to the spectrum, known as the source correction component. This term appears due to the fact that when positrons are emitted by the radioactive source, they are required to pass through the source itself and the involving Kapton® HN foils in order to reach the sample pieces under study. During this crossing, despite the tiny volume of the source's crystallites and the small thickness of the Kapton® HN foils, a non-negligible number of positrons will annihilate within

this set, creating an additional lifetime component in the spectrum. Therefore, a previous knowledge of the time resolution of the system and of the source correction terms is essential in order to correctly analyse a spectrum and accurately extract the lifetime components associated with annihilations in the sample under study. Then, for the purpose of determining these extrinsic contributions, an analysis of a reference sample must be carried out. This process is remarkably simpler and more accurate if the reference sample exhibits mainly a single component with a short lifetime and consequently, one metallic or semiconductor material is usually chosen to act as the reference sample used for this intent.

Besides metallic and semiconductor reference samples, it is also important for the scope of this work to study polymeric reference materials, given that after the optimisation of the spectrometer, it is intended to be applied mainly to the study of polymeric materials developed by the research group. The biggest difference from metals and semiconductors is that polymers tend to exhibit several lifetime components in a positron lifetime spectrum, stemming from annihilations of not only positrons in the bulk of the material, but also from positrons and/or Ps atoms trapped in its free volumes, making the analysis of spectra of this type of material a more complex procedure. Therefore, in order to become acquainted with such spectra and to guarantee a correct spectra analysis and interpretation of the results for the ensuing study of the group's samples, it is essential to firstly experiment with a few reference polymers, whose analysis process is validated by comparing the results obtained with values in the literature.

In summary, three types of samples are analysed in the course of this work: metallic and semiconductor reference materials, polymeric reference materials and finally radiation processed polymer-based materials, developed by the research group.

3.5.1 Metallic and semiconductor reference samples

In order to select the metals and/or semiconductors to be studied, three factors have to be taken into account: the positron lifetime in the material should be as short as possible, which is essential to an accurate determination of the time resolution and source correction terms; the material must have been thoroughly studied and have several well documented literature values of positron lifetimes; and the lifetime results obtained for the material in separate studies must not greatly disagree from one another, guaranteeing, together with the previous requisite, the reliability of the positron lifetime found from averaging the values reported in different studies. For this intent, a compilation of the results obtained in numerous studies for the positron lifetime in a large number of pure metals and semiconductors has been performed, considering only the lifetime values associated with the annihilation of positrons in the bulk of the material. Despite the abundance of studies contained in this compilation, there are, of course, endless more. However, the discrepancy between the number of results presented for each material somewhat represents the discrepancy between the volume of studies published addressing the analysis of each particular material. The literature experimental values of the bulk lifetime of the most extensively studied pure metals and semiconductors are compiled in *Table B.3*, presented in *Appendix B*, alongside the respective average lifetime value and standard deviation. All materials are represented by their chemical symbol, with the exception of the EG-Si, which stands for electronic-grade silicon. EG-Si is intended for microelectronic device fabrication and use as raw material for the growth of single-crystal

silicon in the manufacturing of silicon wafers and therefore is a highly-purified version ($> 99.9\%$) of the metallurgical-grade silicon (MG-Si), here just represented by Si, with an extremely low impurity level.

It is visible that there is not a single material which complies in perfection will all the mentioned requirements as neither of them combines the shortest positron lifetime, the most number of studies where it is featured and the best possible agreement between results from different publications. Therefore, in order to select the metals and/or semiconductors to be analysed in this work, apart from taking into consideration such factors as price and availability of the materials, a compromise between the compliance of the different requisites must additionally be considered. For our work, we settled for three materials, namely copper (Cu), nickel (Ni) and electronic-grade silicon. In the case of copper and nickel they were chosen as not only are they not very expensive and easily obtainable but also fulfil all the requirements rather well, as they have some of the shortest bulk lifetimes among all materials and have been exhaustively analysed since the early days of the PALS technique, with reported values in quite reasonable agreement. On the other hand, the EG-Si was selected partly because it had already been acquired for other purposes and thus was promptly available for analysis in the laboratory, but also due to the good consensus between the few reported results, which are scarce due to its high price. On top of that, EG-Si was selected due to the intention to, before carrying on to polymeric samples, study a material showcasing a slightly longer positron lifetime to ensure that the agreement between our results and the data available in literature was not limited to very short lifetimes.

The copper samples analysed in this experiment were high purity polycrystalline ones supplied by MaTecK GmbH [87], with a thickness of 1 mm and a 99.99+% purity. Since the analysed samples should have a thickness of at least twice the 550 keV, an energy close to the end-point of the continuous energy spectrum of the positrons emitted by ^{22}Na, positron range in them, which in copper is of 0.332 mm [88], the Cu samples should be at least 0.664 mm thick, which means that the chosen samples are suitable for the analysis. Similarly, the high purity polycrystalline nickel samples were acquired from MaTecK GmbH, with a purity of 99.99%. Furthermore, they are 1 mm thick, which means that the samples more than satisfy the minimal required thickness of 0.64 mm [88]. At last, the EG-Si samples have a thickness of 600 μm, which is smaller than the recommended thickness of 2.14 mm [88] and therefore, when performing a data run acquisition, several sheets of the material must be put together in close contact on each side of the source.

Annealing

Although it could be expected that high purity metal foils present a single positron lifetime component with a value close to the ones reported in literature, the reality is that the manufacturing processes involved in their production typically create defects and atom dislocations in the samples, therefore generating trapping sites where positrons might get trapped and consequently annihilate with a different lifetime from that of free positrons. In fact, most analysis involving as-received samples tend to exhibit spectra with either a second lifetime component or both effects crammed up into a single component but with a lifetime rather different from the expected one. However, since a single lifetime for metals is desired, a commonly adopted way in the PALS community to achieve this is by reducing the defect

concentration to a such a degree that is below the PALS technique sensitivity, which is achieved by making the acquired samples undergo an annealing process. Indeed, the values published in literature usually come from the analysis of annealed samples, instead of as-received ones, even if not explicitly asserted.

When annealed, the samples are heated up to a temperature above their recrystallization temperature, in fact corresponding to a high percentage of its melting point for a suitable length of time, They are then cooled down back to the ambient temperature, by either leaving the sample to slowly cool down or by quickly quenching it in water, depending on the metal in question. This procedure eliminates the defects within the material as the heating causes the atoms to move through the crystal lattice and redistribute themselves, eradicating the sample's defects in the process, and the cooling off allows the material to recrystallise. The annealing process can be divided into three separate stages, namely recovery, recrystallization and grain growth. In the recovery stage, the temperature is still being raised and it is then that dislocations sites inside the material are removed and the internal stresses they caused are relieved. Secondly, once the final temperature is achieved, new grains tend to nucleate and grow, replacing the original deformed grains. At the last stage, during the cooling process, these new grains develop further, leaving the material with a more cohesive internal structure.

As a single lifetime component with a similar value to the ones presented in the references was also expected in our case, it was decided to make the copper and nickel samples undergo an annealing process, at the High Temperature Synthesis and Crystal Growth Laboratory, a facility operated by the Solid State Group of C2TN, IST. For that purpose, both the Cu and Ni samples were cut in two so that one half could be annealed, while maintaining a non-annealed second half, in case the measurements with the as-received samples would need to be repeated. The annealing process was performed in a furnace under a vacuum of 1 $\times 10^{-1}$ mbar, where the samples' temperature was raised at a rate of 100 °C/h up to the desired annealing temperature, corresponding to 75% of their respective melting point, which for copper means 813 °C and for nickel is equal to 1090 °C. This temperature was held constant for two hours, after which the furnace was shut off and the materials were left under vacuum to naturally cool off back to ambient temperature.

3.5.2 Polymeric reference samples

Since the main intention behind the analysis of polymeric reference samples was to get acquainted with the lifetime spectra obtained from polymeric materials and their subsequent analysis, the choice of materials to be analysed rest only in two factors. These were the abundance of studies that reported positron lifetimes observed in said material and the level of agreement between the results presented in each publication, in order to guarantee the reliability of the values to which our results would be compared later on. Therefore, in the end, our choice fell upon two of the most easily obtainable and most extensively studied polymers in the PALS community, Polytetrafluoroethylene, also commonly referred to as Teflon® (commercial brand name), and Polycarbonate (Bisphenol A).

The Commercial Teflon® samples selected for the experiment were supplied by RS AMIDATA [89], with a thickness of 2.36 mm. The range of 550 keV positrons in the material is 1.095 mm [88] thence

the Teflon® samples should be at least 2.19 nm thick, which the chosen samples certainly are. Being a polymer, Teflon® usually exhibits more than one positron lifetime component in its spectrum, as additional annihilation phenomenons are not only possible but likely to take place inside its structure. Generally three lifetime components are considered although four are also often reported, as can be verified from the literature lifetime values and associated relative intensities compiled in *Table B.1*, featured in *Appendix B*. The explanation behind the origin of each lifetime component was disputed for several decades, until a consensus was reached that agreed that either the largest or two largest components were attributed to the pick-off annihilations of trapped o-Ps atoms, while free positron annihilations were assumed to give rise to the second shortest one and finally the shortest component was considered to originate from the annihilations of free p-Ps atoms, even though it is speculated that it may also contain contributions from other short lived annihilation channels. Therefore, the number of lifetime components considered in our analysis of the Teflon® samples will be either three or four, depending on which corresponds to the best fitting of the multiexponential model to the experimental spectrum and it will be expected that the results obtained are somewhat similar to the guideline values here presented.

On the other hand, the Polycarbonate (Bisphenol A) samples analysed in this work were acquired from Brett Martin [90] and have a thickness of 1.5 mm, which is not bigger than double the 550 keV positron range in this particular material, which is equal to 1.76 mm [88]. Hence, when analysing this polymer, either several sheets are stacked in close contact on each side of the source, which was the method employed in our work, or an additional layer of a metallic or semiconductor reference material is put on the edge of the source+samples sandwich. Unlike Teflon®, the number of positron lifetime components expected in a Polycarbonate spectrum as well as the annihilation mechanism at the origin of each one have never been in dispute. Although some studies report only the longest one, generally three components are considered, originated from the same annihilation channels that were ultimately accepted to be at the origin of the Teflon® lifetime components. Given the strong agreement between the values reported in literature, in the analysis of the Polycarbonate samples, we expect to observe three lifetime components with values close to the ones presented in *Table B.2*, displayed in *Appendix B*.

3.5.3 Polymeric samples

At last, four polymeric samples developed by the research group were studied. Two of them consisted of graft copolymer films of PE-g-HEMA (Polyethylene-grafted-Hydroxyethyl methacrylate). One of them, hereafter referred to as Sample 1, was a PE-g-HEMA film with 403% of graft, prepared by gamma irradiation, with a total dose of 9 kGy and at a rate of 0.3 kGy/h, in the absence of oxygen. The other one, henceforth labelled as Sample 2, was a PE-g-HEMA film with 158% of graft, also prepared by gamma irradiation in the absence of oxygen with a total dose of 10.5 kGy and at a similar dose rate. The remaining samples consisted of Chitosan/PVA based membranes. One, thereafter designated as Sample 3, was a Chitosan (Medium Molecular Weight) 2% / Polyvinyl alcohol 5% (Weight by Volume - W/V) membrane, while the other, referred to as Sample 4 hereinafter, was a Chitosan (Medium Molecular Weigh) 2% / PVA 5% (W/V) / Gelatin 2% membrane, both prepared by gamma irradiation in the absence of oxygen, with a total dose of 10 kGy. The samples are displayed in *Figure 3.10*

(a) Sample 1 (b) Sample 2 (c) Sample 3 (d) Sample 4

Figure 3.10: Polymeric samples produced by the research group and analysed in this work.

Finally, it is important to point out that, being polymeric samples, the range of positrons in them is relatively large, while their density is rather small, which implies that the samples should be considerably thick in order to completely stop all positrons injected into them. However, the samples provided are very thin, meaning that for the acquisition of these spectra, the set of polymeric sample in question + radioactive source had to be surrounded by a reference metallic foil in each side of the set, as represented in *Figure 3.11*. A reference metal with a very short lifetime component is preferred for this purpose as its contribution to the spectrum amounts solely to an extremely short extra lifetime component, unlikely to be confused with any of the polymer's lifetime components, hence, the annealed reference nickel samples were used in our case.

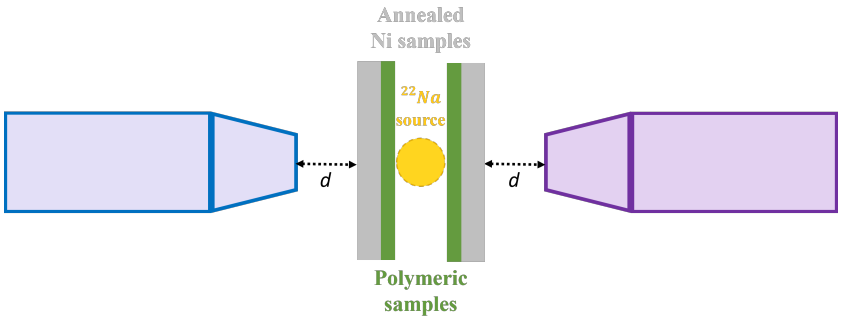

Figure 3.11: Representation of the source+sample sandwich, positioned at the centre of the two detectors, for the case of the polymeric samples.

Chapter 4

Optimisation of the PALS setup

Prior to the beginning of this work, a spectrometer had previously been assembled at the group's facilities. However, the experimental setup had not yet been fully and properly calibrated and refined and a deep understanding of the steps, tools and methods involved in the analysis of the spectra acquired had still not been completely attained. Therefore, as part of two pivotal aspects of this work, not only was the experimental circuit subjected to several enhancements but a comprehensive set of data acquisition and analysis tools was also developed. These two elements then put together ultimately resulted in that the desire to obtain a spectrometer working in optimal conditions and readily available for an accurate analysis, mainly of the macromolecular materials developed by the research group, came to fruition.

4.1 Improvements to the experimental setup

4.1.1 Additions and alterations to the experimental setup

The first improvement stage of the experimental setup comprised a series of alterations and/or additions to the actual physical assembly of the PALS spectrometer. These modifications were essential not only for a better manipulation of the system's components but also for guaranteeing more reliable and accurate results in the end.

Sample holder

One important aspect of any PALS experimental setup is the sample holder positioned between the two detectors where the source+samples sandwich is fixed throughout a measurement. At first, the sample holder was solely comprised of a suspension structure, with an alligator clip at the end, where the samples and source were grasped. This structure was then planted in any desired position relative to the detectors, though it was usually chosen to be in such a way that the source+sample sandwich would be suspended in the centre between the detectors.

Throughout a PALS experiment, it is utterly important to have the source+samples sandwich highly compacted, in an effort to guarantee that the source does not move within the sandwich and possibly slide off of it, ensuring thereby that the sample's disk completely encapsulate the source at all times. Furthermore, it is also extremely important that the whole set is always in extreme close contact, pre-

venting air to get between the layers and interfere with the final results by adding an additional intense lifetime component to the spectrum from positron annihilations in air. Furthermore, it is also essential to guarantee that the sandwich remains fixed in the same place during an entire measurement, given that the distance from the detectors to the samples influence the results obtained. In fact, if the distance between the detectors and the samples was altered during an experiment, then the photons to be detected would have to travel different lengths and therefore be detected at different times. This would result in events that correspond to different bins in the lifetime spectrum, thus corrupting the final results by creating an altered and incorrect histogram. Just to give an idea of the magnitude of the time differences involved, if the distance between the detectors changed as much as 1 mm, the registered time difference would be of 3.3 ps, which is fairly substantial for the range of times generally detected in our experiments.

The original sample holder could not assure neither a full compactness of the sandwich nor a fixed position for it throughout a measurement, as a simple accidental touch could substantially alter its distance from the detectors. Hence, a new sample holder had to be designed and incorporated into the detection assembly and the final product can be observed in *Figure 4.1*. This structure, which now complies with the vital conditions demanded from a sample holder, is constituted by: a base with four screws, that allows the entire structure to slide along the grid and hold a fixed position at any desired distance from the detectors; and the supporting structure itself, that contains a stand where the set of sample foils and ^{22}Na source is positioned, secured and properly constricted with four clamps. Additionally, the supporting stand can be lowered or raised, in order to accommodate samples from all sizes, since these must be always aligned with the centre of the detectors' conical entrance.

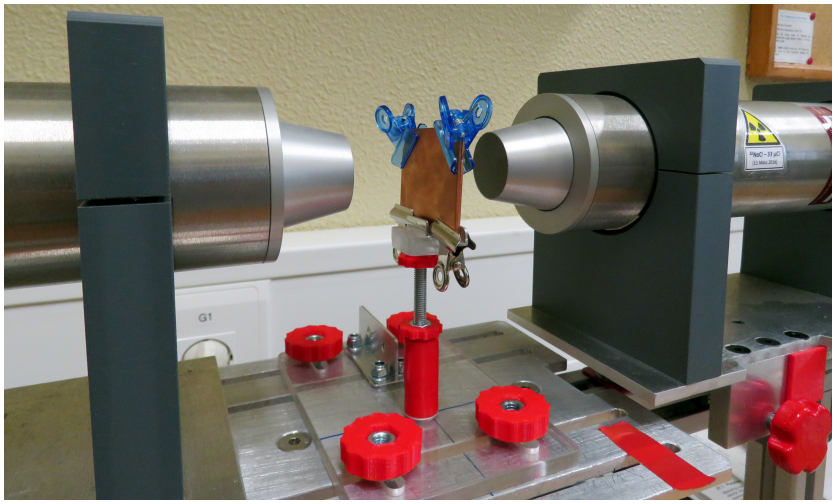

Figure 4.1: New sample holder for our experimental setup.

Measuring scale

Apart from maintaining a stipulated distance from the sample and source sandwich, the detectors must also be equally spaced from this central set. The reason for this is that otherwise the photons would be forced to travel longer distances to reach one of the detectors and then the time difference between the arrival of the start and stop signals as well as the position of the event in the lifetime spectrum would be greater or smaller than expected. Therefore, knowing the precise distance of the scintillators

in the detection assembly is of the utmost importance. On top of everything else, this information is also convenient if a certain measurement is meant to be replicated as the position of the detectors, or in reality their count rate (number of events they are capable of detecting in a certain amount of time), greatly influences the results obtained.

Originally, there was no mechanism for measuring the distance of the scintillators in the detection assembly, however given the obvious advantages, a measuring scale was crafted and integrated into our experimental setup, with the intent to give us a practical and consistent way to assess this distance. This measuring scale consisted of two printed scales and two pointers that were designed using the Fusion 360 software [91] and 3D printed afterwards. The scales were glued beneath each detector onto the side of the rails where the detectors rest, with their 0 pointing inwards, coinciding with the point in which the respective detector is in contact with the sample holder at the centre of the assembly. The pointers were then attached to the base of each detector, pointing out to the respective scale, where the distance of the detectors from the sample holder could be read, in cm, as can be contemplated in *Figure 4.2*.

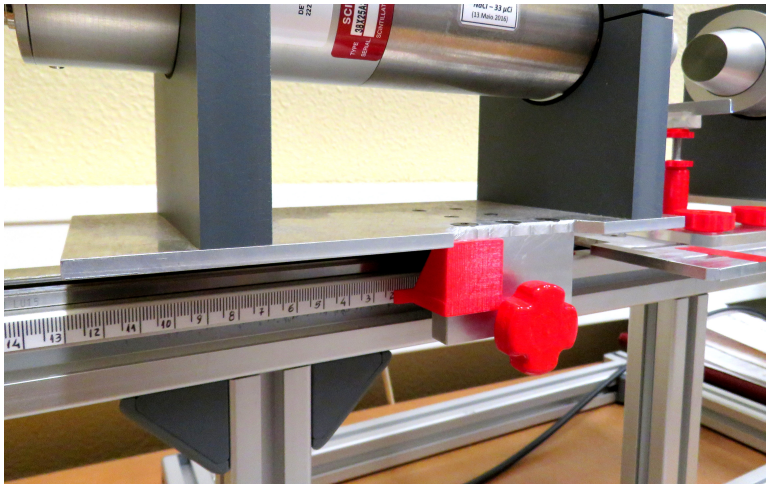

Figure 4.2: The measuring scale implemented in our detection assembly.

Computer monitor

One additional modification to the experimental setup concerned the computer monitor employed to visualise the spectrum being acquired and act on it, through the MAESTRO software, with some preliminary analysis tools. Initially, we were using a Cathode Ray Tube (CRT) monitor for that effect. However, it was pointed out that the CRT's high voltage power supply and its variations might generate an electromagnetic field that would interfere with the operation of the close by photomultiplier tubes, which depend on their internal electric fields, created between each dynode level, to multiply the electron flow and produce their output signal. In the end, it was then decided to replace this CRT monitor with a newer flat one, that did not rely on the same technology and therefore presented no problem to the operation of the remaining components of the experimental circuit.

Ventilation unit

Finally, a ventilation unit was assembled below the set of NIM electronic modules, namely the two High Voltage suppliers, the two CFDDs, the FC Unit and the TAC, in order to dissipate the heating caused by

their operation. This was done to improve the stability of the system, as the modules' operating conditions and performance are somewhat dependent on their working temperature, with the best performance achieved when the surrounding temperature is not excessively high.

4.1.2 Calibration of the detection system and electronic modules

A second step towards the optimisation of the experimental setup concerned the proper calibration of the detectors, their coupled photomultiplier tubes and associated electronic modules, through the careful definition of their ideal operating parameters, which was critical for two reasons.

The first related to the zero channel drift observed in lifetime spectra acquired during some early on experiments with the setup. The zero channel corresponds to the bin in the lifetime or the time resolution histograms with the maximum number of counts and should always be the same throughout a data acquisition run, as long as the operating conditions remain constant. However, it was verified in these preliminary measurements that even maintaining the exact same working conditions, which also included external ones, such as the room's temperature and humidity, ensured by an air conditioning unit, this zero channel greatly shifted between a wide range of channels, either within the same measurement or at the beginning of a new one. This shift, which presented no discernible shift pattern or perceptible reason behind it is of great concern as it causes an artificial broadening of the lifetime spectrum or the time resolution peak, leading to a faulty interpretation of the histogram by the fitting programs, resulting in unreliable and most likely incorrect values for the positrons' lifetime or the time resolution, respectively. Therefore, an attempt must be made to eliminate or at best alleviate this undesired phenomenon and a meticulous fitting calibration of the detection system and electronic models might be key.

The other aspect which may be improved by a correct definition of the working parameters is the time resolution of the system, which is intended to be as small as possible, since the better the resolution is, the smaller the influence and even distortion on the acquired lifetime spectra is and the more reliable and accurate the spectra fitting and therefore the results are. The time resolution is commonly influenced by the geometry and type of scintillator used, although in our case little can be done in that regard, as well as by the PMTs and electronic modules' intrinsic characteristics and operating parameters and even possibly by impedance mismatches between the modules' inputs and outputs.

Time calibration In order to monitor the influence of the many alterations and experiments on the variation of the system's time resolution, as well as to allow the analysis of the lifetime spectra that are to be obtained, firstly, the time calibration of the overall acquisition system had to be assessed. This corresponds to the time value of each channel in the histogram and is used during the spectra analysis to transform the channels in the acquired histograms into time, for the assessment of lifetime results.

To execute this, the output of a pulse generator module was divided and fed to the inputs of both CFDDs, whose discriminating windows' upper and lower thresholds were defined, respectively, to their maximum value and to a value slightly above minimum, to ensure that no noise was detected. Each CFDD output was then passed through an associated delay module and subsequently sent to the TAC, functioning as either the start or stop signal. For a particular set of time delays imposed on the start

and stop signals, the result could be observed in the histogram as one narrow peak centred around a very distinctive channel number. Additionally, by varying the stop signal's time delay, whilst keeping the time delay for the start signal constant, several of these peaks could be observed in the spectrum centred around different channels and for each time delay change of a known amount, the centroid channel of the respective peak was registered. This created a series of data points of peak channel variation (variation from the peak channel observed for when there was no variation in the stop signal's time delay) in terms of time delay variation (variation from the original delay imposed on the stop channel), that allowed for a relation between channel and time, in other words, the system's time per channel value, to be assessed.

Because the time calibration must be executed every time any significant alterations are made to any setup component or parameter, a final time calibration was performed after all calibrations, improvements and parameter adjustments took place for the last time. For that final calibration, the data acquired, together with the linear fit that provided the value for the time per channel is presented in *Figure 4.3*.

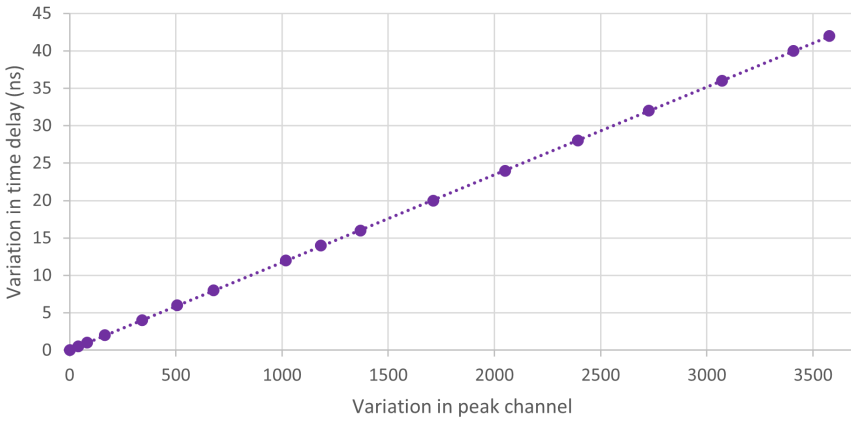

Figure 4.3: Determination of the system's linear time calibration.

The fit produced a time per channel value of 11.722 ps/channel and presented a reduced χ^2 or χ^2 per degree of freedom (DOF) of 0.999986. This is a statistical tool that assesses the fitting quality or in other words the degree of agreement between the experimental provided data and the fitted curve and whose value is expected to be close to 1. It is only when this is observed that the one can be assured of the quality and reliability of the results.

Background time and energy spectra Another important aspect to take into consideration before any further measurements are carried out, either for the determination of the time resolution or for the study of materials, is the assessment of the possible contamination of the acquired spectra by background radiation, in order to ensure that the results obtained are not significantly corrupted by this presence.

With this intent, a first background spectrum was acquired in the time domain, with the usual experimental setup configuration and with the final values found for the CFDDs' discriminating windows, whose process of determination is explained ahead, that corresponded to the ones that would be used for all the final measurements in this work for both the reference and polymeric samples. This is done so since our main objective in acquiring these spectra concerned the influence of the background radiation on future results attained from any PALS experiment.

A second background spectrum, this time in the energy domain, was collected by connecting the

output of one of the PMTs to the ADC, although, since the former is a negative signal and therefore not accepted by the ADC, it was firstly passed trough an amplifier module, where its inversion was performed. In order to obtain a spectrum of counts *vs* energy, an energy calibration is needed to transform the channel scale in the histograms into an energy one. To do so, an energy spectrum of the ^{60}Co source was acquired and is now represented in *Figure 4.4*.

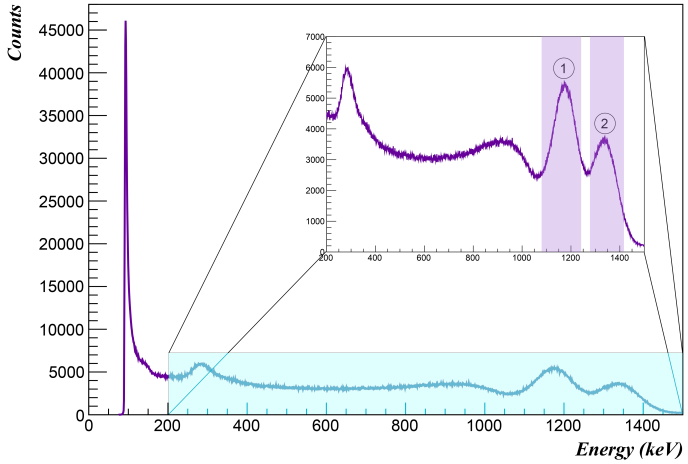

Figure 4.4: Acquired ^{60}Co radioactive source's energy spectrum.

From this spectrum, the photopeaks corresponding to the source's emission of the 1173 keV and 1332 keV γ-rays, represented, respectively, by numbers 1 and 2 in the figure, were identified, along with their corresponding centroid channel. Then, with these two (channel, energy) data points, a linear fit was drawn, resulting in the following formula for the energy associated to each channel in the histogram:

$$E = 0.834\ keV/channel \cdot \#channel + 75.6147\ keV \tag{4.1}$$

The background time spectra was collected for 230729 seconds, which corresponds to approximately 64 hours and is now exhibited in *Figures 4.5(a)*, whilst its energy counterpart, represented in *Figure 4.5(b)*, was acquired for solely 50304 seconds, roughly 14 hours.

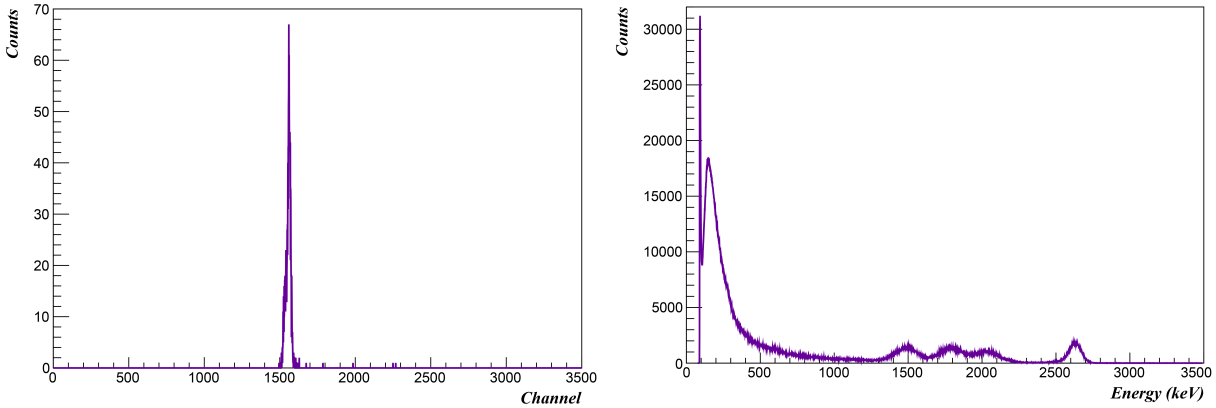

(a) In the time domain

(b) In the energy domain

Figure 4.5: Acquired background spectra.

From the observation of the spectra, it becomes clear that the background radiation makes no significant undesired contribution to the regular lifetime spectra. In fact, not only is the most prominent energy

range of the background radiation, of only a few keV, of no interest to us for further PALS measurements, as it will become clear in a moment, but also, in 64 hours, a time period far greater than the usually acquisitions times employed in our work, only a few hundred very short lived events have been registered.

Afterwards, as a first measure, all the experimental circuit was disassembled and reassembled, in order to search for any component which may need replacement or repair and indeed a few cables connecting the different modules were substituted as some were not in the best of conditions and others were not impedance appropriate. These substitutions did improve slightly both the zero channel drift and the time resolution value, although it was not enough and a second stage ensued, namely an iterative calibration of each piece of equipment.

Photomultiplier tubes

Starting from the beginning of the data acquisition chain, the only parameter of the PMTs needed to be calibrated is their operating voltage. The value selected for this quantity heavily depends on both the requirement to have an output signal with a suitable voltage for the entrance of the CFDDs but also on the value of the output rise time exhibited by the PMTs when that particular voltage is applied to them. Rise time is a parameter used to evaluate the ability of a circuit or component to respond to fast pulses at its input and is defined as the time taken for a signal to cross from 10% to 90% of its final or steady-state value, in other words, how long it takes for a signal to be formed. Because a precise timing register is so vital in the PALS technique, it is desired that each component presents the smallest rise time possible so as not to add any imprecisions to the time registered.

Given that the lower and upper voltage limits of the discriminator windows of the CFDDs have each a maximum threshold of -5 V, it was established that the signals outputted by the PMTs when processing the pulses coming from the radiation of the ^{22}Na source could then have at maximum an amplitude of -4 V, in order to ensure that the top limit of the CFDDs thresholds was never exceeded. However, the ORTEC accompanying script for the installation and further experiments using a Positron Annihilation Lifetime Spectrometer unit [92], that was used as a guideline for the assembling and definition of some basic parameters throughout this work, recommended that the maximum PMT output voltage was approximately -2 V. For the range of applied high voltages that resulted in the PMTs having output voltages ranging from -4 V to -2 V, the rise time of both the cathode and first dynode of each PMT was measured, as a means to verify which of the PMTs exits presented the best rise time. In order to do this, the ^{22}Na source was positioned between the detectors and the outputs of each PMT were then connected to the oscilloscope through a 50 Ω terminated cable, where the signal exhibited allowed both the voltage and rise time of the pulses to be computed.

It was noted that in the specified voltage range not only did neither the cathodes' nor first dynodes' rise time varied for either PMT but also the cathodes presented a smaller rise time of 3.2 ns and 3.5 ns, for the start and stop PMTs, respectively. As a result, the cathodes were then chosen as the output of each PMT to be inputted in the respective CFDD and give continuity to the signal processing chain. Since the applied voltage had no influence on the output signals' rise time and since no advantages were seen in employing higher voltages, it was decided to follow the manual recommendations and settle for

such a high voltage that bounded the maximum amplitude of the PMTs to be -2 V in the presence of the ^{22}Na source, which meant adjusting the high voltage to a value of -1865 V and -1901 V, for the start and stop PMTs, respectively.

Constant Fraction Differential Discriminators

The CFDDs are undeniably the most demanding module, requiring the most work to be properly calibrated out of all the electronic components in the setup. Firstly, they were set to operate in the differential discriminator mode, which signified that, in order to be accepted for further processing, the input signal's voltage had to fall within the preset amplitude span. Additionally, the constant fraction mode was activated, meaning that it was actually a generated bipolar pulse, created from manipulations on the original input signal, that was accounted for when marking the arrival time of the signal.

Blocking Width One of the simplest parameters to define in the CFDDs is the value of their blocking width, a feature aimed to prevent a phenomenon designated as pulse pile-up. This refers to a situation where one signal is already travelling along the electronic circuitry and, because the processing by the various NIM modules takes up a certain amount of time, it might happen that it is not fully processed before a second pulse is detected and enters the processing chain. Then, if there is only a scant time difference between the two incoming signals, they are treated as one, with the convolution of the pulses' amplitudes and widths creating a false signal in the recorded spectrum. In an attempt to prevent this, a blocking signal is generated any time a signal arrives at an CFDD, preventing any new signals from being accepted for a time period equal to the blocking signal's width, or simply blocking width. For our PALS setup, this quantity was set to 1 μs, providing therefore ample processing time and avoiding the undesirable pile-up effect.

WALK potentiometer Although, theoretically, the constant fraction mode of the CFDDs renders an input pulse's amplitude-independent timing register, therefore eliminating the effect of walk errors, in order to achieve this in reality, an adjustment to the WALK potentiometer is needed.

The signals arriving at the CFDDs originated in the decay of the ^{22}Na radioactive source were observed, by displaying the Constant Fraction Monitor (CF MON) output of the CFDDs in the oscilloscope, while triggered externally by the CFDDs' timing output signal. Without the proper tuning of the WALK, a front panel screwdriver-adjusted potentiometer whose value is read with a voltmeter in the respective monitor, the generated bipolar signals of different amplitude do not cross the zero baseline at the same time. Hence, whilst observing these signals, for both CFDDs, the potentiometer was carefully regulated until the zero crossing of signals of all amplitudes was at its possible narrowest. In order to better understand this WALK potentiometer adjustment process, *Figure 4.6* shows the CF MON signal as visualised in the oscilloscope in two distinct scenarios. In the left figure, the zero crossing of different signals happens at different times, so evidently the WALK potentiometer has not been adjusted yet in this case. On the right picture, however, the potentiometer has clearly been properly tuned as the ideal situation has been achieved of the zero crossing being, as possible as can be, at the same exact time for all detected signals.

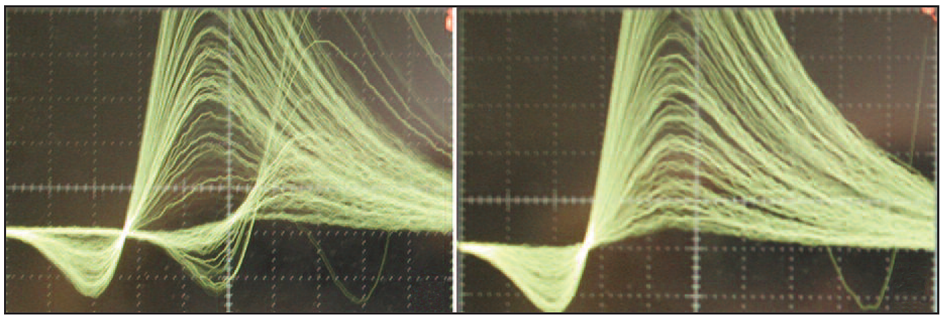

Figure 4.6: WALK potentiometer adjusting process, showing an improper WALK adjustment (left figure), and the ideal WALK adjustment (right figure). Adapted from [92].

These readjustments were performed whenever there was an alteration to the setup prior to or concerning the CFDDs, such as to the PMTs' operating voltage or to the constant fraction delay cable length, as they are indispensable to maintain the best possible timing resolution. As a result of the last adjustment, performed after setting all final operating conditions for the PALS spectrometer, the WALK voltage read 1.3 mV for the start CFDD and -6.6 mV for the stop CFDD.

Voltage/Energy discrimination window Besides the pivotal function of allowing only the signals of interest to carry on along the electronic chain, the definition of the upper and lower threshold values of the CFDDs discriminating windows also plays an extremely important role in the value observed for the system's time resolution. Hence, the correct definition of these voltage limits, which should seek for the best possible time resolution whilst still allowing the intended signals to pass through, is vital for the operation of the spectrometer. Like before, a new definition of the voltage discriminating windows was needed and performed any time the spectrometer suffered a modification or adjustment prior to or concerning the CFDDs, such as when the detectors' distance to the source+sample sandwich or the PMTs' operating voltage were altered.

Two types of voltage (or by extension energy) windows were required to be defined for each CFDD for two different situations. The first type of voltage discrimination concerned the determination of the system's optimal time resolution. For that, the discriminating windows of the start and stop CFDDs were, respectively, adjusted to accept the signals corresponding to the 1173 keV γ-rays and the 1332 keV γ-rays, from the decay of the ^{60}Co source. The second type of voltage discrimination was needed for the remaining measurements, involving the study of materials, as well as for assessing the real time resolution that could be achieved in practice during these experiments. With this intent, the start CFDD's window was set to collect the 1274 keV gamma-rays emitted practically simultaneously with the positrons resulting from the decay of the ^{22}Na source, while the stop CFFD's window was adjusted for the detection of the 511 keV photons originated from the positron annihilations happening in the material under study.

There was a need to distinguish between an optimal and a real time resolution, because in a gamma-gamma coincidence measurement, as is the case of a PALS measurement, the timing resolution of the system has a linear dependency with the energies of the processed γ-ray, E_{γ_1} and E_{γ_1}, according to [93]:

$$Timing\ resolution \propto \left(\frac{1}{E_{\gamma 1}} + \frac{1}{E_{\gamma 2}}\right)^{\frac{1}{2}} \tag{4.2}$$

Hence, the observed system's time resolution varied depending on the range of accepted energies in

the CFDDs and consequently on which type of voltage discriminating windows was established for a particular measurement. Both optimal and real time resolution values were assessed by using the ^{60}Co source. However, when the discriminating CFDDs' windows were adjusted for the detection of the ^{60}Co source's own gamma emissions, given the above relation and because the accepted γ-rays energies were higher, namely 1173 keV and 1332 keV, the registered time resolution of the system was lower, therefore better. As a result, the time resolution measured in these conditions corresponded to the minimum, as in optimal, time resolution that could be achieved with this spectrometer. This quantity was merely used to quantify the quality of the system and to establish the point after which the system could no longer be optimised. On the other hand, when the voltage discriminating windows were tuned for the ^{22}Na source's emissions, the accepted energies were lower since this time the 1274 keV and 511 keV γ-rays were considered. Consequently, the observed time resolution was higher, *i.e.* worse, corresponding to the real time resolution that in practice the spectrometer is able to exhibit in a typical PALS lifetime measurement. For that reason, it was vital to know its value as a means to explain why the results observed were better or worse than expected. This second type of voltage window was then used for two purposes: for the estimation of the real time resolution, with the ^{60}Co source and also for all further material study experiments, performed with the ^{22}Na source. The remaining of the chapter will address both the optimal and real time resolutions and when only the term time resolution is used it refers to both values.

For the purpose of accurately and precisely defining the voltage thresholds of both types of voltage windows discussed, the sources were positioned in the spectrometer and the energy spectra collected with each CFDD were analysed. This was achieved by feeding the CF MON output of each CFDD into the ADC's input, not before forcing it through an amplifier module where the bipolar signal, apart from being amplified, was also inverted so that its first fraction became positive and thus would be accepted by the ADC. The resulting energy histogram was then displayed in the computer monitor, where the energy spectra visualised for the ^{60}Co and the ^{22}Na sources resembled the ones depicted in *Figures 4.4* and *3.4*, respectively.

In order to observe the effect of the energy cut by the discriminating windows and therefore perceive which signals were being accepted or denied in the CFDDs, their Timing output was fed into the ADC's Gate input. However, before it had to be passed through a Gate & Delay Generator, where it was inverted as it needed to be positive to be accepted by the ADC and where its width was extended until it completely enveloped the positive fraction of the CF MON signal coming from the amplifier's output. Given that the Timing outputs are emitted solely when the input signals fall within the established voltage window, by using the former as the gate input for the ADC, only the accepted energy range is visualised in the energy spectrum. Then, the voltage thresholds of each CFDD are manually adjusted in their respective front panel buttons while the energy spectrum is examined and the windows are successively opened or closed until only the desired energy range is presented.

For the case where the discriminating windows were expected to accept the gamma emissions from the ^{60}Co source, the start CFDD's voltage thresholds were adjusted until the acquired energy spectrum displayed exclusively the photopeak corresponding to the 1173 keV γ-ray, represented by the number 1

in *Figure 4.4*. Meanwhile, the voltage limits of the stop CFDD were tuned until only the photopeak corresponding to the 1332 keV γ photon, represented by number 2 in the same figure, was present. For the other case, where the decay of the ^{22}Na source is considered instead, the start CFDD was regulated to guarantee that only the photopeak corresponding to the 1274 keV γ-ray, represented by the number 2 in *Figure 3.4*, was exhibited, whereas the stop CFDD was adjusted so that the annihilation peak, represented by number 1 in the same figure, was isolated in the spectrum. Having said that, it is important to remember however that, even though it grants better time resolution values, having very closed energy windows would result in that only very few signals are accepted and get to be accounted for in the final spectrum. This greatly impairs the counting rate and consequently the celerity of the overall PALS experiment. Thence, care was taken when defining the windows, making sure to include a slightly wider energy range without, of course, stepping out of the realm of the peak of interest, as a way to achieve a proper balance between time resolution and counting rate.

In order to define the final values for the discriminating windows for the first type of voltage discrimination, an effort was made to produce the best ideal time resolution for the system. This was achieved by acquiring several ^{60}Co spectra and iteratively adjusting the voltage windows according to whether the time resolution had improved or not, when compared to previous measurements. Similarly, in an attempt to provide not only the best possible real time resolution, but also the best possible positron lifetime values, the final thresholds for the CFDDs windows for the second type of voltage discrimination were defined by iteratively tuning them according to the level of agreement between the positron lifetimes obtained from the analysis of each consecutive spectrum collected with multiple reference samples and the values reported in literature, whilst still trying to maintain a good real time resolution. The final values for the discriminating windows of the start and stop CFDDs, for both types of voltage discrimination, are expressed in *Table 4.1*.

	1^{st} type of voltage discrimination		2^{nd} type of voltage discrimination	
	Start detector	Stop detector	Start detector	Stop detector
Upper threshold (mV)	5.00	3.10	2.44	0.97
Lower threshold (mV)	2.60	2.49	2.02	0.53

Table 4.1: Final voltage thresholds for the discriminating windows of the start and stop CFDDs for both types of voltage discrimination.

Constant Fraction delay cable The constant fraction circuit in the CFDDs is not complete without an external delay cable joining the two delay connectors in the front panel of the modules as this cable is critical for the shaping of the bipolar signal that will serve to mark the exact arrival time of the input pulses. Despite informing us of what type of cable should be used for this purpose, viz a RG58 cable, the CFDD's operating manual [94] does not state the supposed cable's length. Instead, and given that this factor strongly influences the time resolution of the system, selecting the ideal length requires a bit of experimentation as the length that provides the best timing performance heavily depends on the characteristics of the detectors and PMTs used in each case. Regardless, the user is not left completely in the dark since the manual presents an empirical formula with which to compute an initial estimate of

the suitable cable's length as we are told that the delay provided by the cable, t_{cable}, should be equal to:

$$t_{cable} = 1.1t_{rise} - 0.7ns \tag{4.3}$$

where t_{rise} is the rise time of the output pulse of the associated PMT, whilst the 0.7 ns term refers to the delay already imposed internally by the circuitry within the CFDD module. Seeing as these cables have a signal propagation velocity of 0.66 that of the speed of light c, the ideal cable length, l_{cable}, is estimated according to:

$$l_{cable} = (1.1t_{rise} - 0.7ns) \cdot 0.66c \tag{4.4}$$

Given the PMTs' rise times previously measured, our initial estimates for the delay cables' length were 55.84 cm and 62.37 cm, for the start and stop CFDDs, respectively. Nonetheless, this is only a starting point and so a more in-depth study ensued. For this study, the setup was arranged for the determination of the system's optimal resolution and all experimental setup conditions were kept constant apart from the cables applied to the delay connectors of both CFDDs. A set of cables of different lengths was successively tested and in each iteration the optimal time resolution was determined and later compared with the previous results. We began our trials with two identical cables on each CFDD, with a larger than estimated length of 96.3 cm, which was followed by a second trial with two cables both 49.8 cm long, a length relatively close to the predicted ones. The two tests resulted in ^{60}Co time spectra composed of an asymmetric peak, with which a proper determination of the optimal resolution was clearly not achievable. The study was then continued, this time with shorter cables and the results obtained for the optimal time resolution for each examined cable length are present in *Table 4.2*, where in the "Cables length (cm)" column, the values exhibited correspond to the length of the cable used for the start and stop CFDD, respectively. It is important to note that for each trial an energy spectrum was acquired with each CFDD, in order to ensure that, in each case, the cable change did not interfere with the current energy range defined and consequently with the peak detected.

Cables length (cm)	Optimal time resolution (ps)
12.0 and 12.0	163.77
25.6 and 27.7	163.29
30.2 and 30.2	164.39
31.1 and 31.9	165.39

Table 4.2: Optimal time resolution results for the optimisation test for the ideal constant fraction delay cable length of the start and stop CFDDs, respectively.

The results demonstrate that even though, in the range of lengths investigated, the optimal time resolution did not vary greatly, out of all, the 25.6 and 27.7 cm long cables provided the best optimal time resolution, followed by the 12.0 cm long ones. However, neither of these was employed in the setup because a set of two identical cables was preferred as, in case it was needed in the future, they were easier to be replaced and because the 12.0 cm long cables were too short and were under a great amount of stress when connecting the CFDDs delay connectors, which could deteriorate not only the cables but also the signal being processed. Thus, in the end we went with our third best but still close to finest option

and adopted the 30.2 cm long cables into our spectrometer.

Delay unit

As it has been mentioned, a certain delay is necessary to be imposed on the start and stop signals coming from the CFDDs, in order to give time, a few ns, for the FC unit to process the input pulses and generate an output gate one necessary for the operation of the TAC. Nevertheless, the delay imposed on the output pulses generated by the CFDDs must not be the same for both as the stop pulse must be retarded in relation to the start one, in order to enlarge the time interval that separates them. This is so for two reasons. Firstly, the TAC has a start-to-stop minimum conversion time of 5 ns which, in practice, means that for a valid time conversion to take place the stop signal must arrive at least 5 ns after the start one. This can only be guaranteed by forcing at least a 5 ns interval amidst pulses as most events would have far shorter lifetime spans. The other reason for this requirement concerns the impact on the lifetime histogram. The time difference between the arrival time of the start and stop signals dictates the bin in which that particular event is registered. Some events may have a very short time span between the incoming pulses and therefore, without any halting difference imposed on the pulses, they would belong to one of the very first channels in the histogram and it would be in these initial channels that the lifetime spectrum would begin to take form. Even so, it is so much more convenient to have the spectrum start further along the time axis to facilitate its subsequent analysis and to avoid the noise usually present at the beginning of the histogram to get mixed up with actual pivotal lifetime information, something which is easily achieved by forcing a suitable disparity between the delays imposed to the start and stop pulses.

At the beginning of our work, the time delays were controlled by two passive delay boxes with multiple time choices. However, it was soon realised that these units might be another source contributing to any imperfections in the system that may manifest in the observed zero channel shift and a poorer time resolution. Consequently, and given that we wanted the delay for the start and stop pulses to be fixed throughout our work, the units became redundant and were substituted by a pair of RG58 cables connecting the CFDDs outputs and the TAC's inputs. Since the start signal was meant to be stalled for 64 ns and for the stop signal a 96 ns delay was desired and since the propagation velocity in these cables is 1.98×10^8 m/s, the units were replaced by a 12.7 m long and a 19.0 m long cable, respectively.

Fast Coincidence Unit

The only important parameter to be defined in the FC unit concerns the width of its output signal that is expected at the start input gate of the TAC to validate the start pulse. This signal must last long enough to ensure that both the start and stop pulses arrive at the TAC's inputs for the time conversion process to be completed, seeing that the start pulse is required to be valid until the arrival of the stop, for which a gate signal is not necessary in order to be deemed valid as a true coincidence event has already been confirmed. The width of the FC unit output is controlled by a front panel WIDTH rotary switch and in our case was set for 85 ns, as read in the oscilloscope.

Time-to-Amplitude Converter

The most vital aspect concerning the TAC calibration is the time range, which consists of the max-

imum time interval between the arrival of the start and the stop signals at its inputs that is accepted by the TAC for time conversion. This quantity is set by selecting both one of the available time interval possibilities in the RANGE rotary switch, namely 50, 100 or 200 ns and the multiplying factor of this range from the 1, 10, 100, 1k and 10k options in the MULTIPLIER switch. In our case, a time interval of 50 ns range was selected as events with longer lifetime periods were not expected to arise from the study of neither our reference or polymeric samples.

With the oscilloscope, we quantified the real signals' arrival time at the TAC to make sure everything added up. We verified that the time difference between the arrival of the gate signal from the FC unit and the start pulse from the CFDD was 16 ns, due to the lengthy operation of the FC unit, and that the time period separating the arrival of the start and stop pulses to the TAC was 25 ns, even though the nominal difference was 32 ns. Considering these measurements and the fact that the gate signal's width was 85 ns, the maximum acceptable time range at the TAC was of only 44 (85-16-25) ns, slightly less than the expected 50 ns but still more than enough to admit all the events to be observed in our case.

Analog-to-Digital Converter

Finally, the ADC was set for a 4096 conversion gain, which corresponds to 4096 channels in the MCA histogram as it was determined that it would be sufficient to properly detect and separate the lifetimes we expected to observe. Furthermore, the ADC's upper and lower level discriminators were, respectively defined as 100% and 2% of the defined full scale, so that all signals, but the ones originating from noise, would be considered.

All the working parameters of each component of the experimental setup that were defined during the calibration process, together with their final established value are summarised in *Table 4.3*.

Component	Defined parameter	Value
PMTs	Operating voltage	-1865 V and -1901 V, for the start and stop, respectively
CFDDs	Blocking Width	1 μs
	WALK potentiometer's voltage	1.3 mV and -6.6 mV, for the start and stop, respectively
	Discriminating window's voltage	Adjusted to accept 1274 and 511 keV γ-rays, for the start and stop, respectively
	Constant Fraction delay cable length	30.2 cm, for both the start and stop
Delay units	Length of the RG58 cable that substituted the delay module	12.7 m and 19.0 m, for the start and stop, respectively
FC Unit	Width of the output signal	85 ns
TAC	Accepted time range	50 ns
ADC	Conversion gain	4096
	Upper and lower level discriminators	100% and 2% of the defined full scale, respectively

Table 4.3: Summary of the parameters defined for each electronic module during the calibration process.

4.1.3 Tests to improve the experimental setup performance

Furthermore, a lengthy set of tests and studies were conducted on the performance of the experimental setup in an attempt to find the operating conditions that resulted in not only the absolute best possible

time resolution, without compromising a satisfactory counting rate, but also on a great agreement between the positron lifetime results obtained from the measurements with our reference samples and the values reported in literature.

Ideal detection configuration

A first test, suggested in [95, 96], that could be performed in a PALS experimental setup in an effort to improve the spectrometer's time resolution consists of swapping the role of the detectors and associated PMTs. In other words, the detector and PMT that were originally connected to the CFDD responsible for the detection of the start signal would instead be connected to the other CFDD dealing with the stop signal and vice-versa. Since the PMTs have different rise times, by interchanging their role, it could happen that a more suitable match between the PMTs and respective CFDDs operating times was achieved, resulting in an overall improved time resolution.

In that sense, the set of detector and associated PMT with the lowest rise time, which was originally generating the start signal processing chain was now swapped with the originally stop signal associated detector+PMT set, which presented the highest rise time. In this new configuration, the system's optimal time resolution was measured with the CFDDs' discriminating windows readjusted to ensure that the intended energy ranges were observed, with an equally readjusted WALK potentiometer and with 30.2 cm long CF delay cables, while the PMTs' operating voltages were kept the same as in the initial configuration. This new layout exacerbated the optimal resolution as the registered value was of 165.79 ps, as opposed to the earlier 164.39 ps. Even though there was only a slight difference, the resolution did indeed got worse, so it was decided to maintain the original setup's configuration.

Ideal counting rate and number of counts in a lifetime spectrum

After reaching a satisfying time resolution of the spectrometer, our focus shifted for attaining equally satisfactory results for the positron lifetimes of the reference samples, for the purpose of certifying our spectrometer as suitable for use in any PALS experiment. At the same time, we were interested in improving the quickness of the spectra acquisition process in order to collect more lifetime spectra in a reasonable time period. In that sense, a new series of tests was carried out aiming at discovering the maximum detector/PMT count rate and fewest number of registered counts in a lifetime spectrum that, when combined in a measurement, resulted in lifetime spectra containing the optimal positron lifetimes for the reference samples.

This new set of tests commenced with the collection of spectra with only the ^{22}Na radioactive source positioned at the sample holder, with all setup's parameters working with their ideal specifications, previously defined. The ^{22}Na source was chosen for the first stage of the experiment given that the analysis of the spectra acquired and subsequent result comparison are far simpler as only one main lifetime component is usually expected in a source's lifetime histogram. This is the so called source correction component, associated with the positron annihilations within the Kapton® HN foils encapsulating the source and within the ^{22}Na source itself. Only one lifetime component is commonly reported for Kapton® HN, although at rare times two components can be resolved, making this polymer rather fitting to be used for the source encapsulation, since it adds no further complexity to the lifetime spectrum. An extensive

compilation of these published values, alongside their respective relative intensity in the spectrum, is presented in *Table B.4* featured in *Appendix B*. The relative intensity is absent in most references, although when only a single lifetime component is displayed it usually means that it is the dominant one, with a relative intensity close to 100%. In our case, simply a sole lifetime component with a value close to 381.34 ps is expected for Kapton® HN, corresponding to the average amount computed taking into consideration solely the data shown for a single positron lifetime. On the other hand, although the references reporting results for the positron lifetimes in the $^{22}NaCl$ crystallites tend to agree that only one lifetime component is detected, they definitely can not reach a consensus concerning its value, as a variety of figures have been published, ranging from around 330 ps to about 430 ps, as it can be verified by the compilation in *Table B.5*, featured in *Appendix B*. Furthermore, whether it is 330 ps or 430 ps or some amount in between, the positron lifetime in $^{22}NaCl$ is very close and almost coincident with the single lifetime considered for Kapton® HN. Therefore, and because the length traversed by positrons in the Kapton® HN foils is much larger than the one travelled in the $^{22}NaCl$ crystallites, the effect of the annihilations in the latter are hardly detectable and separated from the main component associated with Kapton® HN in the ^{22}Na source's lifetime spectrum and thus only a sole component of approximately 381.34 ps is expected in our source's spectra.

To carry out these tests, the setup's configuration was kept constant throughout, with the exception of the scintillators' distance from the sample holder at the centre, which is directly correlated to their count rate. Four different situations were tested, that corresponded to positioning the detectors equally distanced 1, 3, 4 and 5 cm away from the sample holder. However, since the detectors and associated PMTs have different operating characteristics, it is expected that, for the same length separating them from the centre, they present slightly different count rates. This was true for our case where the count rates for the start and stop scintillators were respectively of about 37k counts/s and 35k counts/s, 17k counts/s and 16k counts/s, 11k counts/s and 12k counts/s and 9k counts/s and 9.5k counts/s, for the four tested distances, respectively. In order to compute these count rates, the output of each PMT was forced through an amplifier module, where the signal was inverted and later led to the ADC's input and subsequently to the MCA. Here, an energy histogram was accumulated for a certain amount of time, after which the registered events in all channels apart from the first ones, which are heavily influenced by noise, were added up and the found quantity was divided by the collection time, resulting in an estimate for the count rate. Despite corresponding to an even better count rate, the scenario where the detectors were in close contact with the source+samples sandwich was not considered as it was observed that, in this case, anomalous peaks appeared in the lifetime spectrum.

At the same time, for each examined distance, several spectra were acquired for small periods of time, with the help of the developed script for the MAESTRO software, discussed in *Section 4.2.1*, and different amounts of these histograms were added up, with the aid of the Mathematica program written for this purpose, described in *Section 4.2.2*. The idea was, apart from testing the system's stability and the zero channel drift, to obtain in the end a set of histograms, each corresponding to the sum of a different number of smaller spectra and thus having a different number of recorded counts, ranging from tens of thousands to tens of millions, in order to thoroughly investigate the dependence of the reference samples'

positron lifetimes with the number of counts in the respective spectrum. The resulting histograms were then analysed with the PALSfit3 software, where, for each inspected distance, the resolution was determined, in the ResolutionFit module, with the spectra containing the most counts. Additionally, in the PositronFit module, the histograms were examined assuming two lifetime components would be present, one corresponding to positron annihilations in Kapton® HN and the other one corresponding to unwanted annihilations in the surrounding materials or in air.

From the results obtained, it was observed that, for every distance scenario, the Kapton® HN positron lifetimes attained from the analysis of spectra containing 1 or more million counts were practically the same, while for the ones with fewer counts the values somewhat varied from one case to the other. Furthermore, the reduced χ^2 was better for histograms having approximately 1 million counts, which meant that 1 million was the fewest number of counts that a spectrum had to contain in order to produce stable and reliable positron lifetime values. However, for any tested distance, and despite the number of counts in the spectrum, the obtained Kapton® HN positron lifetime values were far from expected, which prevented any conclusion to be drawn regarding the distance that provided the best positron lifetime results. This is due to the small thickness of the Kapton® HN foils, which was not sufficient for stopping all positrons emitted, resulting in a fairly intense lifetime component associated with annihilations in air and inside the detectors, which corrupted the lifetime results for the Kapton® HN itself.

Hence, the tests proceeded with the as-received metallic reference samples, in an attempt to identify the count rate that produced the best possible results for Cu and Ni. For this purpose, with the same exact setup configuration and calibration, one spectrum, containing approximately 1 million counts, was acquired for each sample, for two distinct lengths separating the detectors and the centre of the detection assembly, namely 1 cm and 3 cm. Tests for distances of 4 and 5 cm were dismissed as acquiring a 1 million count spectrum at the associated count rates simply took up too much time. The collected spectra were again examined with the PALSfit3 software, where the resolution was deduced from the nickel spectrum acquired for each distance, since nickel exhibits the shortest positron lifetime out of the two reference samples. With this information, the histograms were then decomposed into three different lifetime components, which, from shortest to longest, were respectively associated with annihilations in the bulk of the sample, the Kapton® HN foils and the surrounding media. The results achieved from the analysis of the as-received Ni and Cu samples, for both distances tested, are displayed in *Table 4.4*.

	Ni			Cu		
	Shortest lifetime (ps)	2^{nd} shortest lifetime (ps)	Reduced χ^2	Shortest lifetime (ps)	2^{nd} shortest lifetime (ps)	Reduced χ^2
Detectors 1 cm away	139.0 ± 1.0	328.8 ± 3.5	1.014	145.1 ± 2.0	330.7 ± 7.3	1.062
Detectors 3 cm away	147.4 ± 1.9	369.2 ± 8.0	1.159	146.6 ± 2.4	334.7 ± 8.0	1.050

Table 4.4: Results obtained the analysis of spectra acquired with the as-received Ni and Cu samples for the detectors 1 cm and 3 cm away from the sample holder.

A closer look at the table shows that, for both samples, the shortest lifetime values were more similar to the respectively desired 106.96 ps and 116.19 ps with the configuration where the detectors are 1 cm away from the centre, even though values close to these ideal ones were not attainable as the samples used were the non-annealed ones. Additionally, for the Kapton® HN's lifetime component it is clear that the values found are somewhat closer to the expected ones for the opposite layout. However, this was not the focus of our efforts as, in fact, this value would not be utilised to render or not the spectrometer as adequate for future PALS measurements. In contrast, the reduced χ^2 seemed to be always either relatively the same or even better for the case where the scintillators are closer to the sample holder. Therefore, since the results appeared to be more accurate with the detectors positioned 1 cm away from the samples and since this arrangement also allowed a faster acquisition of the spectra, it was decided that all further lifetime spectra would be collected with this configuration.

Ideal number of channels in the MCA

One final aspect that could influence the results observed for the metallic and semiconductor reference samples was the established number of channels in the MCA. If the channels were extended from 4096 to 8192, this would result in a far more fine time calibration as the accepted time range would remain the same but now would spread across double the channels. Then, since these samples were expected to exhibit very short positron lifetimes, it was pondered the hypothesis that if the MCA exhibited 8192 channels instead that not only but especially these very short lifetimes would be far better resolved and therefore closer to the reported values.

Then, using the typical setup configuration but with the number of channels in the MCA set for 8192, with both detectors positioned 1 cm away from the sample holder, a spectrum was acquired with the as-received Ni samples, chosen given their lowest expected positron lifetimes. Furthermore, both this spectrum and the one attained in the same conditions, with the same sample and with the detectors positioned 1 cm away from the centre, but with only 4096 channels in the MCA were analysed and the results for their shortest lifetime component derived from positron annihilations in the bulk of the sample, summarised in *Table 4.5*, were compared.

	Spectrum with 4096 channels	Spectrum with 8192 channels
Shortest positron lifetime (ps)	140.0 ± 1.7	139.0 ± 1.0
Reduced χ^2	1.081	1.014

Table 4.5: Results from the analysis of spectra acquired with the as-received Ni samples and detectors 1 cm away from the sample holder, for both cases of 4096 and 8192 channels in the MCA.

It can be concluded that doubling the number of channels in the histogram did not improve neither the results observed for the as-received Ni samples or their quality, as the positron lifetimes were essentially the same within the margin of error as were the values for the reduced χ^2. Thence, and taking into account that, with an histogram with twice as many channels, it takes, in theory, double the time to achieve an equally suitable bin statistic, it was decided to proceed the remaining PALS measurements with just 4096 channels in the histogram.

4.1.4 Conclusions of the calibration procedure and tests

The many calibrations and alterations performed on the experimental setup led to a final optimised acquisition system with a reduced zero channel drift and an improved time resolution.

In fact, thanks to both a reassembly of the whole setup, accompanied by a substitution of some faulty connecting cables, and to a change in the way in which the delay of the signals coming from the CFDDs was executed, by forcing them through cables of appropriate length instead, the zero channel drift apparent in our spectra was diminished. Indeed, it changed from a shift of dozens of channels in a short period of time to a barely noticeable shift of only a few channels in long acquisition periods. Nevertheless, this shift still had an impact on the quality of the spectra acquired and thus its effects needed to be accounted for and possibly totally eliminated in the analysis process, to prevent us from obtaining inaccurate values for either the positrons' lifetime or the system's time resolution.

On the other hand, the many adjustments carried out on the various components of the system, but in particular on the CFDDs, allowed the reduction of the time resolution to very satisfactory values. To prove this, at the end of all modifications, two spectra were acquired with the ^{60}Co source, for the determination of the final optimal and real time resolutions. These were then fitted to both a Gaussian function and an ESG function, with two developed C++ codes, explored in *Section 4.2.3*, in order to extract the corresponding FWHM value that is generally used to characterise any time resolution curve. For both curves, the ESG function produced much more adequate fits, which was not only visible, but was also attested by better values for the reduced χ^2, respectively of 1.192 and 0.998, for the final optimal and real time resolutions. The resulting graphs showing the data acquired for the determination of the ideal and real time resolutions, alongside the ESG fitted function are presented in *Figures 4.7(a) and 4.7(b)*, respectively.

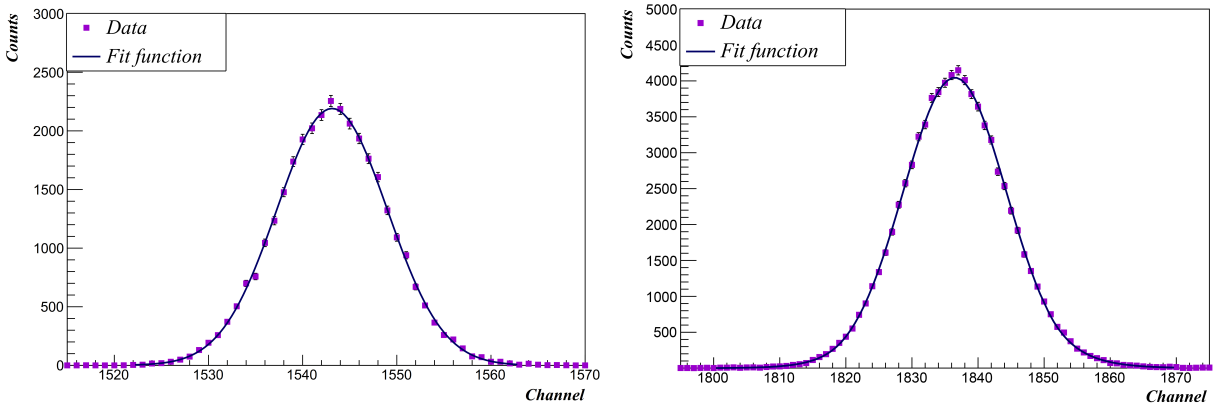

(a) Ideal time resolution curve

(b) Real time resolution curve

Figure 4.7: Data obtained for the determination of the system's ideal and real time resolution functions and respective fitted ESG function.

The resultant FWHM values of the peaks were, respectively, of 164.39 ps, a more than satisfactory result, and 219.05 ps, equally admirable, in total accordance with the typical values attained with a PALS spectrometer, ranging from 180 to 250 ps.

Finally, and most importantly, all the optimisation work culminated in a system capable of collecting

spectra that produce excellent results for the positron lifetimes of the reference samples, in agreement with the values reported in literature. These results will be presented in *Chapter 5*.

4.2 Routines for spectra acquisition and analysis

Following the additions, alterations and improvements performed to our actual experimental setup, a second stage ensues in order to enhance the overall research to be undertaken with our PALS spectrometer. This concerns the attainment of a deep familiarity with the PALS experiment analysis methods and their intricacies, something that was gained through the acquisition and careful analysis of multiple reference material spectra. From that experience, it became apparent that there was a dire need for a set of analysis tools to back up a few procedures of the PALS technique.

In that sense, four routines were created with the intent to enable or ease certain features of the data acquisition and analysis processes and thus allowing comprehensive and insightful future PALS measurements to be carried out.

4.2.1 Acquisition of multiple spectra in one data acquisition run

The first need pointed out concerned the acquirement of the lifetime spectra without the influence of the observed zero channel drift because without eliminating this effect there is no room for an accurate analysis of the results. One way to minimise this is to, rather than attaining the whole histogram in one run, instead running the acquisition in the same conditions but for shorter periods of time and afterwards add all the resulting spectra with fewer counts, after accounting for the zero channel drift and applying a proper correction. This will result in a final spectrum with the same number of counts as in the first case, but now with a more defined peak as the broadening effect disappears. The first step of this procedure is then the consecutive acquisition of spectra for shorter lengths of time. This can be achieved by manually starting and stopping the data collecting process in the MCA. However, one of the many often mentioned advantages of the PALS technique is the ability of the experimental setup to operate unattended, which eases and accelerates the overall study of a sample. Therefore, a manual start and stop of the acquisition process defeats the purpose.

In order to overcome this, a JOB file, whose script is presented in *Figure C.2*, in *Appendix C*, was written for the spectrometer's acquisition software MAESTRO with instructions for the successive collection of many spectra without the user's assistance. A MAESTRO's JOB file is started at the beginning of an acquisition run and consists of an ASCII text detailing a series of commands to be performed by the spectrometer, that when put in action automates most of its functions. In our case, the file orders the spectrometer to acquire n spectra, with n stipulated by the user, each for a period of time of t seconds, t also specified by the user, and then save them in a folder, whose name is yet again defined by the user, with different designations to facilitate the subsequent file manipulation.

4.2.2 Sum of many spectra after zero channel drift correction

After acquiring the many smaller spectra, the next step in obtaining a more defined final spectrum without any influence from the zero channel drift is to properly add all of these, meaning that the fact

that each spectrum exhibits its own zero channel, that may differ from some of the other histograms, must be accounted for when summing. If not, then the result of the sum would be the same as if only one final larger spectrum was acquired, *i.e.* a spectrum with a broadened peak, whose analysis could possibly lead to incorrectly fitted values. Therefore, firstly, the zero channel of each spectra must be identified and one of these is chosen as the final spectrum's zero channel, after which the remaining histograms are shifted by a number of channels corresponding to the remainder between their own zero channel and the selected one. Finally, the counts of all the bins of all the shifted spectra are added in their corresponding bin and a final histogram with the intended number of counts and a well-defined peak is obtained.

For this purpose, a Mathematica [97] routine, whose script is presented in *Figure C.1*, in *Appendix C*, was created that accepts an unlimited number of files of the type outputted by the MAESTRO software. The routine then goes on to search for the zero channel of each spectra, after which it determines the lowest zero channel number out of all the ones identified and subsequently shifts all the histograms, according to the mechanism described above. Finally, the Mathematica script checks if the spectra have been adequately summed by searching for the total number of counts and the zero channel of the final spectrum and if everything is according to the expected, the routine exports the final product in the only format accepted by the PALSfit3 software, in preparation for further analysis.

Only one issue may arise, which is the loss of information resultant from the fact that some channels of the shifted histograms are not taken into account. However, given that the lowest zero channel is picked as the final spectrum's zero channel, which means that all spectra are shifted left, and given that the zero channel from a particular histogram does not usually differ greatly from the others, there is no real loss of information in the process as the bins at the left far end of any spectrum simply contain either noise or negligible counts.

4.2.3 Fitting of the spectrometer's time resolution curve

As it became clear, for many stages of the optimisation process of the PALS spectrometer, it is vital to know the exact description of the system's time resolution. In order to attain a definition of this curve, in particular of its FWHM value, either a sum of multiple (although one is typically enough) gaussian functions or an ESG function is fitted to a spectrum acquired with the ^{60}Co source.

In that sense, a C++ routine, containing functions from the ROOT library [98], whose script is presented in *Figure C.3*, in *Appendix C*, was written for the fitting of a user provided ^{60}Co spectrum to one gaussian function over a user defined range, providing, apart from the reduced χ^2 value, the estimated values for the peak's height, the mean value and the standard deviation, with which the FWHM value can be computed. In addition, another C++ routine, with functions from the ROOT library, whose script is presented in *Figure C.4*, in *Appendix C*, was also developed for the fitting of the curve to an ESG function instead, in a range equally established by the user, that outputs not only the values for all the curve's parameters, but also the reduced χ^2.

Additionally, the user is required by both routines to provide an educated guess of the expected values for the function's parameters, which will be used as initial figures for the fitting. A good guess of the parameters is determinant not only for its quickness but also for the ability of the fitting process to

converge to the accurate values.

4.2.4 Determination of a material's free volumes' size

Finally, when polymeric samples are already being analysed, it should be kept in mind that, at the end of the examination of such samples by the PALS technique, an aspect concerning its free volume structure is often desired, viz the size of the pores found inside the samples.

The size of the free volumes inside a sample under study can be assessed by applying individually and "by hand" each of the existent formulas discussed in *Section 2.3* to the positrons' lifetime values found by the fitting of the experimental spectra. The choice of model, and respective formula, to be employed in each case relies upon the obtained lifetime value as each model is only valid in a certain, and at times tight, o-Ps lifetime range. However, an attempt was undertaken to make this process a lot more straightforward, by developing a Mathematica routine, whose script is presented in *Figure C.5*, in *Appendix C*, which accepts o-Ps lifetime values from the user and simultaneously employs all these equations to calculate the free volume's size. The final results are presented only for the models whose validity range includes the considered o-Ps lifetime, as both the pores' radius or square side, for the valid models that consider them to have a spherical or cubic geometry, respectively and also as the pores' mean free path for all the valid models, for an easier comparison between the obtained results.

Chapter 5

Data analysis and experimental results

The remainder of this work comprised the collection of spectra of all the reference samples, which was meant to demonstrate the impact that the optimisation process had on the quality of the spectrometer, with regards to its capability of producing reliable lifetime spectra that reproduced the expected results found in literature. Furthermore, the now optimised spectrometer was also employed in the collection of lifetime spectra with the set of GREI's polymeric materials, mentioned in *Section 3.5.3*, which were then fitted and the resulting values were used to compute the size of the free volumes inside the polymeric samples, which would later be used to attest their quality and suitableness for the intended purposes.

5.1 Spectra analysis procedure

Before the final results are presented, a remark must be made related to the spectra analysis procedure which, unlike the acquisition process, has not yet been properly and thoroughly discussed. The analysis of the various histograms acquired during the optimisation process, aside from being essential to assess the impact of the many steps undertaken during this task, also served to learn how to use the software PALSfit3 and get acquainted with the several aspects involved in the analysis of a lifetime spectrum. When a lifetime spectrum is introduced into the analysis software, several parameters have to be defined, inserted or selected into the program, namely the system's time calibration; the mechanism for background subtraction; the zero channel of the spectrum; the fit range, *i.e.* the channel range that will be considered for the fitting process; the initial guesses for the lifetime values of the lifetime components; the description of the time resolution curve; and the lifetimes and respective relative intensities of the lifetime components related to annihilation in the source, the source contribution for short.

The first of these parameters, the time calibration, is simply entered in the program. In second place, for the background subtraction, a choice must be made between allowing the program to automatically calculate the mean value of the background by considering the full spectrum range, or delimiting that action to a desired channel interval or even setting the background contribution equal to an amount manually introduced. Similarly, the spectrum's zero channel is either fixed to the value introduced by the user or automatically determined by the software, taking a user inserted guess as the initial value for the conversion process. Additionally, the fit range, which comprises a start and stop channel that constrain the fitting process to the bin span in between, is always defined by the user according to his own analysis necessities. Finally, the lifetime values provided to the software as initial guesses to be used

in the convergence process are either the mean value of the lifetimes reported in literature for the case of reference samples or educated guesses of the expected results for the remaining ones.

Unlike all above parameters whose definition is rather straightforward, the definition and imposition on the software of the system's real time resolution and source contribution values are rather more challenging, due to the fact that a standard process, accepted by every researcher or in literature, for their determination has not yet been established in the PALS community. This would not present a problem if the final results were not heavily influenced by the choice of procedure to apply, however, this is not what is typically observed. In fact, in an interlaboratory study [99], involving 12 laboratories, the positron lifetime results obtained in each laboratory, where lifetime data was collected and evaluated following each laboratory's own standard acquisition and analysis procedures, were compared and an attempt was made to understand the origin of the variations observed. The study found that, for all samples and for all lifetime components, there was quite a considerable disparity between the results attained by each laboratory, for both the lifetimes and respective relative intensities. In order to justify such disparity, one of the causes appointed was the diversity of time resolution and source correction determination procedures, which were individually developed at each laboratory. Of course, some aspects related to the spectrometers' performance and the acquisition process, such as the count rate, the time calibration, the number of counts in each spectrum and the background counts, which were also freely determined by the each laboratory could not be ignored for their influence on the spectra acquired and consequently on the results obtained. That is why, on two other interlaboratory studies [100, 101], where the lifetime results obtained from 12 laboratories were also compared, this time the different laboratories were operating under the same agreed spectra acquisition protocol, while the procedure for source contribution description was still left to the decision of each participant. The discrepancies detected among the results attained by each laboratory, for both lifetimes and relative intensities, are far better than the ones reported in [99], most likely due to the regulated conditions for the lifetime spectra acquisition. Nevertheless, these are still observed and the influence of a non well defined mechanism for the definition of the source contribution can not be denied. Although differences in factors such as the spectrometer's tuning and calibration, the time resolution of the system and the count rate employed, to name a few, have a considerable influence on the disparity of values obtained from the analysis of a lifetime spectrum, making it impossible for different laboratories to ever achieve the same final results, these are considered to be optimised for each experimental setup. Hence, the choice of the analysis method, in particular concerning the determination of the time resolution and the source contribution, has a considerable weight on the outcome of the results. We have seen, from the examples of the most recent interlaboratory studies [100, 101], that there was a significant reduction of the disparities between results when all laboratories involved carried out the acquisition of their spectra according to the agreed protocol. So an even bigger agreement could certainly be reached if a guideline for the analysis process was established. Therefore, it is vital for the success of the PALS technique and the work of each researcher that a consensus is reached for a standardised method for the definition of these two factors as until now a lack thereof has led to a difficulty in ensuring the equivalency and reliability of data from different experiments. This has consequently also led, even if not exclusively, to a difficulty in the establishment of

new PALS spectrometers because a comparison between the results obtained and the data from literature, required for the optimisation process, might be misleading.

In an effort to decide the procedures for the determination of the time resolution function and the source contribution to be employed in our work, around 100 publications were consulted, in order to put together a comprehensive list of the many ways in which these determinations can be performed. The first thing that was noted is that in copious amounts of publications, the determination of either the time resolution function or the source contribution or both is not even mentioned and in others that do mention, the procedures carried out are often not thoroughly described. Even so, many different methods for the determination of the time resolution to be considered in the fitting process were detailed in literature. In fact, in [28, 31, 102–108] the time resolution function that was introduced in the analysis software for the fitting of spectra was assumed to be the one monitored with the ^{60}Co source, while in [109] a similar method was employed, but with a ^{207}Bi radioactive source instead. On the other hand, the spectrometer's time resolution curve can also be determined by extracting this information from the fitting results of a reference sample of well known positron lifetimes, as was performed in [30, 32, 36, 110–112], a process that can be facilitated by depositing the radioactive source directly onto the sample, as was decided in [86, 113], although other problems may arise. A distinct method consists of analysing all collected lifetime spectra in one go, which is possible in some analysis softwares, and extracting the resolution function from this fitting process, where it was considered as one of the fitting parameters and common for all spectra [15, 16, 114–117]. Finally, two different publications [118] and [119] have employed yet two other procedures, respectively, the systematic variation of the fixed value for the resolution in the fitting process, until the best χ^2 per DOF is reached and the extraction of this information from the results obtained from the analysis of a lifetime spectrum acquired solely with the ^{22}Na source and corresponding encapsulating foils.

Contrastingly, the definition of the source contribution is not as straightforward, as both the lifetime and the relative intensity of the corresponding lifetime component have to be determined. They can be determined simultaneously if both parameters are fitted with all collected spectra in one single data analysis run, with the lifetime considered the same for all spectra, but not the relative intensity, as was performed in [15, 16, 114, 116]. Another way is if they are considered as two additional parameters in the fitting process of any individual spectrum, a method employed in [105, 120, 121]. A final method involves considering them as fixed parameters in the fitting of a reference sample spectrum and systematically vary their values until a fitting variance minimum is found, as was the case for [110, 122–124]. Nonetheless, only the lifetime may be determined. This is generally done by considering it as one parameter in the fitting of a reference sample spectrum, like it was performed in [111, 113, 125, 126] or by extracting this quantity from the fitting of a ^{22}Na lifetime spectrum [119, 127]. Finally, in [118], it was the source contribution's relative intensity that was determined as the one for which the spectra χ^2 per DOF value was the best, while the lifetime was fixed as the mean value found in literature. The relative intensity of the source contribution depends on a multitude of factors, such as the source's activity, the thickness of the encapsulating foils and the characteristics of the material under study, such as its density, thickness and atomic number. This last property determines the backscatter of positrons at the interface between

the positron source and the sample and hence the multiple passing of positrons through the source. As a consequence, several empirical models have been designed to estimate the relative intensity of the source component in a lifetime spectrum as a function of the atomic number of the sample of interest, by carefully testing the agreement of their predictions with the experimentally obtained data [110, 124, 126, 128, 129]. These are then employed in some studies, of which [130, 131] are excellent examples, to compute the relative intensity of the source associated lifetime component.

5.2 PALS results for the reference samples

For the purpose of analysing our experimental collected lifetime spectra, the PALSfit3 software was used, where all the parameters and settings defined were the same throughout the evaluation of all spectra. The only exception is the initial values for the lifetimes and relative intensities of the lifetime components, which were established individually, at the beginning of the analysis of a new spectrum as they are sample dependent. The system's time calibration, computed in *Section 4.1.2*, was manually introduced in the program to allow for the counts *vs* channel histograms to be converted into spectra in the time realm, for the determination of the positron lifetimes. Furthermore, the background subtraction was defined to be automatically calculated by considering the full spectrum range, while the zero channel was equally determined automatically by the software and the required user specified initial guess corresponded to the bin containing the maximum number of counts, as that is the definition of zero channel. On the other hand, the start and stop channels of the fit range were stipulated as the zero channel and the last bin in the spectrum, respectively. The choice of the stop channel is pretty obvious, whereas for the start one a lot more thought was put into it as the selection of these parameters influenced the obtained lifetime values up to dozens of ps. In our case, the zero channel was selected not only because, for all spectra analysed, this was the choice that guaranteed the most reliable fits, with χ^2 values closer to 1, but also because this assured that all but only the channels containing information regarding the lifetime of positrons were considered, in order to avoid adding any more complexity to the fitting process.

Additionally, the time resolution of the system was extracted from the analysis of a reference sample spectrum, namely that of the annealed nickel samples. Nickel was preferred as it presents the shortest positron lifetime out of all the selected materials, therefore its corresponding spectrum was the simplest of all to be utilised for this purpose. The annealed samples were used because, unlike the as-received ones, their expected positron lifetime was known with a high degree of certainty. The spectrum was then analysed in the ResolutionFit module of the software, where three attempts were made to describe the resolution function as either a gaussian function or a sum of either 2 or 3 gaussian functions, each with an FWHM value whose initial guess had to be supplied by the user in an essential step to achieve convergence of the fitting process. While the initial values provided for the lower intensity curves were simply educated guesses, the number supplied for the most intense or unique gaussian function was the real time resolution found in *Section 4.1.4*, as this is indeed the time resolution with which all spectra were in fact acquired and so it is expected that the fitting software is capable of obtaining a value similar to this one. In the end, the best fit was achieved when only one gaussian function, with a FWHM of 212.5 ± 1.9 ps was considered, a value quite close to the 219.05 ps obtained for the real time resolution. Hence,

this was the time resolution description that was considered for the analysis of the remaining spectra, by being introduced and fixed in the Resolution section of the PositronFit module, that was used henceforth.

Finally, the source contribution was determined with the aid of the same annealed Ni sample spectrum, now analysed in the PositronFit module, where three lifetime components were considered, with one of them associated to annihilations in the radioactive source. The lifetime result obtained for this component was 364.9 ± 5.4 ps, which is considerably close to the expected 381.34 ps, corresponding to the average value computed for the positron lifetime in Kapton® HN, which was set as the initial guess for this component. The full description of the analysis process carried out with this spectrum is provided in *Section 5.2.1*. From this point onwards, an additional lifetime component accounting for annihilations in the positron source, with a fixed lifetime value of 364.9 ps, was added in the evaluation of the lifetime spectra. However, its relative intensity was kept a free parameter to be fitted, since the strength of the source contribution is different for every sample as it is heavily dependent on factors such as density and atomic number of the sample under study. These two mechanisms of time resolution and source contribution determination were chosen for our work not only because they were adaptable to our analysis conditions but also due to the fact that they were the most commonly applied methods, which signified a more reliable comparison with results reported in literature.

The parameters defined in the fitting software at the beginning of the analysis, along with the method employed for their definition and the value introduced for them in the program are compiled in *Table 5.1*.

Parameter	Definition process	Introduced value
Time calibration	Manually introduced in the software	11.722 ps/channel
Background subtraction	Automatically determined by the software by considering the full spectrum range	-
Zero channel	Automatically determined by the software, with a user provided initial guess	The initial guess corresponded to the bin containing the maximum number of counts
Start channel	Manually introduced in the software	The bin corresponding to the zero channel
Stop channel	Manually introduced in the software	Last bin in the spectrum
Time resolution	Extracted from the analysis of an annealed Ni reference sample spectrum	212.5 ± 1.9 ps
Source contribution	Extracted from the analysis of an annealed Ni reference sample spectrum in the PositronFit	364.9 ± 5.4 ps

Table 5.1: Determination method and defined value for the parameters defined in the fitting software at the beginning of the analysis process.

5.2.1 Metallic and semiconductor reference samples

As-received nickel and copper samples

After the determination and definition of all relevant analysis parameters and settings, the first properly evaluated lifetime spectra were the ones collected with the as-received nickel and copper samples. Each spectrum was resolved into three discrete lifetime components corresponding, from shortest to

longest, to: the free positron annihilations in the bulk of the sample, characterised by the lifetime τ_{bulk} and relative intensity I_{bulk}; the source contribution, described by the lifetime τ_{source} and relative intensity I_{source}; and the positron annihilations in the surrounding environment, such as neighbouring materials or the air layers between the samples and the source and between the source+sample sandwich and the detectors, defined by the lifetime τ_{env} and relative intensity I_{env}. Apart from τ_{source}, which was fixed to the established value of 364.9 ps, all the other parameters were freely determined by the software, with the initial lifetime value for the environment component set to an educated guess of the expected results and for the case of τ_{bulk} to the average value of the positron lifetimes in the samples, computed with results reported in literature, corresponding to 106.96 ps for nickel and to 116.19 ps for copper. The acquired lifetime spectra with their constituent lifetime components, accompanied by their respective residual plot are represented in *Figures 5.1* and *5.2*, for nickel and copper, respectively.

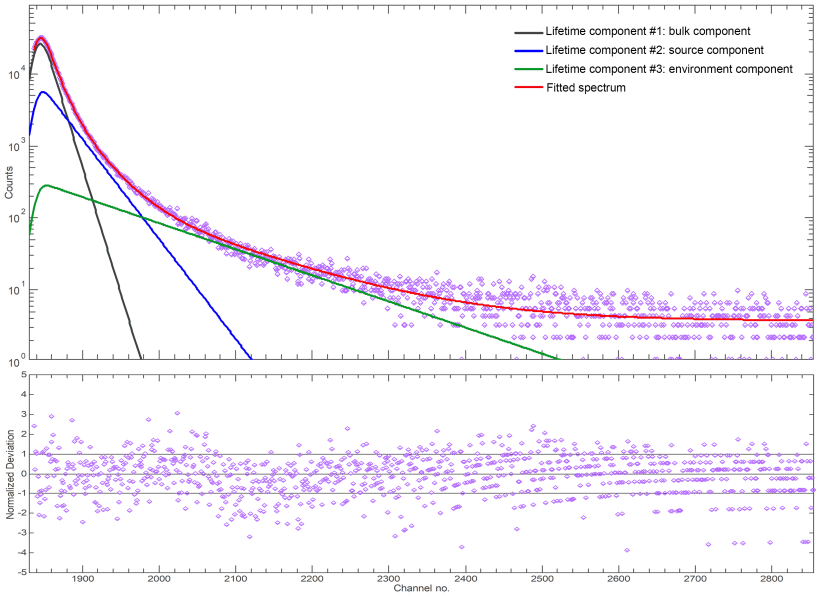

Figure 5.1: Experimental lifetime spectrum acquired with the as-received Ni samples and the result of its decomposition into three lifetime components (on top) and respective residual plot (on bottom).

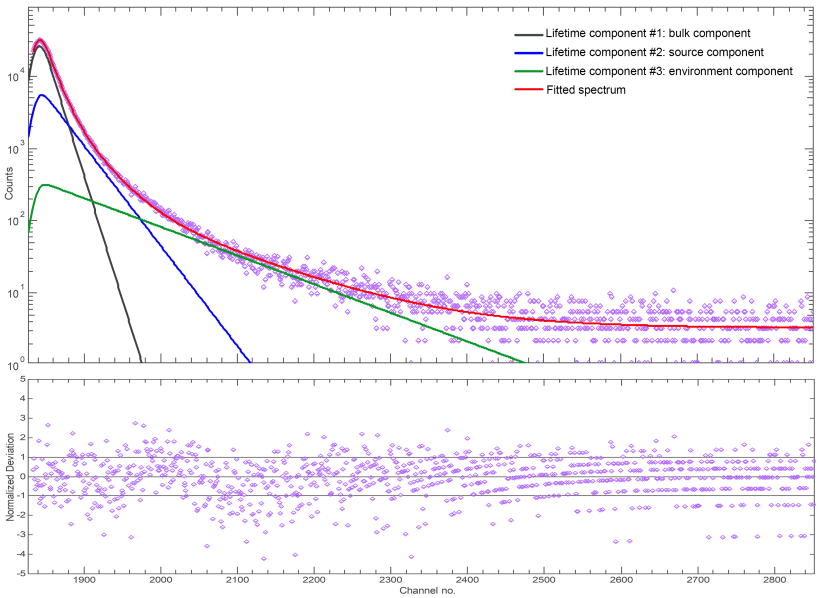

Figure 5.2: Experimental lifetime spectrum acquired with the as-received Cu samples and the result of its decomposition into three lifetime components (on top) and respective residual plot (on bottom).

The results obtained for the fitting parameters are summarised in *Table 5.2* and *5.3*, respectively.

τ_{bulk} (ps)	I_{bulk} (%)	τ_{source} (ps)*	I_{source} (%)	τ_{env} (ps)	I_{env} (%)	Reduced χ^2
144.3 ± 0.9	71.19 ± 0.31	364.9	25.19 ± 0.37	1395.7 ± 22.2	3.62 ± 0.08	1.169

Table 5.2: Lifetimes and respective relative intensities of the lifetime components resultant from the deconvolution of the lifetime spectrum acquired with the as-received Ni samples.
* Value fixed during the fitting process.

τ_{bulk} (ps)	I_{bulk} (%)	τ_{source} (ps)*	I_{source} (%)	τ_{env} (ps)	I_{env} (%)	Reduced χ^2
147.5 ± 0.9	71.43 ± 0.34	364.9	24.80 ± 0.42	1276.0 ± 21.3	3.77 ± 0.10	1.145

Table 5.3: Lifetimes and respective relative intensities of the lifetime components resultant from the deconvolution of the lifetime spectrum acquired with the as-received Cu samples.
* Value fixed during the fitting process.

For both cases, the reduced χ^2 values are rather close to 1, signifying pretty good fits and consequently reliable results. Since these are as-received samples, they very likely contain some defects inside acting as trapping sites for the positrons, from where they annihilate with a different lifetime. This should result in two lifetime components associated with positron annihilations in the sample arising in the spectrum, however, a four component fit was not achievable. Hence, the found bulk component encapsulates the effect of both annihilation channels and is thus, as expected, considerably larger than the literature values.

Annealed nickel and copper samples

This was followed by the analysis of the annealed nickel and copper samples. Each spectrum was again decomposed into three discrete lifetime components, corresponding to the same annihilation channels as before. For the annealed Ni spectrum, all fitting parameters were freely fitted by the software and the exact same initial values of the previous analysis were used. For the Cu case, the only difference was that the τ_{source} parameter was fixed to the computed value of 364.9 ps. The experimentally obtained lifetime spectra, together with their constituent lifetime components and respective residual plot are presented in *Figures 5.3* and *5.4*, respectively, for nickel and copper.

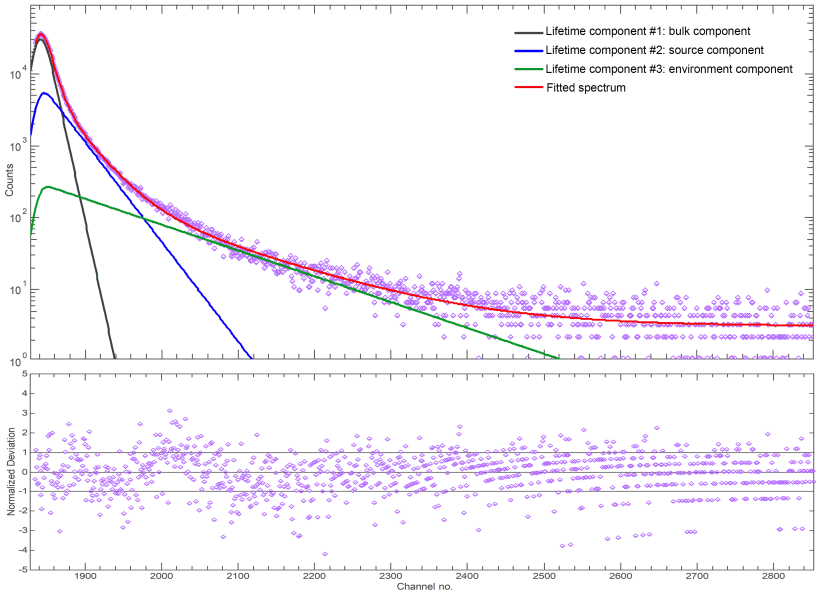

Figure 5.3: Experimental lifetime spectrum acquired with the annealed Ni samples and the result of its decomposition into three lifetime components (on top) and respective residual plot (on bottom).

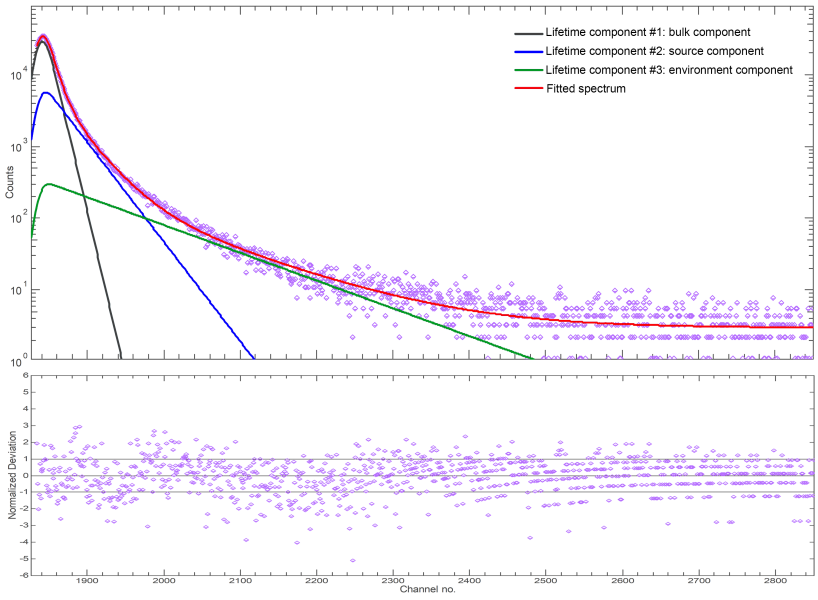

Figure 5.4: Experimental lifetime spectrum acquired with the annealed Cu samples and the result of its decomposition into three lifetime components (on top) and respective residual plot (on bottom).

The values obtained for the fitting parameters are expressed in, respectively, *Table 5.4* and *5.5*.

τ_{bulk} (ps)	I_{bulk} (%)	τ_{source} (ps)	I_{source} (%)	τ_{env} (ps)	I_{env} (%)	Reduced χ^2
102.3 ± 1.0	72.13 ± 0.47	364.9 ± 5.4	24.40 ± 0.40	1408.8 ± 29.9	3.47 ± 0.13	1.155

Table 5.4: Lifetimes and respective relative intensities of the lifetime components resultant from the deconvolution of the lifetime spectrum acquired with the annealed Ni samples.

τ_{bulk} (ps)	I_{bulk} (%)	τ_{source} (ps) *	I_{source} (%)	τ_{env} (ps)	I_{env} (%)	Reduced χ^2
111.2 ± 0.7	70.73 ± 0.20	364.9	25.65 ± 0.27	1307.5 ± 19.9	3.62 ± 0.08	1.189

Table 5.5: Lifetimes and respective relative intensities of the lifetime components resultant from the deconvolution of the lifetime spectrum acquired with the as-received Cu samples.
* Value fixed during the fitting process.

Once again, good fits were produced and reliable results were achieved as both reduced χ^2 values are fairly close to 1. This time, however, the values obtained for the bulk lifetimes are much closer to the expected bulk lifetimes found in literature of 106.96 ps and 116.19 ps, for nickel and copper, respectively, as in fact they differ only 4.36% and 4.49% from the average value, for nickel and copper, respectively. Given that the conditions employed for the acquisition of these spectra were the same as for the spectra of the as-received samples, this enormous improvement can only be attributed to the annealing of the samples. It can then be concluded that the annealing was in fact successful at eliminating the defect concentration to a degree below the PALS technique sensitivity, resulting in that only one actual lifetime component, corresponding to positron annihilations in the bulk of the samples, was expected. It is interesting to see that the relative intensities of the source and environment components are practically the same as before, which was expected since the only difference from the previous case is that the samples have undergone an annealing process, therefore maintaining their density, thickness and atomic number, the aspects upon which these intensities depend.

Electronic-grade silicon samples

Lastly, the EG-Si samples were studied. For the analysis of the acquired spectrum, three discrete lifetime components were also considered in the fitting software, corresponding once more to free positron annihilations in the bulk of the sample, the radioactive source and the surrounding environment. All the fitting parameters, besides τ_{source}, which was set to its pre-determined value, were left unconstrained. As before, the lifetime of the bulk component was set to the average value computed with results from various studies, which, for EG-Si, is equal to 179.33 ps and the τ_{env} was simply set to an estimate of the expected value based on the previous analysis. Both the experimental lifetime spectrum, decomposed into the three considered lifetime components and its associated residual plot are shown in *Figure 5.5*.

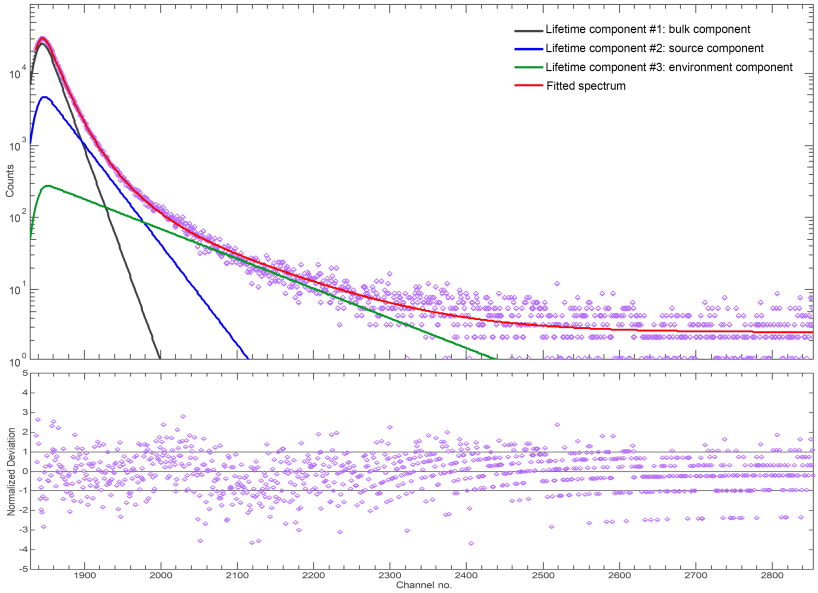

Figure 5.5: Experimental lifetime spectrum acquired with the EG-Si samples and the result of its decomposition into three lifetime components (on top) and respective residual plot (on bottom).

The lifetime and relative intensity results are displayed in *Table 5.6*.

τ_{bulk} (ps)	I_{bulk} (%)	τ_{source} (ps) *	I_{source} (%)	τ_{env} (ps)	I_{env} (%)	Reduced χ^2
171.7 ± 1.1	75.48 ± 0.47	364.9	21.35 ± 0.56	1223.8 ± 23.9	3.17 ± 0.11	1.136

Table 5.6: Lifetimes and respective relative intensities of the lifetime components resultant from the deconvolution of the lifetime spectrum acquired with the EG-Si samples.
* Value fixed during the fitting process.

The bulk lifetime results are not only reliable, due to the reduced χ^2 value being close to 1, but also reasonably accurate as only a difference of 4.26% between the obtained and expected value of 179.33 ps is observed. This percentage is similar to the ones registered for the annealed nickel and copper samples and just like with those samples, the obtained lifetime is lower than the average value found in literature. These consistent disparities might be an indication of a systematic error in our system, that is perhaps transmitted to the results obtained, but to assert this beyond a shadow of a doubt this details requires to be explored in more detail in studies to come.

Summary of positron lifetime results for the metallic and semiconductor reference samples

For an easier interpretation of the results obtained from the analysis of the lifetime spectra acquired for all metallic and semiconductor samples, the final results for the bulk lifetime (the only lifetime component

associated with annihilation in the samples considered during the fitting process) found in our work are compared with the values reported in literature, in *Table 5.7*.

Material	Bulk lifetime of as-received sample (ps)	Bulk lifetime of annealed sample (ps)	Bulk lifetime from literature (ps)	Deviation from average value (%)
Ni	144.3 ± 0.9	102.3 ± 1.0	106.96	4.36
Cu	147.5 ± 0.9	111.2 ± 0.7	116.19	4.49
EG-Si	171.7 ± 1.1	-	179.33	4.26

Table 5.7: Bulk lifetimes obtained from the deconvolution of the lifetime spectra acquired with the as-received and annealed Ni and Cu samples and EG-Si samples, compared with the respective values reported in literature.

5.2.2 Polymeric reference samples

Following a rather fruitful examination of the metallic and semiconductor reference samples, a study of the Teflon® and Polycarbonate collected spectra ensued. An effort was made to decompose each spectrum into the five expected components, which, from shortest to longest were ascribed to: (i) a mixture of free p-Ps atoms annihilations in the bulk of the material and an unknown contribution, (ii) the source contribution of fixed lifetime, (iii) the free positrons annihilations in the bulk of the material, (iv) trapped o-Ps atoms annihilations in the material's free volume structure and (v) positron annihilations in the surrounding environment. In fact, a six component decomposition was also possible for Teflon® as two lifetime components associated to o-Ps annihilations in free volumes are sometimes reported.

However, fits containing so many free parameters to be fitted were impossible to produce and instead a three component fit was achieved for each spectrum, containing solely the lifetime components corresponding to free p-Ps atoms, free positrons and trapped o-Ps atoms annihilations in the sample, respectively, with lifetimes and relative intensities τ_1 and I_1, τ_2 and I_2 and τ_3 and I_3 as the the source and environment components could not be resolved. An additional attempt was made to consider the longest lifetime component in each spectrum as a distribution of lifetimes, resulting from a possible free volume's size distribution in the samples. Nevertheless, when this situation was forced into the fitting procedure, the program produced a distribution with a variance equal to 0 as no such distribution was present in the spectra and so this hypothesis was discarded.

Therefore, a three discrete lifetime component analysis was performed, with every parameter freely estimated by the software, with the respective initial lifetime values set for 300, 800 and 3000 ps, for Teflon® and 200, 500 and 2000 ps, for Polycarbonate as these values were in the range of the ones published in studies that consider three lifetime components for these materials. The acquired spectra with their corresponding lifetime decomposition and residual plot are displayed in *Figures 5.6* and *5.7*, respectively for Teflon® and Polycarbonate.

The results obtained for the lifetimes and associated relative intensities of each lifetime component are, respectively, expressed in *Tables 5.8* and *5.9*.

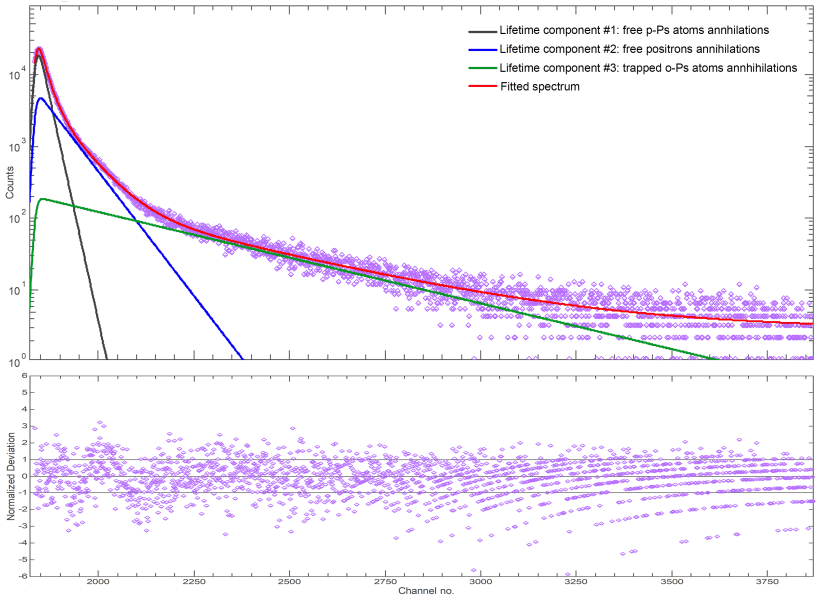

Figure 5.6: Experimental lifetime spectrum acquired with the Teflon® samples and the result of its decomposition into three lifetime components (on top) and respective residual plot (on bottom).

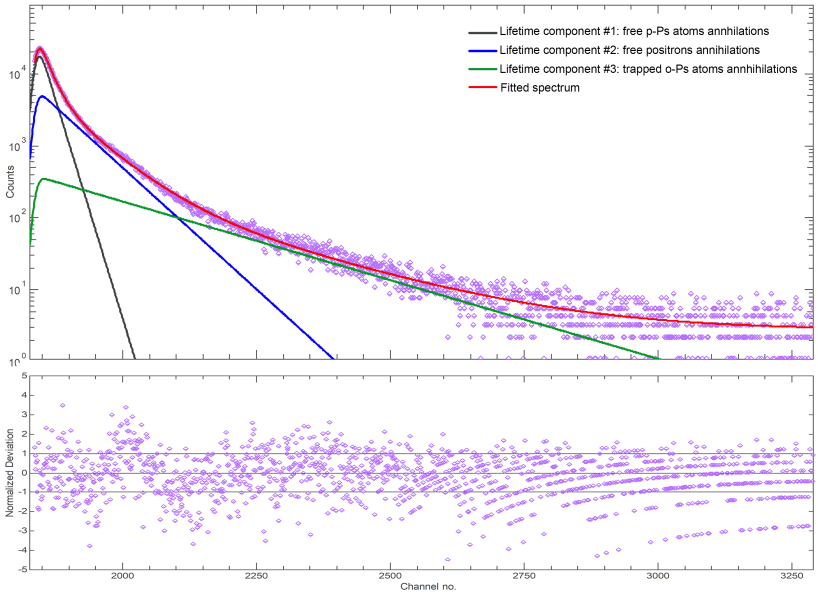

Figure 5.7: Experimental lifetime spectrum acquired with the Polycarbonate samples and the result of its decomposition into three lifetime components (on top) and respective residual plot (on bottom).

τ_1 (ps)	I_1 (%)	τ_2 (ps)	I_2 (%)	τ_3 (ps)	I_3 (%)	Reduced χ^2
207.3 ± 1.5	58.40 ± 0.42	731.3 ± 6.9	35.36 ± 0.37	3977.4 ± 63.1	6.24 ± 0.09	1.234

Table 5.8: Lifetimes and respective relative intensities of the lifetime components resultant from the deconvolution of the lifetime spectrum acquired with the Teflon® samples.

τ_1 (ps)	I_1 (%)	τ_2 (ps)	I_2 (%)	τ_3 (ps)	I_3 (%)	Reduced χ^2
208.5 ± 1.8	55.85 ± 0.48	748.8 ± 9.8	37.13 ± 0.35	2312.9 ± 45.0	7.02 ± 0.29	1.301

Table 5.9: Lifetimes and respective relative intensities of the lifetime components resultant from the deconvolution of the lifetime spectrum acquired with the Polycarbonate samples.

When analysing both tables, the first aspect that draws the attention is the slightly higher values of the reduced χ^2, when compared to the ones attained before, which is likely the result of the decomposition of five components spectra into only three, with two of them accommodating the effects of the two rather intense missing components. In spite of that, the reduced χ^2 are not significantly away from the desired value of 1 for the fits and results to be considered reliable. For Teflon®, the results obtained are quite satisfying as not only is the longest lifetime component rather similar to the one reported in [132], but most impressively, all three lifetimes values are in excellent agreement with the ones obtained in [117]. Conversely, it is only the shortest lifetime found for Polycarbonate that is in excellent agreement with the values commonly attained, despite the fact that τ_3 is still relatively close to the expected. It is important to note that the longest lifetime component is, in this analysis, attributed to o-Ps annihilations in the free volumes since the values obtained for both samples are fairly different from the previous results ascribed to the environment component, the only other long lifetime component, and therefore can not be viewed as such. In terms of relative intensities, it is far more complicated to compare the achieved values to the reported ones as a good agreement even between published studies has not yet been properly reached. Even so, it is possible to verify that, for both polymers, I_3 is appreciably smaller than foreseen. All these observed discrepancies, however, are easily justified by differences in density or in concentration and size of internal free volumes, that are often observed amongst samples of the same polymer and that significantly alter the behaviour of positrons inside the samples and consequently the observed results.

5.3 PALS results for the polymeric samples

Up until now, the analysis of the metallic, semiconductor and polymeric reference samples produced more than satisfactory lifetime results in good agreement with the conclusions reported in literature. As well as that, a lot of experience was gained concerning the analysis method and its intricacies and constraints with the study of all samples, but in particular of Teflon® and Polycarbonate. Therefore, it was decided that it was now time to start studying the PE-g-HEMA films and Chitosan based membranes developed by the research group, that have been properly described in *Section 3.5.3*. It is important to remember that, given the very small thickness of these samples, in order to properly acquire their lifetime spectra without an immense undesired contribution from surrounding positron annihilations, an annealed Ni sample was placed in either side of the sample+source sandwich, thus an additional lifetime component, corresponding to annihilations within Ni, was taken into account.

For the first try, six lifetime components were considered in each spectrum, corresponding to: free positron annihilations in the bulk of the annealed Ni samples, a combination of free p-Ps atoms annihilations in the bulk of the materials and an unknown contribution, positron annihilations in the source set, free positrons annihilations in the bulk of the material, trapped o-Ps atoms annihilations in the material's free volume structure and positron annihilations in the surrounding environment, from shortest to longest. Nonetheless, just like before, a fit with so many unconstrained parameters was not achievable, whereas a fit considering exclusively the lifetime components of the bulk annihilations in annealed Ni and the free p-Ps atoms, free positrons and ttrapped o-Ps atoms annihilations in the polymeric sample, respectively with lifetimes and relative intensities τ_1 and I_1, τ_2 and I_2, τ_3 and I_3 and τ_4 and I_4, could indeed be produced. Similar to what was attempted for the Teflon® and the Polycarbonate samples,

a spectrum analysis run was performed with the longest lifetime component assumed to be a distribution of lifetimes, which for polymers is quite likely to arise. However, in neither of the runs was the program capable of fitting any lifetime distribution to the spectrum and thus this hypothesis was again rejected. Consequently, a four discrete lifetime component analysis of the spectra was carried out, with the shortest lifetime fixed to 102.3 ps (the value previously found for the bulk lifetime component in our annealed Ni samples), while all the remaining parameters were freely estimated by the program. Their initial lifetime values were set for the educated guesses of 200, 500 and 2000 ps, for all studied samples, which were assumed as typical values for these lifetime components in polymers. The spectra acquired for the Samples 1, 2, 3 and 4 are represented in *Figures 5.8*, *5.9*, *5.10* and *5.11*, respectively, where their decomposition into the four lifetime components and residual plot are also displayed.

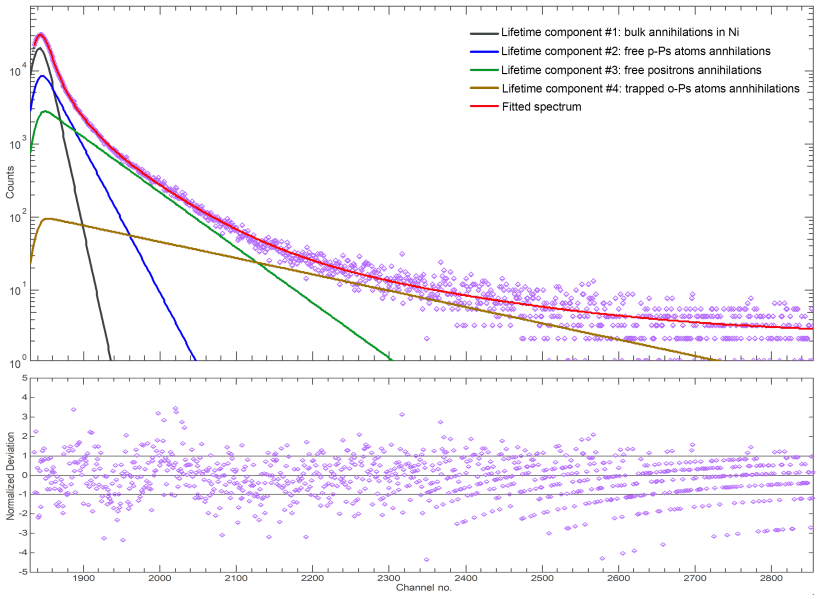

Figure 5.8: Experimental lifetime spectrum acquired with the Sample 1 films and the result of its decomposition into four lifetime components (on top) and respective residual plot (on bottom).

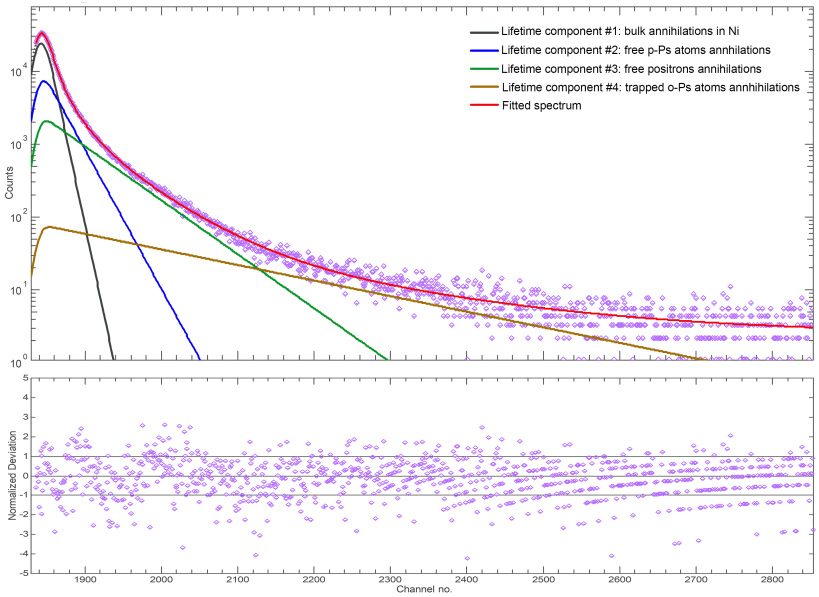

Figure 5.9: Experimental lifetime spectrum acquired with the Sample 2 films and the result of its decomposition into four lifetime components (on top) and respective residual plot (on bottom).

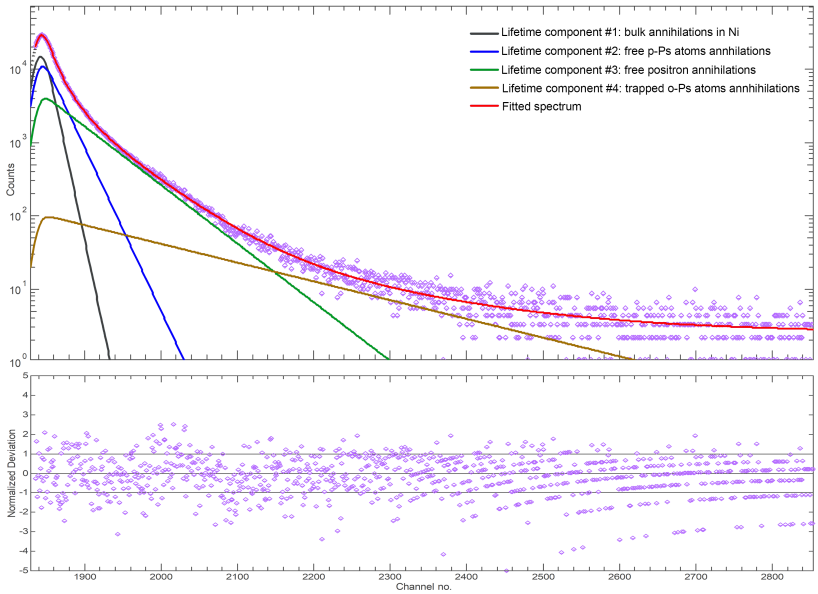

Figure 5.10: Experimental lifetime spectrum acquired with the Sample 3 membranes and the result of its decomposition into four lifetime components (on top) and respective residual plot (on bottom).

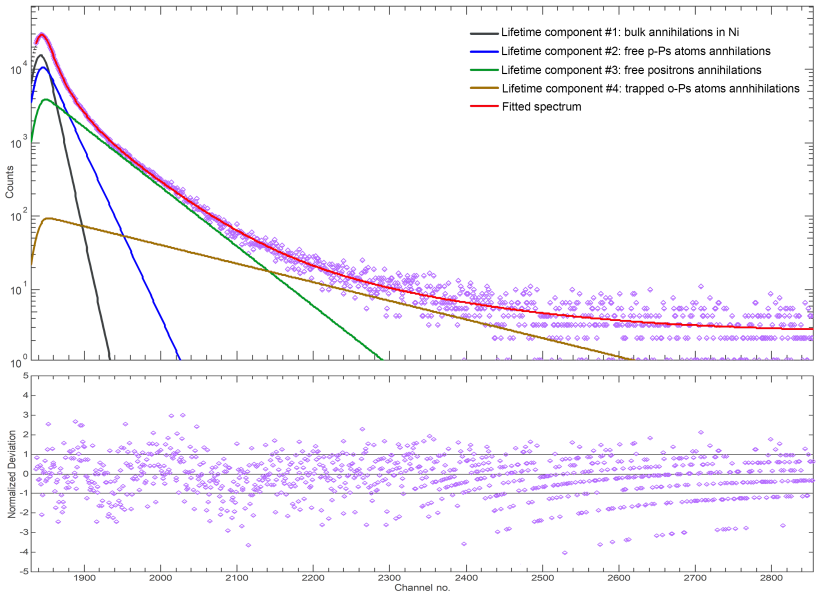

Figure 5.11: Experimental obtained lifetime spectrum acquired with the Sample 4 membranes and the result of its decomposition into four lifetime components (on top) and respective residual plot (on bottom).

The final results for the lifetimes and associated relative intensities obtained for all samples are summarised in *Table 5.10*. The reduced χ^2 values achieved, which are not presented in the table, were respectively, 1.152, 1.098, 1.100 and 1.148, which signifies reliable fits and results. As expected, the most intense component is the one associated to annihilations in the annealed Ni samples, which is explained due to their much larger thickness compared to the polymeric samples. Although there is no possible comparison with literature values since these are novel samples developed by the research group and since no previous PALS measurement had been performed with them, it is still possible to conclude that the attained lifetime values are within an expected range for polymers. Like before, it is important to ensure that the longest component is in fact associated with o-Ps annihilations in the free volume structure

within the samples and not with annihilations in the surroundings, which is easily confirmed due to the fact that the values obtained for τ_4 are rather different from the τ_{env} determined in previous analysis.

Sample	τ_1 (ps) *	I_1 (%)	τ_2 (ps)	I_2 (%)	τ_3 (ps)	I_3 (%)	τ_4 (ps)	I_4 (%)
1	102.3	47.89 ± 0.84	253.8 ± 8.8	30.81 ± 0.70	669.7 ± 19.9	19.40 ± 0.92	2269.5 ± 110.6	1.90 ± 0.18
2		57.10 ± 0.71	264.7 ± 9.6	26.77 ± 0.67	682.9 ± 25.3	14.64 ± 0.89	2368.2 ± 138.6	1.50 ± 0.17
3		35.29 ± 1.22	226.5 ± 7.7	36.60 ± 0.80	631.5 ± 14.6	26.42 ± 0.89	1974.6 ± 119.3	1.69 ± 0.23
4		37.12 ± 1.30	221.6 ± 7.9	35.60 ± 0.84	622.7 ± 14.3	25.64 ± 0.87	1992.4 ± 116.6	1.65 ± 0.21

Table 5.10: Lifetimes and respective relative intensities of the lifetime components resultant from the deconvolution of the lifetime spectrum acquired with each polymeric sample.
*Value fixed during the fitting process.

Since τ_4 is associated with o-Ps annihilations occurring inside the free volumes within the samples, it was then desired to determine the size of the pores where these annihilations were taking place. For this purpose, the τ_4 values were introduced in the Mathematica routine developed for the effect, detailed in *Section 4.2.4*. There, the pores' sizes were determined according to the only three theoretical models for the estimation of free volumes' size whose validity range encompassed the lifetimes determined, namely the Tao-Eldrup, the Tokyo and the Combined Models. The results obtained for each sample, according to each model, in terms of both radius and mean free path of the pore, are expressed in *Table 5.11*.

	Radius (nm)			Mean free path (nm)		
Samples	TE Model	Tokyo Model	Combined Model	TE Model	Tokyo Model	Combined Model
1	0.309	0.312	0.312	0.412	0.416	0.416
2	0.317	0.320	0.320	0.423	0.427	0.427
3	0.283	0.286	0.286	0.377	0.381	0.381
4	0.285	0.287	0.287	0.380	0.383	0.383

Table 5.11: Radius and mean free path values estimated for the free volumes inside each polymeric sample, calculated with the theoretical models valid for the size range in question.

It is interesting to see that the sizes estimated by the Tokyo and the Combined Models are exactly the same since in the studied lifetime range these models are defined by the same exact equation.

The values obtained regarding the PE-g-HEMA films (Samples 1 and 2) show that the increase in the samples' grafting yield from 158% to 403% induces a slight decrease in the respective material's porous size. This decrease, which is lower than expected, may be associated to the higher amount of HEMA grafted to the PE backbone that leads to a more dense structure and therefore to smaller internal pores. These results were an authentic revelation regarding the samples' structural organisation and thus pave the way for new applications of these materials. On the other hand, the results concerning chitosan/PVA membranes (Samples 3 and 4) demonstrate that the introduction of gelatin as a plasticiser agent in the membranes does not compromise their internal free volume structure. Hence, the membranes maintain the adequate structural organisation necessary for their intended biomedical applications, under optimisation by the GREI team involved in biomedical materials research. In order to not only validate the results obtained but also obtain additional information to get a better understanding of the origin of each lifetime component or of the implications of the pores' size, further complementing experimental measurements on these samples, including that of other positron techniques, should be performed.

Chapter 6

Discussion and conclusions

6.1 Conclusions

The first thing to be concluded at the end of our work is that the calibration steps taken, the alterations performed and the performance tests carried out on the experimental setup resulted in a stable spectrometer capable of producing lifetime spectra with a time resolution on par with some of the best resolution values reported in literature.

Furthermore, the results obtained from the analysis of the lifetime spectra acquired with the annealed nickel, annealed copper and EG silicon reference samples are in excellent agreement with the average of previously published literature values. It is also interesting to see that there was a significant difference between the bulk lifetimes attained for the as-received Ni and Cu samples and the annealed ones. This is a testament not only to the ability of the annealing process to essentially eliminate the defects inside a sample but also to the aptitude of both the spectrometer and the employed analysis method to detect changes in the internal structure of materials. For the Teflon® and Polycarbonate samples, the agreement with literature is not so evident but is nevertheless beyond reasonable. This outcome was more than expected as being polymers, slight deviations in characteristics, such as density or internal free volume structure, from those of the samples considered in different published studies can induce an entirely distinct behaviour of positrons inside them and consequently different obtained positron lifetimes.

Even so, these examinations led us to believe that this PALS setup was capable of producing an accurate and precise description of lifetime spectra and, in broader terms, of the free volume structure of the associated samples, whose interpretation strongly depends upon the correct application and validity of the implemented models. They also provided the necessary knowledge of the intricacies, considerations and vital steps of the acquisition and analysis procedures for us to be able to apply the PALS setup for the study of our own polymeric samples. From these last experiments, lifetime and subsequently free volumes' size values within the reasonable and expected range were achieved. In addition, the spectrometer was effective in discerning the different compositions of the samples and the distinct production conditions and parameters involved in their development, by generating contrasting free volumes' sizes amongst them. However, a deeper understanding of the mechanisms involved in the creation of these free volumes and

of the implications of this free volume structure on the samples' performance for their intended purposes requires further measurements and studies, not only with PALS, but also with complementary probing techniques.

From the present observations, it could be concluded that, in the end, we were capable of attaining an optimised PALS spectrometer, a set of acquisition and analysis tools and a broad knowledge of the PALS technique, that together will allow the research group GREI to perform consistently accurate PALS measurements that will shed some light on the free volume structure of the macromolecular materials developed by the group and, more broadly, on their overall behaviour, attributes and performance.

6.2 Future work

Even though we have been able to achieve an optimised and fully operational PALS setup, supplementary improvements and additions can still be performed.

The first one concerns the dependence of the system's time resolution with the angle formed between the detectors, something which has been exhaustively explored in [95] and, to a lesser degree, in [112] and [121]. Therefore, in order to improve the system's timing resolution even further, a set of trials should be carried out, in which the detectors are positioned not facing each other but instead forming various angles between them, while the optimal time resolution of the system is measured, until the position corresponding to the minimum time resolution is found. The only setback is that the current structure in which the detectors are mounted on that does not allow such movement and therefore, prior to these tests, a new supporting structure is needed to provide rotational freedom to the detectors. As well as that, an important set of reproducibility tests should also be conducted to attest the spectrometer's ability to produce identical lifetime spectra and consequently identical results when faced with the same operating conditions as it is expected that any deviations from previous results can only stem from the spectra acquisition process and not from the analysis performed with the PALSfit software. Finally, since in future experiments it may be desired to study the dependence of a sample's internal free volume structure with temperature, it could be pertinent to install, in the detection assembly, a system that enables the variation and maintenance of a certain temperature of the sample under analysis.

With this PALS setup, apart from the study of the multiple macromulecular materials developed by the research group, it would also be interesting to apply it to both an interlaboratory study and a study employing other probing techniques, not only as an additional step to validate the work here performed and to attest the quality of our spectrometer but also to contribute for the standardisation of certain aspects of the PALS technique. We have seen, in the course of this work, that both the occasional omission, in certain published studies, of the acquisition and analysis procedures carried out and the lack of a widely accepted way to perform these procedures greatly impairs the work of both new and experienced researchers and thus it would be extremely important that studies aimed at contributing to an even greater success of the PALS technique could be carried out with this setup.

Bibliography

[1] Dirac, P. A. M. & Fowler, R. H. The quantum theory of the electron. *Proceedings of the Royal Society of London. Series A, Containing Papers of a Mathematical and Physical Character* **117,** 610–624. https://doi.org/10.1098/rspa.1928.0023 (1928).

[2] Dirac, P. A. M. & Fowler, R. H. A theory of electrons and protons. *Proceedings of the Royal Society of London. Series A, Containing Papers of a Mathematical and Physical Character* **126,** 360–365. https://doi.org/10.1098/rspa.1930.0013 (1930).

[3] Anderson, C. D. The positive electron. *Phys. Rev.* **43,** 491–494. https://doi.org/10.1103/PhysRev.43.491 (1933).

[4] Blackett, P. M. S. & Occhialini, G. P. S. Some photographs of the tracks of penetrating radiation. *Proc. Roy. Soc. Lond. A* **139,** 699–720. https://doi.org/10.1098/rspa.1933.0048 (1933).

[5] Heiting, T. Kernanregung durch harte γ-Strahlen. *Naturwissenschaften* **21,** 674. https://doi.org/10.1007/BF01504047 (1933).

[6] Joliot, F. Preuves expérimentales de l'annihilation des électrons positifs. *C. R. Hebd. Acad. Sci* **197,** 1622–1625. https://doi.org/10.1051/jphysrad:0193400507029900 (1933).

[7] Thibaud, J. L'annihilation des positrons au contact de la matière et la radiation qui en résulte. *C.R. Hebd. Acad. Sci* **197,** 1629–1632. https://gallica.bnf.fr/ark:/12148/bpt6k3149q (1933).

[8] Thibaud, J. Positive electrons: focussing of beams, measurement of charge-to-mass ratio, study of absorption and conversion into light. *Phys. Rev.* **45,** 781–787. https://doi.org/10.1103/PhysRev.45.781 (1934).

[9] Klemperer, O. On the annihilation radiation of the positron. *Mathematical Proceedings of the Cambridge Philosophical Society* **30,** 347–354. https://doi.org/10.1017/S0305004100012536 (1934).

[10] Ore, A. & Powell, J. L. Three-photon annihilation of an electron-positron pair. *Phys. Rev.* **75,** 1963. https://doi.org/10.1103/PhysRev.75.1963.2 (1949).

[11] Mohorovičić, S. Möglichkeit neuer Elemente und ihre Bedeutung für die Astrophysik. *Astronomische Nachrichten* **253,** 93–108. https://doi.org/10.1002/asna.19342530402 (1934).

[12] Ruark, A. E. Positronium. *Phys. Rev.* **68,** 278. https://doi.org/10.1103/PhysRev.68.278 (1945).

[13] Deutsch, M. Evidence for the formation of positronium in gases. *Phys. Rev.* **82,** 455–456. https://doi.org/10.1103/PhysRev.82.455 (1951).

[14] Bishay, I., Aly, E. H. & Saadallah, F. A study of annealing stages in commercial pure Cu using mechanical measurements and positron annihilation lifetime technique. *Materials Science and Engineering: A* **527,** 3893–3897. https://doi.org/10.1016/j.msea.2010.02.074 (2010).

[15] Kansy, J., Hanc, A. & Giebel, D. Point defect study in Fe75Al25 and Fe70Al25X5 X=(Cr,Ni) alloys as a function of thermal treatment by positron lifetime spectroscopy. *Physics Procedia* **35.** note: Part of special issue Positron Studies of Defects 2011, 86–91. https://doi.org/10.1016/j.phpro.2012.06.016 (2012).

[16] Kansy, J., Aneta, H. & Giebel, D. Change of the defect structure in FeAl alloy as a result of its aging at ambient temperature. *Nukleonika* **58,** 221–224. http://hdl.handle.net/20.500.12128/14708 (2013).

[17] Dryzek, J. Detection of tribolayer in different metals using positron lifetime spectroscopy. *Tribology International* **131,** 268–276. https://doi.org/10.1016/j.triboint.2018.10.031 (2019).

[18] Lee, C. Y. Positron annihilation Study of vacancy type defects in Ti, Si, and BaSrFBr:Eu. *Applied Science and Convergence Technology* **25,** 85–87. http://dx.doi.org/10.5757/ASCT.2016.25.5.85 (2016).

[19] Bosnar, S., Vrankić, M., Bosnar, D., Ren, N. & Šarić, A. Positron annihilation lifetime spectroscopy (PALS) study of the as prepared and calcined MFI zeolites. *Journal of Physics and Chemistry of Solids* **110,** 227–233. https://doi.org/10.1016/j.jpcs.2017.06.016 (2017).

[20] Nikitina, L., Laptev, R., Abzaev, Y., Lider, A. & Ivashutenko, A. Positron spectroscopy of nanodiamonds after hydrogen sorption. *Nanomaterials* **8,** 36. https://doi.org/10.3390/nano8010036 (2018).

[21] Assis, M., Ponce, M. A., Gouveia, A. F., Souza, D., da Costa, J. P. d. C., Teodoro, V., Gobato, Y. G., Andrés, J., Macchi, C., Somoza, A. & Longo, E. Revealing the nature of defects in α-Ag2WO4 by positron annihilation lifetime spectroscopy: a joint experimental and theoretical study. *Crystal Growth & Design* **21,** 1093–1102. https://doi.org/10.1021/acs.cgd.0c01417 (2021).

[22] DeBenedetti, S. & Richings, H. J. The half-life of positrons in condensed materials. *Phys. Rev.* **85,** 377–378. https://doi.org/10.1103/PhysRev.85.377 (1952).

[23] Brandt, W., Berko, S. & Walker, W. W. Positronium decay in molecular substances. *Phys. Rev.* **120,** 1289–1295. https://doi.org/10.1103/PhysRev.120.1289 (1960).

[24] Brandt, W. & Spirn, I. Positron lifetime spectra in molecular substances. *Phys. Rev.* **142,** 231–237. https://doi.org/10.1103/PhysRev.142.231 (1966).

[25] Tao, S. J. Positronium annihilation in molecular substances. *The Journal of Chemical Physics* **56,** 5499–5510. https://doi.org/10.1063/1.1677067 (1972).

[26] Hamielec, A. E., Eldrup, M. & Mogensen, O. Positron annihilation techniques (PAT) in polymer science and engineering. *Journal of Macromolecular Science, Part C* **9,** 305–337. https://doi.org/10.1080/15583727308545901 (1973).

[27] Eldrup, M., Lightbody, D. & Sherwood, J. The temperature dependence of positron lifetimes in solid pivalic acid. *Chemical Physics* **63,** 51–58. https://doi.org/10.1016/0301-0104(81)80307-2 (1981).

[28] Shpotyuk, O., Bujňáková, Z., Baláž, P., Ingram, A. & Shpotyuk, Y. Positron annihilation lifetime study of polyvinylpyrrolidone for nanoparticle-stabilizing pharmaceuticals. *Journal of Pharmaceutical and Biomedical Analysis* **117,** 419–425. https://doi.org/10.1016/j.jpba.2015.09.030 (2016).

[29] Söylemez, M. A. & Güven, O. Detailed positron annihilation lifetime spectroscopic investigation of atrazine imprinted polymers grafted onto PE/PP non-woven fabrics. *Journal of Molecular Recognition* **31,** e2676. https://doi.org/10.1002/jmr.2676 (2018).

[30] Švajdlenková, H., Šauša, O., Maťko, I., Koch, T. & Gorsche, C. Investigating the free-volume characteristics of regulated dimethacrylate networks below and above glass transition temperature. *Macromolecular Chemistry and Physics* **219,** 1800119. https://doi.org/10.1002/macp.201800119 (2018).

[31] Mahmoud, K. R., El-Shehawy, A. & Atta, H. Positron annihilation spectroscopy of chain-end-functionalized polystyrenes with definite numbers of benzyl alcohol and perfluorooctyl groups. *Polímeros* **29,** e2019046. https://doi.org/10.1590/0104-1428.04619 (2019).

[32] Nuruddin, M., Chowdhury, R., Lopez-Perez, N., Montes, F., Youngblood, J. & Howarter, J. The influence of free volume determined by positron annihilation lifetime spectroscopy (PALS) on gas permeability of cellulose nanocrystals films. *ACS Applied Materials & Interfaces* **12,** 24380–24389. https://doi.org/10.1021/acsami.0c05738 (2020).

[33] Husband, P., Bartošová, I., Slugen, V. & Selim, F. Positron annihilation in transparent ceramics. *Journal of Physics: Conference Series* **674,** 012013. https://doi.org/10.1088/1742-6596/674/1/012013 (2016).

[34] Klym, H., Ingram, A., Shpotyuk, O., Hadzaman, I., Solntsev, V., Hotra, O. & Popov, A. I. Positron annihilation characterization of free volume in micro- and macro-modified Cu0.4Co0.4Ni0.4Mn1.8O4 ceramics. *Low Temperature Physics* **42,** 601–605. https://doi.org/10.1063/1.4959021 (2016).

[35] Klym, H., Ingram, A., Hadzaman, I., Karbovnyk, I., Vasylchyshyn, I. & Popov, A. I. Nanoporous characterization of modified humidity-sensitive MgO-Al2O3 ceramics by positron annihilation lifetime spectroscopy method. *IOP Conference Series: Materials Science and Engineering* **503,** 012019. https://doi.org/10.1088/1757-899x/503/1/012019 (2019).

[36] Pham, B., Guagliardo, P., Williams, J., Samarin, S. & Smith, S. V. A study of porosity of synthetic polymer nanoparticles using PALS. *Journal of Physics: Conference Series* **262,** 012048. https://doi.org/10.1088/1742-6596/262/1/012048 (2011).

[37] Akmalova, Y. A., Dubov, L. Y., Stepanov, S. V., Shtotsky, Y. V. & Timoshenko, V. Y. Positron lifetime spectroscopy of silicon nanocontainers for cancer theranostic applications. *KnE Energy* **3,** 1–9. https://doi.org/10.18502/ken.v3i2.1784 (2018).

[38] Heikinheimo, J. *Applications of positron annihilation spectroscopy in nuclear materials research* Doctoral thesis (School of Science, 2017), 65 + app. 49. https://aaltodoc.aalto.fi/handle/123456789/29557.

[39] Ding, Z., Zhang, C., Zhang, X., Chen, Y., Yang, Y., Song, Y., Liu, X. & Xue, F. Post-irradiation annealing behavior of irradiation hardening of China low-Cu RPV steel. *Nuclear Materials and Energy* **22,** 100727. https://doi.org/10.1016/j.nme.2020.100727 (2020).

[40] Zibrov, M., Egger, W., Heikinheimo, J., Mayer, M. & Tuomisto, F. Vacancy cluster growth and thermal recovery in hydrogen-irradiated tungsten. *Journal of Nuclear Materials* **531,** 152017. https://doi.org/10.1016/j.jnucmat.2020.152017 (2020).

[41] Pietrzak, R., Borbulak, S. & Szatanik, R. Influence of neoplastic therapy on the investigated blood using positron annihilation lifetime spectroscopy. *Nukleonika* **58,** 199–202. https://repo.uni.opole.pl/info/article/UOde8a69c062c3423da6f716c4c0e4336b/ (2013).

[42] Jasińska, B., Zgardzińska, B., Chołubek, G., Gorgol, M., Wiktor, K., Wysogląd, K., Białas, P., Curceanu, C., Czerwiński, E., Dulski, K. & et al. Human tissues investigation using PALS technique. *Acta Physica Polonica B* **48,** 1737–1747. https://doi.org/10.5506/APhysPolB.48.1737 (2017).

[43] Jasińska, B., Zgardzińska, B., Chołubek, G., Pietrow, M., Gorgol, M., Wiktor, K., Wysogląd, K., Bialas, P., Curceanu, C., Czerwiński, E., Dulski, K., Gajos, A., Głowacz, B., Hiesmayr, B., Jodlowska-Jedrych, B., Kamińska, D., Korcyl, G., Kowalski, P., Kozik, T. & Moskal, P. Human tissue investigations using PALS technique-free radicals influence. *Acta Physica Polonica A* **132,** 1556–1559. https://doi.org/10.12693/APhysPolA.132.1556 (2017).

[44] Moskal, P., Kisielewska, D., Curceanu, C., Czerwiński, E., Dulski, K., Gajos, A., Gorgol, M., Hiesmayr, B., Bozena, J., Kacprzak, K., Kapłon, Ł., Korcyl, G., Kowalski, P., Krzemien, W., Kozik, T., Kubicz, E., Mohammed, M., Niedźwiecki, S., Palka, M. & Zgardzińska, B. Feasibility study of the positronium imaging with the J-PET tomograph. *Physics in Medicine and Biology* **64,** 055017. https://doi.org/10.1088/1361-6560/aafe20 (2019).

[45] Zgardzińska, B., Chołubek, G., Jarosz, B., Wysogląd, K., Gorgol, M., Goździuk, M., Chołubek, M. & Jasińska, B. Studies on healthy and neoplastic tissues using positron annihilation lifetime spectroscopy and focused histopathological imaging. *Scientific Reports* **10,** 11890. https://doi.org/10.1038/s41598-020-68727-3 (2020).

[46] Bosnar, D., Fríščić, I., Jerbić-Zorc, G., Makek, M. J. & Bosnar, S. Applications of positron annihilation spectroscopy. *Proceedings of International Topical Meeting on Nuclear Research Applications and Utilization of Accelerators, 4-8 May 2009, Vienna.* http://inis.iaea.org/search/search.aspx?orig_q=RN:41127804 (2010).

[47] Fang, M., Bartholomew, N. & Fulvio, A. D. *Timing performance of organic scintillators for positron annihilation lifetime spectroscopy* in *2019 IEEE Nuclear Science Symposium and Medical Imaging Conference, NSS/MIC 2019* (Institute of Electrical and Electronics Engineers Inc., 2019), pp. 1–5. https://doi.org/10.1109/NSS/MIC42101.2019.9059732.

[48] Petschke, D. & Staab, T. E. DDRS4PALS: A software for the acquisition and simulation of lifetime spectra using the DRS4 evaluation board. *SoftwareX* **10,** 100261. https://doi.org/10.1016/j.softx.2019.100261 (2019).

[49] Casimiro, M., Silva, A., Alvarez, R., Ferreira, L., Ramos, A. & Vital, J. PVA supported catalytic membranes obtained by gamma-irradiation for biodiesel production. *Radiation Physics And Chemistry* **94,** 171–175. https://doi.org/10.1016/j.radphyschem.2013.05.058 (2014).

[50] Lancastre, J. J., Falcão, A. N., Margaça, F. M., Ferreira, L. M., Salvado, I. M. M., Casimiro, M. H., Almásy, L. & Meiszterics, A. Influence of the polymer molecular weight on the microstructure of hybrid materials prepared by γ-irradiation. *Radiation Physics and Chemistry* **106,** 126–129. https://doi.org/10.1016/j.radphyschem.2014.06.023 (2015).

[51] Lancastre, J. J., Falcão, A. N., Margaça, F. M., Ferreira, L. M., Salvado, I. M. M., Almásy, L., Casimiro, M. H. & Meiszterics, A. Nanostructure of PDMS–TEOS–PrZr hybrids prepared by direct deposition of gamma radiation energy. *Applied Surface Science* **352,** 91–94. https://doi.org/10.1016/j.apsusc.2015.01.224 (2015).

[52] Casimiro, M., Lancastre, J., Rodrigues, A., Gomes, S., Rodrigues, G. & Ferreira, L. Chitosan-based matrices prepared by gamma irradiation for tissue regeneration: structural properties vs. preparation method. *Topics in Current Chemistry* **375,** 5. https://doi.org/10.1007/s41061-016-0092-5 (2017).

[53] Evans, R. *The atomic nucleus* https://www.worldcat.org/title/atomic-nucleus/oclc/542611 (McGraw Hill Book Company, Inc, 1955).

[54] Charlton, M. & Humberston, J. W. *Positron Physics* https://doi.org/10.1017/CBO9780511535208 (Cambridge University Press, 2000).

[55] Stepanov, S. V. & Byakov, V. M. *Physical and Radiation Chemistry of the Positron and Positronium* in *Principles and applications of positron and positronium chemistry* (eds Jean, Y. C., Mallon, P. E. & Schrader, D. M.) 117 (World Scientific, 2004). https://doi.org/10.1142/5086.

[56] Stepanov, S. V., Byakov, V. M. & Kobayashi, Y. Positronium formation in molecular media: The effect of the external electric field. *Phys. Rev. B* **72,** 054205. https://doi.org/10.1103/PhysRevB.72.054205 (2005).

[57] Stepanov, S., Byakov, V. & Hirade, T. To the theory of Ps formation. New interpretation of the e + lifetime spectrum in water. *Radiation Physics and Chemistry* **76,** 90–95. https://doi.org/10.1016/j.radphyschem.2006.03.012 (2007).

[58] Stepanov, S., Mikhin, K., Zvezhinskiy, D. & Byakov, V. Energy dissipation and Ps bubble growth in liquids. *Radiation Physics and Chemistry* **76,** 275–279. https://doi.org/10.1016/j.radphyschem.2006.03.050 (2007).

[59] Mogensen, O. E. Spur reaction model of positronium formation. *The Journal of Chemical Physics* **60,** 998–1004. https://doi.org/10.1063/1.1681180 (1974).

[60] Procházka, I. Positron annihilation spectroscopy. *Materials Structure* **8,** 55–60. http://www.xray.cz/ms/bul2001-2/prochazka.pdf (2001).

[61] Nakanishi, H. & Jean, Y. *Positrons and positronium in liquids. Chapter 5* in *Positron and positronium chemistry* (eds Schrader, D. & Jean, Y.) (Elsevier, Netherlands, 1988). ISBN: 9780444430090. http://inis.iaea.org/search/search.aspx?orig_q=RN:20043033.

[62] Ito, K., Nakanishi, H. & Ujihira, Y. Extension of the equation for the annihilation lifetime of orthopositronium at a cavity larger than 1 nm in radius. *The Journal of Physical Chemistry B* **103,** 4555–4558. https://doi.org/10.1021/jp9831841 (1999).

[63] Thraenert, S., Hassan, E., Enke, D., Fuerst, D. & Krause-Rehberg, R. Verifying the RTE model: Ortho-positronium lifetime measurement on controlled pore glasses. *Physica Status Solidi c* **4,** 3819–3822. https://doi.org/10.1002/pssc.200675738 (2007).

[64] Dull, T., Frieze, W., Gidley, D., Sun, J. & Yee, A. Determination of pore size in mesoporous thin films from the annihilation lifetime of positronium. *Journal of Physical Chemistry B* **105,** 4657–4662. https://doi.org/10.1021/jp004182v (2001).

[65] Zaleski, R., Kierys, A., Dziadosz, M., Goworek, J. & Halasz, I. Positron annihilation and N2 adsorption for nanopore determination in silica-polymer composites. *RSC Advances* **2,** 3729–3734. https://doi.org/10.1039/C2RA20147J (2012).

[66] Thanh, N. D., Dung, T. Q., Tuyên, L. A. & Tuan, K. T. Semi-empirical formula for large pore-size estimation from the o-Ps annihilation lifetime. *International Journal of Nuclear Energy Science and Technology* **4,** 81. https://doi.org/10.1504/IJNEST.2008.020528 (2008).

[67] Tuyen, L., Dong Xuan, T., Tuan Kiet, H., Chi Cuong, L., Trong Phuc, P., Duy Tap, T., Phuc, D.-V., Nguyen, L., Ngoc Hue, N., Thi Hue, P., Thai Son, L., Van Hoang, D., Hoang Long, N. & Quang Hung, N. A hybrid model for estimation of pore size from ortho-positronium lifetimes in porous materials. *Radiation Physics and Chemistry* **172,** 108867. https://doi.org/10.1016/j.radphyschem.2020.108867 (2020).

[68] Gidley, D., Frieze, W., Dull, T., Yee, A., Ryan, E. & Ho, H. M. Positronium annihilation in mesoporous thin films. *Physical Review B* **60,** R5157–R5160. https://doi.org/10.1103/physrevb.60.r5157 (1999).

[69] Gidley, D. W., Marko, K. A. & Rich, A. Precision measurement of the decay rate of orthopositronium in SiO_2 powders. *Phys. Rev. Lett.* **36,** 395–398. https://doi.org/10.1103/PhysRevLett.36.395 (1976).

[70] Wada, K. & Hyodo, T. A simple shape-free model for pore-size estimation with positron annihilation lifetime spectroscopy. *Journal of Physics: Conference Series* **443,** 012003. https://doi.org/10.1088/1742-6596/443/1/012003 (2013).

[71] Jean, Y. C., Mallon, P. E. & Schrader, D. M. *Principles and Applications of Positron and Positronium Chemistry* https://www.worldscientific.com/doi/abs/10.1142/5086 (WORLD SCIENTIFIC, 2003).

[72] *Scionix Holland* https://scionix.nl/.

[73] *Hamamatsu Photonics* https://www.hamamatsu.com/jp/en/index.html.

[74] *FAST ComTec GmbH* https://www.fastcomtec.com/.

[75] *Ametek Ortec* https://www.ortec-online.com/.

[76] *Mirion Tecnhonolgies // Canberra BNLS* https://www.canberra.com/cbns/.

[77] Das, S. A simple alternative to the Crystal Ball function. *arXiv: High Energy Physics-Experiment.* https://arxiv.org/abs/1603.08591 (2016).

[78] Olsen, J. V. P. K., Pedersen, N. J. & Eldrup, M. M. PALSfit: A new program for the evaluation of positron lifetime spectra. *Physica Status Solidi. C: Current Topics in Solid State Physics* **4,** 4004–4006. https://doi.org/10.1002/pssc.200675868 (2007).

[79] Kirkegaard, P., Pedersen, N. & Eldrup, M. *PATFIT-88: A Data-Processing System for Positron Annihilation Spectra on Mainframe and Personal Computers* English. *Risø-M* **2740.** ISBN: 87-550-1491-7. https://orbit.dtu.dk/en/publications/patfit-88-a-data-processing-system-for-positron-annihilation-spec (Risø National Laboratory, 1989).

[80] Giebel, D. & Kansy, J. LT10 Program for Solving Basic Problems Connected with Defect Detection. *Physics Procedia* **35.** Positron Studies of Defects 2011, 122–127. https://doi.org/10.1016/j.phpro.2012.06.022 (2012).

[81] Kansy, J. Microcomputer program for analysis of positron annihilation lifetime spectra. *Nuclear Instruments and Methods in Physics Research Section A: Accelerators, Spectrometers, Detectors and Associated Equipment* **374,** 235–244. https://doi.org/10.1016/0168-9002(96)00075-7 (1996).

[82] Shukla, A., Peter, M. & Hoffmann, L. Analysis of positron lifetime spectra using quantified maximum entropy and a general linear filter. *Nuclear Instruments and Methods in Physics Research Section A: Accelerators, Spectrometers, Detectors and Associated Equipment* **335,** 310–317. https://doi.org/10.1016/0168-9002(93)90286-Q (1993).

[83] Shukla, A., Hoffmann, L., Manuel, A. & Peter, M. Melt 4.0 a Program for Positron Lifetime Analysis. *Materials Science Forum* **255-257,** 233–237. https://www.scientific.net/MSF.255-257.233 (1997).

[84] Gregory, R. B. & Zhu, Y. Analysis of positron annihilation lifetime data by numerical laplace inversion with the program CONTIN. *Nuclear Instruments and Methods in Physics Research Section A: Accelerators, Spectrometers, Detectors and Associated Equipment* **290,** 172–182. https://doi.org/10.1016/0168-9002(90)90358-D (1990).

[85] Gregory, R. B. Free-volume and pore size distributions determined by numerical Laplace inversion of positron annihilation lifetime data. *Journal of Applied Physics* **70,** 4665–4670. https://doi.org/10.1063/1.349057 (1991).

[86] Kanda, G. *Positron annihilation lifetime spectroscopy methodology and application to perovskite oxide materials* Thesis. 2015. https://discovery.dundee.ac.uk/en/studentTheses/positron-annihilation-lifetime-spectroscopy-methodology-and-appli.

[87] *MaTecK* https://mateck.com/.

[88] *ESTAR - Stopping power and range tables for electrons // NIST* https://physics.nist.gov/PhysRefData/Star/Text/ESTAR.html.

[89] *RS AMIDATA* https://pt.rs-online.com/web/.

[90] *Brett Martin* https://www.brettmartin.com/home.

[91] *Autodesk // Fusion 360* https://www.autodesk.pt/products/fusion-360/overview.

[92] Ortec. Experiment 27 - Positron Annihilation Lifetime Spectrometry. https://www.ortec-online.com/-/media/ametekortec/third-edition-experiments/27-positron-annihilation-lifetime-spectrometry.pdf?la=en&revision=f7ac0fd5-8ee1-4502-ae4f-a25ba8c56088&hash=C51B933CD0411388608EFC0318B89AEE (2018).

[93] Gerdau, E., Thiel, T. A. & Netz, G. A fast detector system with cooled NaI-scintillators. *Hyperfine Interactions* **10,** 1155–1160. https://doi.org/10.1007/BF01022068 (1981).

[94] Ortec. Model 583B Constant Fraction Differential Discriminator Operating Manual. https://www.ortec-online.com/-/media/ametekortec/manuals/583b-mnl.pdf?la=en&revision=eca27cf7-cf5c-4daa-9a79-fbe55d6a89e7 (2009).

[95] Bečvář, F., Čížek, J., Lešták, L., Novotný, I., Procházka, I. & Šebesta, F. A high-resolution BaF2 positron-lifetime spectrometer and experience with its long-term exploitation. *Nuclear Instruments and Methods in Physics Research Section A: Accelerators, Spectrometers, Detectors and Associated Equipment* **443,** 557–577. https://doi.org/10.1016/S0168-9002(99)01156-0 (2000).

[96] Ortec. Positron Lifetime System (PLS-SYSTEM) Setup REVISION B. https://www.ortec-online.com/service-and-support/technical-support (2006).

[97] *Wolfram // Mathematica* https://www.wolfram.com/mathematica/.

[98] *ROOT* https://root.cern/.

[99] Wästlund, C., Eldrup, M. & Maurer, F. Interlaboratory comparison of positron and positronium lifetimes in polymers. *Nuclear Instruments and Methods in Physics Research Section B: Beam Interactions with Materials and Atoms* **143,** 575–583. https://doi.org/10.1016/S0168-583X(98)00400-5 (1998).

[100] Ito, K., Oka, T., Kobayashi, Y., Shirai, Y., Wada, K., Matsumoto, M., Fujinami, M., Hirade, T., Honda, Y., Hosomi, H., Nagai, Y., Inoue, K., Saito, H., Sakaki, K., Sato, K., Shimazu, A. & Uedono, A. Interlaboratory comparison of positron annihilation lifetime measurements for synthetic fused silica and polycarbonate. *Journal of Applied Physics* **104,** 026102. https://doi.org/10.1063/1.2957074 (2008).

[101] Ito, K., Oka, T., Kobayashi, Y., Shirai, Y., Wada, K., Matsumoto, M., Fujinami, M., Hirade, T., Honda, Y., Hosomi, H., Nagai, Y., Inoue, K., Saito, H., Sakaki, K., Sato, K., Shimazu, A. & Uedono, A. *Interlaboratory Comparison of Positron Annihilation Lifetime Measurements* in *Positron and Positronium Chemistry* **607** (Trans Tech Publications Ltd, 2009), 248–250. https://doi.org/10.4028/www.scientific.net/MSF.607.248.

[102] Gong, W., Mai, Y., Zhou, Y., Qi, N., Wang, B. & Yan, D. Effect of the Degree of Branching on Atomic-Scale Free Volume in Hyperbranched Poly[3-ethyl-3-(hydroxymethyl)oxetane]. A Positron Study. *Macromolecules* **38,** 9644–9649. https://doi.org/10.1021/ma051026j (2005).

[103] Liu, J., Deng, Q. & Jean, Y. C. Free-volume distributions of polystyrene probed by positron annihilation: comparison with free-volume theories. *Macromolecules* **26,** 7149–7155. https://doi.org/10.1021/ma00078a006 (1993).

[104] Pach-Zawada, K., Filipecki, J., Golis, E., Yousef, E. & Boyko, V. Measurements of Defect Structures by Positron Annihilation Lifetime Spectroscopy of the Tellurite Glass 70TeO2-5XO-10P2O5-10ZnO-5PbF2 (X = Mg, Bi2, Ti) Doped with Ions of the Rare Earth Element Er3+. *Nanoscale Research Letters* **12.** https://doi.org/10.1186/s11671-017-2075-z (2017).

[105] Dong, A. W., Pascual-Izarra, C., Dong, Y.-D., Pas, S. J., Hill, A. J., Boyd, B. J. & Drummond, C. *Positron annihilation lifetime spectroscopy (PALS) and small angle x-ray scattering (SAXS) of self-assembled amphiphiles* in *Device and Process Technologies for Microelectronics, MEMS, Photonics, and Nanotechnology IV* (eds Tan, H. H., Chiao, J.-C., Faraone, L., Jagadish, C., Williams, J. & Wilson, A. R.) **6800** (SPIE, 2008), 290–295. https://doi.org/10.1117/12.759243.

[106] Wang, Y. Y., Nakanishi, H., Jean, Y. C. & Sandreczki, T. C. Positron annihilation in amine-cured epoxy polymers—pressure dependence. *Journal of Polymer Science Part B: Polymer Physics* **28,** 1431–1441. https://doi.org/10.1002/polb.1990.090280902 (1990).

[107] Cangialosi, D., Schut, H., van Veen, A. & Picken, S. J. Positron Annihilation Lifetime Spectroscopy for Measuring Free Volume during Physical Aging of Polycarbonate. *Macromolecules* **36,** 142–147. https://doi.org/10.1021/ma021214z (2003).

[108] Eren, B., Eren, E., Guney, M., Jean, Y.-C. & Van Horn, J. D. Positron annihilation lifetime spectroscopy study of polyvinylpyrrolidone-added polyvinylidene fluoride membranes: Investigation of free volume and permeation relationships. *Journal of Polymer Science* **58,** 589–598. https://doi.org/10.1002/pol.20190031 (2020).

[109] Kansy, J., Consolati, G. & Dauwe, C. Positronium trapping in free volume of polymers. *Radiation Physics and Chemistry* **58,** 427–431. https://doi.org/10.1016/S0969-806X(00)00195-X (2000).

[110] McGuire, S. & Keeble, D. Positron lifetime and implantation in Kapton. *Journal of Physics D* **39,** 3388–3393. https://doi.org/101088/0022-3727/39/15/025 (2006).

[111] Dlubek, G., Buchhold, R., Hübner, C., Nakladal, A. & Sahre, K. Local free volumes in boron-bombarded Kapton polyimide: A positron lifetime study. *Journal of Polymer Science Part B: Polymer Physics* **37,** 2539–2543. https://doi.org/10.1002/(SICI)1099-0488(19990901)37:17<2539::AID-POLB25>3.0.CO;2-7 (1999).

[112] Ross, M. A. *Development and Optimization of a Positron Annihilation Lifetime Spectrometer to Measure Nanoscale Defects in Solids and Borane Cage Molecules in Aqueous Nitrate Solutions* Thesis. 2008. https://www.semanticscholar.org/paper/Development-and-Optimization-of-a-Positron-Lifetime-Ross/2556b694e4ad2e9c5e71d55d568e4342780a035a.

[113] Russell, H., Morton, A. & Keeble, D. Determination of positron annihilation lifetime spectroscopy instrument timing resolution function and source terms using standard samples. *Journal of Physics: Conference Series* **1253,** 012014. https://doi.org/10.1088/1742-6596/1253/1/012014 (2019).

[114] Kansy, J. & Suzuki, T. Delayed formation and localisation of positronium in polymers at low temperatures. *Radiation Physics and Chemistry* **76,** 759–765. https://doi.org/10.1016/j.radphyschem.2006.10.005 (2007).

[115] Kansy, J. A Comparison of Different Theoretical Models of Positron Lifetime Spectra for Polymers. *Acta Physica Polonica A* **113,** 1397–1407. https://doi.org/10.12693/APhysPolA.113.1397 (2008).

[116] Kansy, J. & Suzuki, T. Positronium fraction in polymer spectra determined by ETLA model. *Radiation Physics and Chemistry* **68.** Proceedings of the 7th International Conference on Positron and Positronium Chemistry, 497–500. https://doi.org/10.1016/S0969-806X(03)00217-2 (2003).

[117] Kindl, P., Puff, W. & Sormann, H. A free four-term analysis of positron lifetime spectra of γ-irradiated Teflon. *physica status solidi (a)* **58,** 489–494. https://doi.org/10.1002/pssa.2210580219 (1980).

[118] Karbowski, A., Fidelus, J. & Karwasz, G. Testing an ORTEC lifetime system. *Materials Science Forum* **666,** 155. https://doi.org/10.4028/www.scientific.net/MSF.666 (2010).

[119] Wieland, B. M. *Construction and Testing of a Positron Annihilation Lifetime Spectrometer* Thesis. MA thesis (Idaho State University, 2012). https://sierraapp.library.isu.edu/record=b1953891~S1.

[120] Petschke, D., Helm, R. & Staab, T. Data on pure tin by Positron Annihilation Lifetime Spectroscopy (PALS) acquired with a semi-analog/digital setup using DDRS4PALS. *Data in Brief* **22,** 16–29. https://doi.org/10.1016/j.dib.2018.11.121 (2019).

[121] Dulski, K. *Assembly and calibration of apparatus for Positron Annihilation Lifetime Spectroscopy* Thesis. 2016. http://koza.if.uj.edu.pl/files/45a95b748493f891844cbf6949c57810/Praca%5C%20(watermarked).pdf.

[122] Luís, J. M. M. *Espectroscopia de tempos de vida de aniquilação do positrão no estudo dos processos de relaxação e absorção de humidade num polímero comercial* Thesis. MA thesis (Universidade de Coimbra, 2010). http://hdl.handle.net/10316/13815.

[123] Staab, T., Somieski, B. & Krause-Rehberg, R. The data treatment influence on the spectra decomposition in positron lifetime spectroscopy Part 2: The effect of source corrections. *Nuclear Instruments and Methods in Physics Research Section A: Accelerators, Spectrometers, Detectors and Associated Equipment* **381,** 141–151. https://doi.org/10.1016/0168-9002(96)00585-2 (1996).

[124] McGuire, S. & Keeble, D. J. Positron lifetimes of polycrystalline metals: A positron source correction study. *Journal of Applied Physics* **100,** 103504. https://doi.org/10.1063/1.2384794 (2006).

[125] Sharma, S. K., Sudarshan, K., Sahu, M. & Pujari, P. K. Investigation of free volume characteristics of the interfacial layer in poly(methyl methacrylate)–alumina nanocomposite and its role in thermal behaviour. *RSC Adv.* **6,** 67997–68004. http://dx.doi.org/10.1039/C6RA07051E (72 2016).

[126] Djourelov, N. & Misheva, M. Source correction in positron annihilation lifetime spectroscopy. *Journal of Physics: Condensed Matter* **8,** 2081–2087. https://doi.org/10.1088/0953-8984/8/12/020 (1996).

[127] Kim, S.-J., Kook, S., O'Rourke, B. E., Lee, J., Hwang, M., Kobayashi, Y., Suzuki, R. & Kim, I. S. Characterization of pore size distribution (PSD) in cellulose triacetate (CTA) and polyamide (PA) thin active layers by positron annihilation lifetime spectroscopy (PALS) and fractional rejection (FR) method. *Journal of Membrane Science* **527,** 143–151. https://doi.org/10.1016/j.memsci.2016.12.064 (2017).

[128] Mahony, J., Friessnegg, T., Tessaro, G., Mascher, P. & Puff, W. Transmission of positrons with a β^+ energy distribution through thin films. *Applied Physics A* **63,** 299–301. https://doi.org/10.1007/BF01567885 (1996).

[129] Saoucha, A. Positron transmission into Kapton: The effective mass absorption coefficient of relevance to positron lifetime experiments. *Journal of Applied Physics* **85,** 1802–1810. https://doi.org/10.1063/1.369327 (1999).

[130] Gaydarov, V., Chen, Z., Zamfirova, G., Söylemez, M. A., Zhang, J., Djourelov, N. & Zhang, J. Micromechanical and positron annihilation lifetime study of new cellulose esters with different topological structures. *Carbohydrate Polymers* **219,** 56–62. https://doi.org/10.1016/j.carbpol.2019.05.022 (2019).

[131] Yu, Y. *Positron annihilation lifetime spectroscopy - studies of amorphous and crystalline molecular materials* PhD thesis (Martin-Luther-Universität Halle-Wittenberg, 2011). http://dx.doi.org/10.25673/596.

[132] Tao, S. J. & Green, J. H. A third positron lifetime in solid polymers. *Proceedings of the Physical Society* **85,** 463–467. https://doi.org/10.1088/0370-1328/85/3/307 (1965).

[133] Buchtela, K. *RADIOCHEMICAL METHODS | Gamma-Ray Spectrometry* in *Encyclopedia of Analytical Science (Second Edition)* (eds Worsfold, P., Townshend, A. & Poole, C.) Second Edition, 72–79 (Elsevier, Oxford, 2005). ISBN: 978-0-12-369397-6. https://doi.org/10.1016/B0-12-369397-7/00525-2.

[134] Khan, M. N. G. A., Carswell, D. J. & Bell, J. A study of positron lifetime measurements in Teflon under gamma radiation. *Journal of Physics D: Applied Physics* **1,** 1833–1836. https://doi.org/10.1088/0022-3727/1/12/432 (1968).

[135] Shuying, W., Tianbao, Z., Yanming, S., Haidong, W. & Guangming, Y. On the Nature of the Medium Lifetime Component of Positron Annihilation in a Teflon Polymer. *Chinese Physics C* **14,** 11. http://inis.iaea.org/search/search.aspx?orig_q=RN:22039665 (1990).

[136] Kerr, D. P. Positron Annihilation in Teflon and Polyethylene. *Canadian Journal of Physics* **52,** 935–939. https://doi.org/10.1139/p74-127 (1974).

[137] Hill, A. J. & Agrawal, C. M. Positron lifetime spectroscopy characterization of thermal history effects on polycarbonate. *Journal of Materials Science* **25,** 5036–5042. https://doi.org/10.1007/BF00580127 (1990).

[138] Kluin, J. E., Yu, Z., Vleeshouwers, S., McGervey, J. D., Jamieson, A. M. & Simha, R. Temperature and time dependence of free volume in bisphenol A polycarbonate studied by positron lifetime spectroscopy. *Macromolecules* **25,** 5089–5093. https://doi.org/10.1021/ma00045a040 (1992).

[139] Kluin, J., Yu, Z., Vleeshouwers, S., McGervey, J., Jamieson, A., Simha, R. & Sommer, K. Orthopositronium lifetime studies of free volume in polycarbonates of different structures: influence of hole size distributions. English. *Macromolecules* **26,** 1853–1861. https://doi.org/10.1021/ma00060a010 (1993).

[140] Bohlen, J. & Kirchheim, R. Macroscopic Volume Changes versus Changes of Free Volume As Determined by Positron Annihilation Spectroscopy for Polycarbonate and Polystyrene. *Macromolecules* **34,** 4210–4215. https://doi.org/10.1021/ma001297o (2001).

[141] Dlubek, G., Clarke, A., Fretwell, H., Dugdale, S. & Alam, M. Positron lifetime studies of free volume hole size distribution in amorphous and in semi-crystalline polymers. *Journal of Radioanalytical and Nuclear Chemistry* **211,** 69–76. https://doi.org/10.1007/bf02036257 (1996).

[142] Campillo Robles, J. & Plazaola, F. Collection of Data on Positron Lifetimes and Vacancy Formation Energies of the Elements of the Periodic Table. *Defect and Diffusion Forum* **213-215,** 141. https://doi.org/10.4028/www.scientific.net/DDF.213-215.141 (2003).

[143] Sterne, P. A. & Kaiser, J. H. First-principles calculation of positron lifetimes in solids. *Phys. Rev. B* **43,** 13892–13898. https://doi.org/10.1103/PhysRevB.43.13892 (17 1991).

[144] Dlubek, G., Buchhold, R., Hübner, C. & Nakladal, A. Water in Local Free Volumes of Polyimides: A Positron Lifetime Study. *Macromolecules* **32,** 2348–2355. https://doi.org/10.1021/ma981381s (1999).

[145] Sharma, S. C., Hozhabri, N., Hyer, R. G., Hossain, T., Kim, S., Meyer, F. O., Pas, M. & Stephens, A. E. A Study of Defects in Czochralski-Grown Silicon by Positron Annihilation Spectroscopy. *MRS Proceedings* **262,** 45. https://doi.org/10.1557/PROC-262-45 (1992).

[146] Britton, D. T., Willutzki, P., Jackman, T. E. & Mascher, P. Positron lifetime studies of defects in MBE-grown silicon. *Journal of Physics: Condensed Matter* **4,** 8511–8518. https://doi.org/10.1088/0953-8984/4/44/012 (1992).

[147] Giebel, D. & Kansy, J. *A New Version of LT Program for Positron Lifetime Spectra Analysis* in *Progress in Positron Annihilation* **666** (Trans Tech Publications Ltd, 2011), 138–141. https://doi.org/10.4028/www.scientific.net/MSF.666.138.

[148] Krause-Rehberg, R. & Leipner, H. *Positron annihilation in semiconductors : defect studies* in (Springer-Verlag Berlin Heidelberg, Germany, 1999), 15. https://www.springer.com/gp/book/9783540643715.

[149] Mackie, R. A., Singh, S., Laverock, J., Dugdale, S. B. & Keeble, D. J. Vacancy defect positron lifetimes in strontium titanate. *Physical Review B* **79,** 014102. http://dx.doi.org/10.1103/PhysRevB.79.014102 (2009).

[150] Kanda, G. & Keeble, D. Positron annihilation lifetime spectroscopy source correction determination: A simulation study. *Nuclear Instruments and Methods in Physics Research Section A Accelerators Spectrometers Detectors and Associated Equipment* **808,** 54–59. http://dx.doi.org/10.1016/j.nima.2015.11.052 (2016).

[151] Dauwe, C., Waeyenberge, B., Consolati, G., Kansy, J., Segers, D., Van Hoecke, T. & Du Prez, F. Thermalisation of Positronium in Polymers. *Materials Science Forum* **255-257,** 62. 10.4028/www.scientific.net/MSF.255-257.62 (1997).

[152] Kanda, G. S., Ravelli, L., Löwe, B., Egger, W. & Keeble, D. J. Positron annihilation lifetime spectroscopy study of Kapton thin foils. *Journal of Physics D Applied Physics* **49,** 025305. http://dx.doi.org/10.1088/0022-3727/49/2/025305 (2016).

[153] Kansy, J. & Suzuki, T. A non-conventional method of polymer PAL spectrum analysis by the LT computer program. *Radiation Physics and Chemistry* **76.** Proceedings of the 8th International Workshop on Positron and Positronium Chemistry, 291–296. https://doi.org/10.1016/j.radphyschem.2006.03.052 (2007).

[154] Płotkowski, K., Panek, T. J. & Kansy, J. Positron implantation profile in kapton. *Il Nuovo Cimento D* **10,** 933–940. https://doi.org/10.1007/BF02450195 (1988).

[155] Kansy, J. & Ziąbka, M. *Positron Irradiation Effects in HDPE during PAL Measurement at Ambient Temperature* in *Positron and Positronium Chemistry X* **733** (Trans Tech Publications Ltd, 2013), 143–146. https://doi.org/10.4028/www.scientific.net/MSF.733.143.

[156] Dlubek, G. *Local Free-Volume Distribution from PALS and Dynamics of Polymers* in *Polymer Physics* 421–472 (John Wiley & Sons, Ltd, 2010). ISBN: 9780470600160. https://doi.org/10.1002/9780470600160.ch11.

[157] Hidalgo, C., González-Doncel, G., Linderoth, S. & San Juan, J. Structure of dislocations in Al and Fe as studied by positron-annihilation spectroscopy. *Phys. Rev. B* **45,** 7017–7021. https://link.aps.org/doi/10.1103/PhysRevB.45.7017 (13 1992).

Appendix A

Gamma spectroscopy

A typical gamma spectrum resultant from the decay of a radionuclide, containing the most commonly observed features, under the assumption that only one photon at a time enters the detector, is shown in *Figure A.1*.

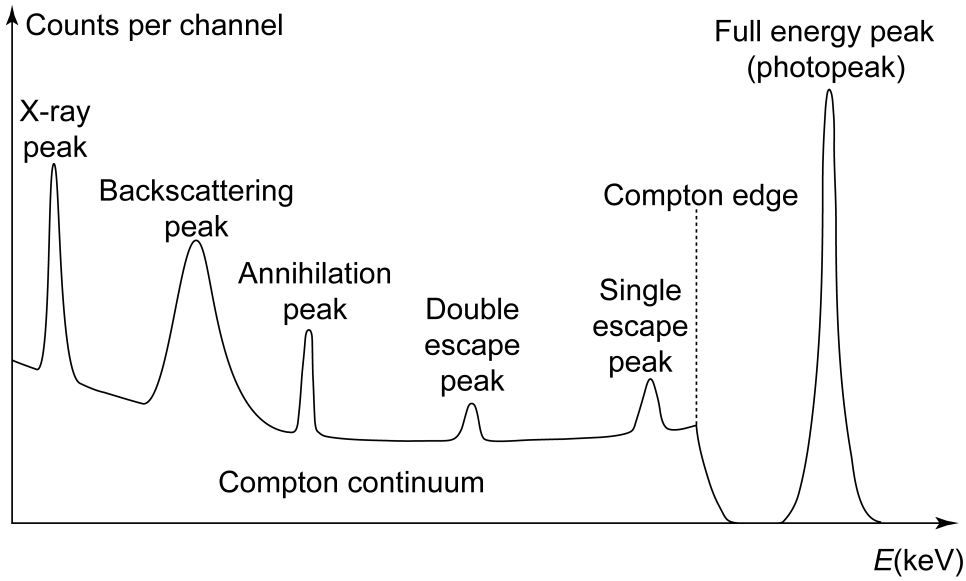

Figure A.1: Representation of a typical gamma spectrum produced in gamma spectroscopy experiments, where "Counts per channel" in the Y axis represents the number of detected photons whose energy lies between the energy range defined for each channel in the X axis. Adapted from [133].

When a photon enters a scintillator, it interacts with its medium through the processes reviewed in *Section 2.1*, with the possibility of generating secondary electrons as a result. The actions partaken not only by the original photon but also by the resultant secondary electrons culminate in the deposition of either the entirety or different fractions of the photon's original energy, which will then be absorbed by the scintillator material and re-emitted in the form of a photon in the visible range, giving rise to the different features displayed in the gamma spectrum. The specific course of action that is at the origin of each feature is thus discussed below:

★ **Compton continuum:** When a γ-ray suffers one or multiple Compton scatterings, a portion of

its energy, which is dependent on the scattering angle, is transferred to one or multiple electrons. Supposing that this γ-ray then leaves the detector, only the energy transferred to the electrons is deposited on the detector and contributes to the gamma spectrum, meaning that part of the initial photon's energy is lost. Because scatterings in all angles are likely to occur in the detector, a continuous spectrum of energies can be transferred to the electron(s), ranging from zero up to a certain maximum, meaning that a continuum of energies is deposited in the detector, therefore giving rise to what is known as the Compton continuum.

★ **Compton edge:** The maximum energy that can be transferred from a photon to an electron in a single Compton scattering happens on a head-on collision, which corresponds to a scattering angle of 180^{o}. So, if it is the case that a photon suffers a head-on collision with an electron followed by an escape from the detector, then this electron will deposit in the detector this maximum energy that corresponds to the limit of the Compton continuum, otherwise called the Compton edge.

★ **Full energy peak or Photopeak:** When a photon enters a detector and undergoes a photoelectric interaction, it generates a photoelectron that is promptly emitted, creating, as a result, a vacancy in the electron shell of the atom. This vacancy is swiftly filled either through the capture of a free electron from the medium or through the electron rearrangement in the atom shells. In the second case, the binding energy of the initial electron in its original shell is released either in the form of a Auger electron or a characteristic X-ray. Both the Auger electron and the X-ray will deposit their energy on the detector as the latter is also absorbed by photoelectric interactions with less tightly bound electrons. Thus, the original photoelectric absorption not only produces a photoelectron which carries off most of the gamma-ray energy but also a subsequent set of lower energy electrons to which the binding energy of the previous photoelectron is transferred. In conclusion, the sum of the kinetic energies of the emitted electrons equals the energy of the original gamma-ray photon, which is totally deposited in the detector, giving rise to the photopeak.

Nevertheless, a simple photoelectric interaction is not the only process to contribute to the full energy peak. In fact, if a photon experiences one or multiple Compton scatterings and thereafter, instead of leaving the detector, is absorbed via photoelectric effect, its entire energy is deposited in the detector. As well as that, in the event that a photon is involved in a pair production process, after which the created electron deposits its energy and the resulting positron annihilates in the detector, generating two annihilation γ-rays that do not flee the detector but instead suffer Compton scatterings and subsequent photoelectric effect, as described just now, there is also a total deposition of the original γ-ray's energy.

★ **Single escape peak:** On the other hand, it may happen that when a γ-ray of sufficient energy undergoes pair production and the resulting positron annihilates in the detector, generating two annihilation γ-rays, one of them escapes the detector. In that case, an energy equal to 511 keV is lost and, as a consequence, a peak, named the single escape peak, of lower energy than the photopeak, will appear in the gamma spectrum, given that the energy deposited in the detector is only the energy of the initial gamma photon minus 511 keV.

★ **Double escape peak:** Another possible scenario is that, after the annihilation of the positron resultant from the pair production process initialised by a γ-ray, both annihilation photons flee the detector, meaning an energy of 1022 keV is lost. This situation gives rise to a peak in the spectrum, known as the double escape peak, of even lower energy than the single escape peak, since now the energy deposited in the detector is only the energy of the original γ photon reduced by 1022 keV.

★ **Backscattering peak:** Besides interacting with the detector, a photon may also interact with the surrounding medium before entering the detector, in particular with the materials adjacent to the detector. For instance, it may happen that a photon suffers Compton scattering with one of the electrons in the surrounding media, in which case it will transfer some of its energy to the electron before scattering back to the detector, where its energy will be deposited by photoelectric effect. The amount of energy lost in the interaction is dependent upon the scattering angle, although for angles greater than about 110-120$^{\mathrm{o}}$, the scattered photons are of nearly identical energy. Therefore, rather that a large energy spectrum as was the case for the Compton continuum, a somewhat broad peak, the backscattering peak, will appear in the recorded gamma spectrum instead.

★ **X-ray peak:** Apart from scattering, it is also likely that photons experience the process of photoelectric absorption in the materials immediately surrounding the detector, which, as has been previously pointed out, can lead to the generation of X-rays. Due to the noticeable distance travelled by them, the generated X-rays can easily penetrate the detector, where they will be absorbed in more photoelectric interactions and deposit their characteristic material dependent energy, prompting, in the process, the appearance of the very low energy X-ray peak.

X-rays can also be produced in the decay of a radioisotope if processes like electronic capture or internal conversion are part of its decay mode, in which case, the emitted X-rays will be absorbed in the detector through the photoelectric effect and the entirety of their energy will be deposited, giving rise to an X-ray peak in the low energy range of the spectrum.

★ **Annihilation peak:** It is also feasible that photons undergo pair production in neighbouring, and especially in high-Z, materials, followed by the subsequent annihilation of the formed positron. From this annihilation, there is a high probability that one of the produced 511 keV photons enters the detector, where it will partake in photoelectric interactions and deposit its energy, resulting in the rise of the annihilation peak, centred around the energy of 511 keV.

An additional contribution to the annihilation peak concerns the energy deposition of 511 keV photons, resultant from the annihilation not of positrons formed during pair production reactions, but instead emitted by the radioactive sources that contain a β^+ decay branch in their decay scheme, as is the case of the ^{22}Na source used in this work.

Appendix B

Positron lifetime values reported in literature

τ_1 (ns)	I_1 (%)	τ_2 (ns)	I_2 (%)	τ_3 (ns)	I_3 (%)	τ_4 (ns)	I_4 (%)	Reference
0.422	74.2	3.307	26.3	-	-	-	-	[134]
0.32	72.63	0.93	11.4	3.89	15.97	-	-	[132]
0.25	50.32	0.747	25.98	3.931	23.7	-	-	[117]
0.126	18.85	0.384	47.14	1.399	12.94	4.225	21.07	
0.117	19	0.353	48.83	1.417	13.9	4.272	18.43	[135]
0.23	20.8	0.39	47.3	1.23	17.5	4.33	14.4	[136]

Table B.1: Experimentally obtained lifetime values reported in literature for Commercial Teflon.

τ_1 (ns)	I_1 (%)	τ_2 (ns)	I_2 (%)	τ_3 (ns)	I_3 (%)	Reference
-	-	-	-	2.05-2.2	18-36	[100]
-	-	-	-	2.09	26.6	[137]
-	-	-	-	2.12	27.4	
0.125	-	0.4	-	2.14	28.5	[107]
0.22	38-49	0.5-0.62	20-31	2.03-2.13	27.5-29	[138]
0.12-0.28	19-21	0.35-0.45	39-45	2.05-2.08	28-34	[139]
0.19	23	0.41	46	2.05	30	[140]
0.231	42.6	0.495	27.5	2.032	29.9	[141]
0.242	42.8	0.47	26.8	2.014	30.5	

Table B.2: Published positron lifetime values for Polycarbonate.

Samples	Ag	Al			Au	Cd	Cu		Fe	Ge
Lifetimes (ps)	119 [123]	156 [124]	162.5 [142]	164.9 [119]	113 [142]	184 [142]	103 [123]	119 [142]	104 [81]	228 [142]
	120 [142]	158 [142]	162.8 [86]	165 [142]	113 [142]	185 [126]	106 [86]	120 [80]	104 [123]	228 [142]
	130 [142]	158 [86]	163 [119]	165 [142]	117 [142]	187 [92]	110 [118]	120 [142]	106 [142]	230 [142]
	130 [86]	158 [123]	163 [142]	165 [142]	117 [143]	190 [126]	110 [142]	120 [86]	106 [143]	230 [142]
	130 [86]	159 [142]	163 [142]	165 [126]	118 [92]		110 [126]	120 [14]	106 [81]	230 [142]
	131 [142]	159 [86]	163 [142]	166 [92]			110.7 [142]	120.6 [119]	106 [95]	230 [142]
	131 [143]	160 [142]	163 [142]	166 [142]			111 [123]	121 [126]	107 [92]	231 [126]
	131 [123]	160 [123]	163 [142]	166 [142]			112 [123]	121.8 [119]	108 [142]	
	135 [86]	160.3 [119]	163 [142]	166 [86]			112 [81]	122 [92]	108 [142]	
	135 [123]	160.7 [142]	163 [126]	170 [142]			113 [86]	122 [118]	108.1 [95]	
	137 [142]	161 [124]	164 [142]	171 [123]			114.5 [86]	122 [86]	110 [142]	
	138 [92]	161 [113]	164.1 [142]	180 [144]			114.5 [81]	124 [86]	110 [142]	
	138 [142]	162 [124]	164.5 [142]	195 [110]			115 [118]	128 [14]	110 [142]	
	140 [142]	162 [142]					115 [118]		111 [142]	
	142 [86]								112 [142]	
	164 [124]								114 [142]	
	165 [124]								115 [142]	
	167 [124]								117 [142]	
Average lifetime (ps)	137.94	164.10			115.60	186.50	116.19		109.01	229.57
Standard deviation (ps)	13.56	6.56			2.15	2.29	5.92		3.60	1.05

Samples	In	Mg	Mo	Nb	Ni		Pb	Pt	Sb	EG-Si
Lifetimes (ps)	180 [124]	220 [142]	103 [142]	112 [142]	94 [86]	108 [81]	194 [119]	99 [142]	214 [142]	175 [145]
	184 [124]	224 [126]	103 [143]	118 [142]	94 [123]	108 [81]	194 [126]	99 [142]	215 [142]	178 [18]
	184 [124]	225 [142]	104 [142]	119 [142]	95 [80]	109.8 [142]	200 [142]	99 [143]	269 [142]	185 [146]
	189 [124]	225 [142]	109.5 [142]	119 [143]	102 [86]	110 [92]	200 [142]			
	191 [126]	225 [142]	114 [142]	120 [142]	103 [123]	110 [119]	202.5 [119]			
	192 [80]	225 [126]	118 [142]	120 [86]	104.3 [142]	110 [124]	204 [142]			
	193 [142]		121 [92]	120 [86]	105 [142]	110 [142]	205 [124]			
	193 [126]		123 [81]	122 [142]	105 [86]	110 [86]	206 [124]			
	194.7 [142]			122 [142]	106.8 [119]	110 [86]	207 [124]			
	196 [126]			122 [142]	107 [142]	110 [81]	207 [126]			
	196 [126]			123 [86]	108 [124]	110 [123]				
	197 [147]			128 [86]	108 [124]	116 [142]				
	197 [142]			128.3 [86]	108 [86]	120 [110]				
	200 [142]			133 [124]						
	220 [142]			137 [124]						
				138 [124]						
Average lifetime (ps)	193.78	224.00	111.94	123.83	106.96		201.95	99.00	232.67	179.33
Standard deviation (ps)	8.85	1.83	7.70	6.94	5.91		4.64	0	25.70	4.19

Samples	Si		Sn		Ta	Ti	V	W	Zn	Zr
Lifetimes (ps)	213 [142]	219 [147]	191 [120]	196.3 [120]	113 [92]	143 [142]	120 [142]	101 [112]	145 [142]	163 [124]
	216 [142]	219 [144]	191.5 [120]	196.9 [120]	116 [142]	145 [142]	123 [142]	102 [142]	152 [142]	163 [142]
	217 [142]	219 [111]	191.9 [120]	197 [120]	116 [143]	147 [143]	130 [142]	105 [142]	153 [142]	165 [92]
	217.9 [142]	219.1 [122]	191.9 [120]	199 [80]	117 [142]	147 [126]	130 [143]	105 [143]	153 [142]	165 [142]
	218 [80]	220 [118]	192.6 [120]	201 [92]	120 [142]	149 [126]	133 [142]	163 [124]	154 [142]	165 [143]
	218 [148]	221 [142]	193.7 [120]	201 [142]	122 [142]	152 [142]		166 [124]	156 [126]	167 [124]
	218 [121]	221 [142]	194 [120]	201 [126]	122 [142]	154 [142]		168 [124]	160 [92]	167 [124]
	218 [142]	222 [142]	194.3 [120]	202 [147]	125 [142]	172 [124]			175 [126]	173 [142]
	218.3 [122]	222 [142]	194.6 [120]	230 [142]	155 [124]	173 [124]				181 [142]
	218.3 [122]	223 [142]	195 [126]		158 [124]	176 [124]				
					160 [124]					
Average lifetime (ps)	218.88		197.62		129.45	155.80	127.20	130.00	156.00	167.67
Standard deviation (ps)	2.21		8.38		17.60	12.11	4.87	30.95	8.19	5.50

Table B.3: Reported bulk lifetime values for the most commonly studied metals and semiconductors.

τ_1 (ps)	I_1 (%)	τ_2 (ps)	I_2 (%)	References
362.8	-	-	-	[48]
370	-	-	-	[121]
373.8	100	-	-	[122]
373.8	100	-	-	
374.2	100	-	-	
374.7	100	-	-	
382	-			
380	-	-	-	[149]
380	-	-	-	[120]
380	-	-	-	[141]
381	-	-	-	[150]
381	-	-	-	[86]
387	99.8	-	-	
382	-	-	-	[92]
382	-	-	-	[151]
382	100	-	-	[126]
382	100	-	-	[118]
385	-	-	-	[131]
385	-	-	-	[124]
385	100	-	-	[152]
385	99.3	-	-	
386	-	-	-	[129]
386	-	-	-	[153]
386	-	-	-	[115]
386	100	-	-	[154]
393	-	-	-	[29]
412	-	-	-	[125]
367.6	-	-	-	[119]
373.3	-	-	-	
229	12	378	87.4	
135	64	361	36	[16]
144	44.1	378	50.8	
152.2	45.8	371.0	54.2	[80]
163	36.6	372	62.5	[155]

Table B.4: Reported positron lifetimes obtained for Kapton® HN.

τ_1 (ps)	References
336	[123]
345	
352	
356	
364	
380	[156]
380	[144]
386	[147]
415	[126]
430	[124]
430	[110]
450	[157]

Table B.5: Published positron lifetime values for $^{22}NaCl$.

Appendix C

Routine's scripts

Routine for shifting and adding lifetime spectra

This routine was written for the proper summation of lifetime spectra, from files outputted by the PALS spectrometer's software MAESTRO, into one lifetime spectrum with the intended number of counts, outputted in the only file format accepted by the PALSfit3 software. This proper summation eliminates the influence of the spectrometer's zero channel drift in the final lifetime spectrum.

Get the lifetime data from the spectra

In this section, the routine extracts the lifetime data (channel, lifetime) from each lifetime spectra under analysis.

Note: In the following line, the folder where the spectra under analysis are stored must be indicated.

```
files = FileNames["*.Spe", "<drive>:\\<path to folder>\\<folder>"]
        nomes de arquivos
```

Note: In the following line, the second number should be equal to 15 plus the number of ROIs (Regions of Interest) with which the spectra have been acquired.

```
data = Import[#, "List", HeaderLines → 13][[ ;; -16]] & /@ files;
       importa          lista      linhas de cabeçalho
NumberofSpectra = Length[data] + 1
                  comprimento
```

Check if there was a zero channel shift

In this section, the routine prints the zero channel of each spectrum so that the user can compare the different zero channels and check if there was any zero channel drift during the measurement.

```
For[i = 1, i < NumberofSpectra, i++,
para cada
 Print[First[First[Position[data[[i]], Max[data[[i]]]]]]]]
 escreve prime··· prime··· posição          máximo
```

Shift the spectra

In this section, the routine shifts all the spectra in order to align the zero channel of all spectra. To do this, the routine determines the lowest zero channel out of the zero channels of all the spectra, after which all the spectra are shifted by a number of channels corresponding to the difference between their own zero channel and the selected one.

Determine the lowest zero channel number

```
MinimumZeroChannel = 4096;
For[i = 1, i < NumberofSpectra, i++,
 If[First[First[Position[data[[i]], Max[data[[i]]]]]] < MinimumZeroChannel,
  MinimumZeroChannel = First[First[Position[data[[i]], Max[data[[i]]]]]],
  MinimumZeroChannel = MinimumZeroChannel]]
MinimumZeroChannel
```

Shift all the spectra to align all the zero channels with the lowest zero channel number

```
For[i = 1, i < NumberofSpectra, i++, data[[i]] = RotateRight[data[[i]],
    MinimumZeroChannel - First[Position[data[[i]], Max[data[[i]]]]]]]
```

Add the spectra

In this section, the routine adds the content of all the bins of all the spectra into the corresponding bin to obtain a final spectrum with the intended larger number of counts.

```
Finaldata = 0;
For[i = 1, i < NumberofSpectra, i++, Finaldata = Finaldata + data[[i]]]
```

Check if everything is correct

In this section, the routine checks if the spectra have been adequately summed by searching for the total number of counts and the zero channel of the final spectrum. If everything was done correctly, the number of counts in the final spectrum should be equal to the sum of the number of counts of all the spectra and the zero channel of the final spectrum should be the lowest registered zero channel.

```
Totalmax = 0;
For[i = 1, i < NumberofSpectra, i++, Totalmax = Totalmax + Max[data[[i]]]]
Totalmax
Max[Finaldata]
```

Note: If everything was done correctly, the values of Totalmax (sum of the number of counts of all the spectra) and Max[Finaldata] (number of counts in the final spectrum) should be the same.

```
Position[Finaldata, Max[Finaldata]]
posição  máximo
```

Note: If everything was done correctly, the value of Position[Finaldata,Max[Finaldata]] (zero channel of the final spectrum) should be the lowest zero channel out of all the zero channels, which can be checked in the “Check if there was a zero channel shift” section.

Export the final spectrum

In this section, the routine exports the final spectrum to a .dat file, which is the only file format accepted by PALSfit3.

```
Finaldata2 = ArrayReshape[Finaldata, {410, 10}];
             redimensionamento de arranjo
```

Note: In the following line, the name of the file in which the final spectrum is to be stored and the folder where the file is to be stored must be indicated.

```
file = OpenAppend["<drive>:\\<path to folder>\\<folder>\<file name>"];
       abre arquivo para anexar
```

Note: In the following line, the desired name for the spectrum to be read by PALSfit3 must be indicated.

```
Write[file, "<spectrum name>"]
escreve
Export[file, Finaldata2, "Table"]
exporta  tabela
Close[file];
fecha
```

Figure C.1: Mathematica script, for the shifting and proper summation of lifetime spectra.

```
REM This JOB file was written for the PALS spectrometer's acquisition software MAESTRO with
instructions for the successive collection of many lifetime spectra without the user's
intervention. The file orders the spectrometer to acquire n spectra, with n stipulated by
the user, each for a period of time of t seconds, t also specified by the user, and then
save them in a folder indicated by the user, in a .Spe file, each with a name defined by the
order in which they were acquired
SET_PRESET_CLEAR
REM The number in the following line must be changed to the number of real time seconds for
which each spectrum is desired to be acquired
SET_PRESET_REAl 10
REM The number in the following line must be changed to the number of spectra desired to be
acquired
LOOP 2
CLEAR
START
WAIT
REM In the following line, the name of the folder where the spectra will be stored must be
changed to the desired folder. Note that the ??? in the spectrum's file name is the loop
count value, indicating the order in which each spectrum was acquired
SAVE "C:\User\20210122\Spectrum???.Spe"
END_LOOP
```

Figure C.2: JOB file script, for the spectrometer’s acquisition software MAESTRO for the successive collection of many spectra without the user’s assistance.

```
/*****************************************************************************
* This routine was written to determine the system's time resolution function, *
* through the fitting of a user provided Co-60 spectrum to a Gaussian function *
*****************************************************************************/

#include<iostream>
#include<string>
using namespace std;

void Fit_gauss(){

  /*Section to establish the graph, the canvas and the histogram with data*/
  //In the following line, the folder and the .txt file where the spectrum under analysis is
  stored must be indicated
  TGraphErrors *graph = new TGraphErrors("<folder name>/<file name>","%lg %lg %lg %lg");
   //In the following line, the desired name for the canvas must be indicated in the second
   parameter inside the parentheses
  TCanvas *canvas = new TCanvas("canvas"," Gaussian fitting",300,10,700,500);
  //In the following line, the following numbers must be provided inside theparentheses in
  this order: number of desired bins in the x axis, desired lower bound limit in the x axis,
  desired upper bound limit in the x axis, number of desired bins in the y axis, desired
  lower bound limit in the y axis, desired upper bound limit in the y axis
  TH2F *hist = new TH2F("hist","",300,1400,1700,100,0,20000);


  /*Section to define the histogram style*/
  //In the following line, the desired title for the histogram must be indicated
  hist->SetTitle("Co60");
  hist->SetXTitle("Channel");
  hist->SetYTitle("Counts");
  hist->GetYaxis()->SetTitleFont(30);
  hist->GetYaxis()->SetTitleSize(0.04);
  hist->GetXaxis()->SetTitleFont(30);
  hist->GetXaxis()->SetTitleSize(0.04);


  /*Section to define the graph style*/
  gStyle->SetOptStat(0);
  gStyle->SetOptFit(0);
  hist->Draw();
  graph->SetName("graph");
  graph->SetMarkerColor(kViolet-6);
  graph->SetMarkerStyle(29);
  graph->SetMarkerSize(1.2);
  graph->Draw("P");


  /*Section to establish the fit function - a Gaussian function defined with 3 fitting
  parameters (p0,p1,p2) as f(x) = p0*exp(-1/2*((x-p1)/p2)^2)*/
  TF1 *f1 = new TF1("f1", "gaus(0)", 0,5000);
  f1->SetLineColor(kBlue+2);
  f1->SetLineWidth(3);


  /*Section to define the initial values for the fitting parameters of the fit function */
  //In the following line, the initial parameter for the parameter p0 must be indicated
  f1->SetParameter(0,1500);
  //In the following line, the initial parameter for the parameter p1 must be indicated
  f1->SetParameter(1,10000);
  //In the following line, the initial parameter for the parameter p2 must be indicated
  f1->SetParameter(2,7);


  /*Section to define the lower and upper bound limits for the fitting parameters of the fit
  function */
  //In the following line, the lower and upper bound limits for the parameter p0 must be
  indicated, the first and second numbers, respectively
  f1->SetParLimits(0,100,20000);
  //In the following line, the lower and upper bound limits for the parameter p1 must be
  indicated, the first and second numbers, respectively
  f1->SetParLimits(1,1400,1700);
```

```
    //In the following line, the lower and upper bound limits for the parameter p2 must be
    indicated, the first and second numbers, respectively
    f1->SetParLimits(2,2,20);


    /*Section to define the fit options*/
    //In the following line, the fit range must be defined, by defining the lower and upper
    bound limits, the first and second numbers, respectively
    graph->Fit(f1,"", "", 1470,1630);
    f1->Draw("same");
    //The following line must be uncommented if it is desired that the y axis is presented in
    the logarithmic scale
    //canvas->SetLogy();


    /*Section to define the legend options*/
    TLegend* legend = new TLegend(0.1,0.7,0.48,0.9);
    legend->AddEntry("graph", "Data", "p");
    legend->AddEntry("f1","Fit function","l");
    legend->Draw();
    canvas->Update();

}
```

Figure C.3: C++ script, containing functions from the ROOT library, for determination of the system's time resolution through the fitting of a ^{60}Co spectrum to a gaussian function.

```
/*****************************************************************************
* This routine was written to determine the system's time resolution function, *
* through the fitting of a user provided Co-60 spectrum to an Exponential Sided*
* Gaussian (ESG) function                                                     *
*****************************************************************************/

#include<iostream>
#include<string>
using namespace std;

void Fit_gauss_exp(){

  /*Section to establish the graph, the canvas and the histogram with data*/
  //In the following line, the folder and the .txt file where the spectrum under analysis is
  stored must be indicated
  TGraphErrors *graph = new TGraphErrors("<folder name>/<file name>","%lg %lg %lg %lg");
   //In the following line, the desired name for the canvas must be indicated in the second
   parameter inside the parentheses
  TCanvas *canvas = new TCanvas("canvas"," Gaussian fitting",300,10,700,500);
  //In the following line, the following numbers must be provided inside theparentheses in
  this order: number of desired bins in the x axis, desired lower bound limit in the x axis,
  desired upper bound limit in the x axis, number of desired bins in the y axis, desired
  lower bound limit in the y axis, desired upper bound limit in the y axis
  TH2F *hist = new TH2F("hist","",70,1560,1625,1000,0,2300);


  /*Section to define the histogram style*/
  //In the following line, the desired title for the histogram must be indicated
  hist->SetTitle("Co60");
  hist->SetXTitle("Channel");
  hist->SetYTitle("Counts");
  hist->GetYaxis()->SetTitleFont(30);
  hist->GetYaxis()->SetTitleSize(0.04);
  hist->GetXaxis()->SetTitleFont(30);
  hist->GetXaxis()->SetTitleSize(0.04);


  /*Section to define the graph style*/
  gStyle->SetOptStat(0);
  gStyle->SetOptFit(0);
  hist->Draw();
  graph->SetName("graph");
  graph->SetMarkerColor(kViolet-1);
  graph->SetMarkerStyle(21);
  graph->SetMarkerSize(0.8);
  graph->Draw("P");


  /*Section to establish the fit function - a Exponential Sided Gaussian function (a
  Gaussian function with exponential tails) */
  TF1 *f1 = new TF1("f1", "(x<=int([1]-[0]*[2]))*[3]*exp([0]^2/2+[0]*(x-[1])/[2]) + \
                           (x>int([1]-[0]*[2]) &&
                           x<=int(-[4]*[2]+[1]))*[3]*exp(-0.5*((x-[1])/[2])^2) +\
(x>int(-[4]*[2]+[1]))*[3]*exp([4]^2/2+[4]*(x-[1])/[2])", 1800,1870);
  f1->SetLineColor(kBlue+3);
  f1->SetLineWidth(2);


  /*Section to define the initial values for the fitting parameters of the fit function */
  //In the following line, the initial parameter for the parameter p0 must be indicated
  f1->SetParameter(0,2);
   //In the following line, the initial parameter for the parameter p1 must be indicated
  f1->SetParameter(1,1590);
   //In the following line, the initial parameter for the parameter p2 must be indicated
  f1->SetParameter(2,7);
   //In the following line, the initial parameter for the parameter p3 must be indicated
  f1->SetParameter(3,3000);
   //In the following line, the initial parameter for the parameter p4 must be indicated
  f1->SetParameter(4,-2);
```

```
    /*Section to define the lower and upper bound limits for the fitting parameters of the fit
    function */
    //In the following line, the lower and upper bound limits for the parameter p0 must be
    indicated, the first and second numbers, respectively
    f1->SetParLimits(0,0,10);
    //In the following line, the lower and upper bound limits for the parameter p1 must be
    indicated, the first and second numbers, respectively
    f1->SetParLimits(1,1500,1700);
    //In the following line, the lower and upper bound limits for the parameter p2 must be
    indicated, the first and second numbers, respectively
    f1->SetParLimits(2,1,30);
    //In the following line, the lower and upper bound limits for the parameter p3 must be
    indicated, the first and second numbers, respectively
    f1->SetParLimits(3,-1,20000);
    //In the following line, the lower and upper bound limits for the parameter p4 must be
    indicated, the first and second numbers, respectively
    f1->SetParLimits(4,-10,0);


    /*Section to define the fit options*/
    //In the following line, the fit range must be defined, by defining the lower and upper
    bound limits, the first and second numbers, respectively
    graph->Fit(f1, "", "", 1565,1620);
    f1->Draw("same");
    //The following line must be uncommented if it is desired that the y axis is presented in
    the logarithmic scale
    //canvas->SetLogy();


    /*Section to define the legend options*/
    TLegend* legend = new TLegend(0.1,0.7,0.48,0.9);
    legend->SetTextFont(12);
    legend->AddEntry("graph", "Data", "p");
    legend->AddEntry("f1","Fit function","l");
    legend->Draw();

    canvas->Update();

}
```

Figure C.4: C++ script, containing functions from the ROOT library, for determination of the system's time resolution through the fitting of a ^{60}Co spectrum to an ESG function.

Routine for the free volumes' size estimation

This routine was written for the estimation of the size of the free volumes inside a sample given the o-Ps lifetimes obtained from the analysis of their lifetime spectra, according to theoretical models designed to correlate the free volumes' size with the observed lifetime of the o-Ps atoms. The only information that the user is required to provide is the obtained o-Ps lifetime from the spectra analysis in ns, in the parameter Tau in the "Data" section and an estimate for the free volume's radiius in nm, in the parameter FirstEstimate in the "Data" section. The script is then runin its entirety and the final free volumes' size results are presented in a table at the end of the script.

Data

```
Tau = 1;
FirstEstimate = 0.5;
```

Parameters

```
LambdapPs = 1 / 0.125;
LambdaoPs = 1 / 142;
LambdaA = (LambdapPs + LambdaoPs * 3) / 4;
Delta = 0.1656;
Ra = 0.8;
b = 0.55;
Delta2 = 0.18;
Betavar = 0.188;
T = 295.15;
Kappa = 8.6173324 * 10^-5;
Dvalue = Exp[-2];
         exponencial
vthPA = 0.021;
Delta3 = 0.38;
Lvalue = 1.28;
```

Theoretical models for free volume size estimation

Tao-Eldrup Model

Radius

```
R1 = R1 /. FindRoot[
          encontra raiz
     (LambdaA (1 - R1 / (R1 + Delta) + 1 / (2 Pi) * Sin[2 Pi * R1 / (R1 + Delta)]))^{-1} == Tau,
                                                  nú··· seno número pi
     {R1, FirstEstimate}];
```

Mean free path

```
L1 = 4 * R1 / 3;
```

Tokyo Model

Radius

```
Piecefunction1[x_] := Piecewise[
                      função por partes
  {{( LambdaA * (1 - x / (x + Delta) + 1 / (2 Pi) * Sin[2 Pi * x / (x + Delta)]) + LambdaoPs)^
                                                  nú··· seno número pi
     {-1}, x < Ra},
   {( LambdaA * (1 - Ra / (Ra + Delta) + 1 / (2 Pi) * Sin[2 Pi * Ra / (Ra + Delta)]) *
                                                  nú··· seno número pi
        (1 - ((x - Ra) / (x + Delta))^b) + LambdaoPs)^{-1} , x >= Ra}}]

R2 = R2 /. FindRoot[Piecefunction1[R2] == Tau, {R2, FirstEstimate}];
          encontra raiz
```

Mean free path

```
L2 = 4 * R2 / 3;
```

Rectangular Tao-Eldrup Model

Cube side

```
R3 = R3 /.
    FindRoot[(LambdaA - (LambdapPs - LambdaoPs) / 4 * (1 - 2 * Delta2 / R3 + Sum[1 / (i * Pi) *
      Sin[2 i * Pi * Delta2 / R3] * Exp[-Betavar * i^2 / (R3^2 * Kappa * T)],
     {i, 1, 100000}] / Sum[Exp[-Betavar * i^2 / (R3^2 * Kappa * T)],
     {i, 1, Infinity}])^3)^-1 == Tau, {R3, FirstEstimate}];
```

Mean free path

```
L3 = 2 * R3 / 3;
```

Hybrid Model

Functions

```
Pickoff[x_] :=
 LambdaA * (3 * Dvalue / (1 + Dvalue)) * (Delta / (x + Delta)) * (x / (x + Delta))^2
Tao[x_] := LambdaA * (1 - x / (x + Delta) + 1 / (2 Pi) * Sin[2 Pi * x / (x + Delta)])
```

Radius

```
R4 = x /. FindRoot[(((Sqrt[Pickoff[x] * Tao[x]] + LambdaoPs) *
      Sqrt[(Pickoff[x] + LambdaoPs) * (Tao[x] + LambdaoPs)])^(1 / 2))^
    -1 == Tau, {x, FirstEstimate}, WorkingPrecision → 10];
```

Mean free path

```
L4 = 4 * R4 / 3;
```

Classical model

Mean free path

```
L5 = L5 /. FindRoot[(vthPA / L5 + LambdaoPs) ^ -1 == Tau, {L5, FirstEstimate}];
```
encontra raiz

Radius

Assuming the free volume is a sphere:

```
R5 = 3 * L5 / 4;
```

Combined Model

Mean free path

```
Piecefunction2[x_] :=
 Piecewise[{{( LambdaA * (1 - (3 * x / 4) / ((3 * x / 4) + Delta) + 1 / (2 Pi) *
```
função por partes
```
            Sin[2 Pi * (3 * x / 4) / ((3 * x / 4) + Delta)]) + LambdaoPs) ^ -1,
```
número pi
```
    (3 * x / 4) < Lvalue}, {(vthPA / (x - 2 Delta3) + LambdaoPs) ^ -1 , x ≥ Lvalue}}]

L6 = L6 /. FindRoot[Piecefunction2[L6] == Tau, {L6, FirstEstimate}];
```
encontra raiz

Radius

Assuming the free volume is a sphere

```
R6 = 3 * L6 / 4;
```

Results for the free volumes' size

```
If[Tau <= 3.4, data =
```
se
```
   {{"Model", " Radius(nm)", "Mean free path (nm)"}, {"Tao-Eldrup Model", R1 , L1},
```
média
```
    {"Tokyo Model", R2 , L2}, {"Combined Model", R6 , L6}} ];
If[Tau < 3.4, Print["In this lifetime range, only the Tao-Eldrup
```
escreve entrada
```
    Model, the Tokyo Model and the Combined Model are valid. The
    free volumes' sizes estimated according to these models are:",
```

```
  Grid[data, Alignment → Center, Spacings → {2, 1}, Frame → All,
              alinhamento   centro   espaçados              quadro  tudo
   Background → {None, {1 → RGBColor[0.643137, 0.282353, 1]}}]]]
                 nenhum     cores do sistema RGB

If[3.4 < Tau <= 16, data = {{"Model", " Radius(nm)", "Mean free path (nm)"},
se                                                    média
    {"Tao-Eldrup Model", R1 , L1}, {"Tokyo Model", R2 , L2},
    {"Hybrid Model", R4, L4}, {"Combined Model", R6, L6}} ];
If[3.4 < Tau <= 16, Print["In this lifetime range, only the Tao-Eldrup Model,
                     escreve  entrada
    the Tokyo Model, the Hybrid Model and the Combined Model are valid.
    The free volumes' sizes estimated according to these models are:",
  Grid[data, Alignment → Center, Spacings → {2, 1}, Frame → All,
              alinhamento   centro   espaçados              quadro  tudo
   Background → {None, {1 → RGBColor[0.643137, 0.282353, 1]}}]]]
                 nenhum     cores do sistema RGB
If[16 < Tau < 28, data = {{"Model", " Radius or Cube side(nm)", "Mean free path (nm)"},
                                                                  média
    {"Tao-Eldrup Model", R1 , L1}, {"Tokyo Model", R2 , L2},
    {"Rectangular Tao-Eldrup Model", R3, L3},
    {"Hybrid Model", R4, L4}, {"Combined Model", R6, L6}} ];
If[16 < Tau < 28, Print["In this lifetime range, only the Tao-Eldrup
                    escreve  entrada
    Model, the Tokyo Model, the Rectangular Tao-Edlrup Model,
    the Hybrid Model and the Combined Model are valid. The free
    volumes' sizes estimated according to these models are:",
  Grid[data, Alignment → Center, Spacings → {2, 1}, Frame → All,
              alinhamento   centro   espaçados              quadro  tudo
   Background → {None, {1 → RGBColor[0.643137, 0.282353, 1]}}]]]
                 nenhum     cores do sistema RGB
If[28 <= Tau < 123, data = {{"Model", " Radius or Cube side(nm)",
se
     "Mean free path (nm)"}, {"Tokyo Model", R2 , L2},
      média
    {"Rectangular Tao-Eldrup Model", R3, L3}, {"Hybrid Model", R4, L4},
    {"Combined Model", R6, L6}} ];
If[28 <= Tau < 123, Print["In this lifetime range, only the Tokyo Model, the
                     escreve  entrada
    Rectangular Tao-Edlrup Model, the Hybrid Model and the Combined Model are
    valid. The free volumes' sizes estimated according to these models are:",
  Grid[data, Alignment → Center, Spacings → {2, 1}, Frame → All,
              alinhamento   centro   espaçados              quadro  tudo
   Background → {None, {1 → RGBColor[0.643137, 0.282353, 1]}}]]]
                 nenhum     cores do sistema RGB
If[Tau == 123, data = {{"Model", " Radius or Cube side(nm)", "Mean free path (nm)"},
                                                                  média
    {"Rectangular Tao-Eldrup Model", R3, L3},
    {"Hybrid Model", R4, L4}, {"Combined Model", R6, L6}} ];
If[Tau == 123, Print["In this lifetime range, only the Rectangular Tao-Edlrup
                  escreve  entrada
    Model, the Hybrid Model and the Combined Model are valid. The
    free volumes' sizes estimated according to these models are:",
```

```
  Grid[data, Alignment → Center, Spacings → {2, 1}, Frame → All,
            |alinhamento  |centro  |espaçados          |quadro  |tudo
   Background → {None, {1 → RGBColor[0.643137, 0.282353, 1]}}]]]
                 |nenhum     |cores do sistema RGB
If[123 < Tau < 135, data = {{"Model", " Radius or Cube side(nm)",
|se
     "Mean free path (nm)"}, {"Rectangular Tao-Eldrup Model", R3, L3},
      |média
    {"Hybrid Model", R4, L4}, {"Classical Model", R5, L5},
    {"Combined Model", R6, L6}} ];
If[123 < Tau < 135, Print["In this lifetime range, only the Rectangular Tao-Edlrup
|se                  |escreve |entrada
    Model, the Hybrid Model, the Classical Model and the Combined Model are
    valid. The free volumes' sizes estimated according to these models are:",
  Grid[data, Alignment → Center, Spacings → {2, 1},
  |grade       |alinhamento  |centro  |espaçados
   Frame → All Background → {None, {1 → RGBColor[0.643137, 0.282353, 1]}}]]]
   |quadro  |t··· |imagem de fundo |nenhum     |cores do sistema RGB
If[135 <= Tau < 140, data = {{"Model", " Radius or Cube side(nm)",
|se
     "Mean free path (nm)"}, {"Hybrid Model", R4, L4},
      |média
    {"Classical Model", R5, L5}, {"Combined Model", R6, L6}} ];
If[135 <= Tau < 140, Print["In this lifetime range, only the Hybrid
|se                  |escreve |entrada
    Model, the Classical Model and the Combined Model are valid. The
    free volumes' sizes estimated according to these models are:",
  Grid[data, Alignment → Center, Spacings → {2, 1}, Frame → All,
  |grade       |alinhamento  |centro  |espaçados          |quadro  |tudo
   Background → {None, {1 → RGBColor[0.643137, 0.282353, 1]}}]]]
   |imagem de fundo |nenhum     |cores do sistema RGB
If[140 <= Tau < 142, data =
|se
   {{"Model", " Radius or Cube side(nm)", "Mean free path (nm)"},
                                           |média
    {"Classical Model", R5, L5}, {"Combined Model", R6, L6}} ];
If[140 <= Tau < 142, Print["In this lifetime range, only the
|se                  |escreve |entrada
    Classical Model and the Combined Model are valid. The free
    volumes' sizes estimated according to these models are:",
  Grid[data, Alignment → Center, Spacings → {2, 1}, Frame → All,
  |grade       |alinhamento  |centro  |espaçados          |quadro  |tudo
   Background → {None, {1 → RGBColor[0.643137, 0.282353, 1]}}]]]
   |imagem de fundo |nenhum     |cores do sistema RGB
If[Tau >= 142, data = {{"Model", " Radius or Cube side(nm)", "Mean free path (nm)"},
|se                                                          |média
    {"Classical Model", R5, L5}, {"Combined Model", R6, L6}} ];
If[Tau >= 142, Print["In this lifetime range, only the Classical Model is
|se               |escreve |entrada
    valid. The free volumes' size estimated according to this model is:",
  Grid[data, Alignment → Center, Spacings → {2, 1}, Frame → All,
  |grade       |alinhamento  |centro  |espaçados          |quadro  |tudo
   Background → {None, {1 → RGBColor[0.643137, 0.282353, 1]}}]]]
   |imagem de fundo |nenhum     |cores do sistema RGB
```

Figure C.5: Mathematica script for the free volumes' size estimation.